

Customized porosity in ceramic composites via freeze casting

Thesis by
Claire Taijung Kuo

In Partial Fulfillment of the Requirements for the
Degree of
DOCTOR OF PHILOSOPHY

The logo for the California Institute of Technology (Caltech), featuring the word "Caltech" in a bold, orange, sans-serif font.

CALIFORNIA INSTITUTE OF TECHNOLOGY
Pasadena, California

2021
Defended December 15, 2020

© 2021

Claire Taijung Kuo
ORCID: 0000-0002-3720-968X

All rights reserved

ACKNOWLEDGEMENTS

So many people have helped me along the way and without them, I could not reach where I am today. It has been a wonderful journey.

First, I would like to thank my advisor, Prof. Katherine Faber, who has been the best mentor anyone could ask for. I have grown so much as a researcher under her guidance. I especially appreciate her vision that as a researcher, we are here to do good and sound science. There are rough bumps along the way when experiments were just not working but her encouragement and support have always made me want to try again.

Next, I would like to thank Prof. Brent Fultz, Prof. William Johnson, and Prof. Julie Kornfield for graciously agreeing to be on my thesis committee, encouraging me when I first started, reviewing my thesis, and giving invaluable advice.

Many thanks also go out to my research group mates in the Faber group: Dr. Matthew Johnson, Dr. Sarah Miller, Dr. Maninpat Naviroj, Dr. Xiaomei Zeng, Dr. Wei-Lin Tan, Dr. Neal Brodnik, Dr. Noriaki Arai, Ben Herren, Celia Chari, Vince Wu, Laura Quinn, and Carl Keck. I would like to thank Putt, Matt, and Wei-Lin for their mentorships and for helping me navigate research and life. I value Nori's 5+ years of friendship, helpful suggestions, and support. My gratitude also goes to Carl for his work on SiC whiskers. I would also like to thank Xiaomei, Neal, Ben, Celia, Vince, Laura, and Carl for all their research suggestions, support, and sense of humor that got me through the PhD program. It wouldn't be the same without you.

Special thanks to my collaborators, Lisa M. Rueschhoff, Matthew B. Dickerson, and Tulsi A. Patel at Air Force Research Laboratory for providing expertise in the block copolymer, analyzing the gel structures, conducting XCT, bouncing ideas off of, and revising the manuscript. I would also like to thank the administrative staff at Caltech, Angie, Katie, Jennifer, and Christy, who have always been one email away and ready to save the day.

I'm infinitely grateful for the support of all my friends at Caltech and in Taiwan, the Yangi crew, the Craft & Tea group, Hannah and Oscar, Pai, and many more. Finally, I would like to thank my family for their unwavering support throughout the years. Their belief in me motivates me to keep trying and reach higher every day.

ABSTRACT

Freeze casting is a facile pore-forming technique for ceramics as it affords great tunability in pore structure including size, morphology, wall thickness, tortuosity, and alignment. Nevertheless, similar to any other pore-forming techniques, it has limitations in terms of the range of accessible properties. For example, a porous lamellar structure is highly permeable but easily fractures, while the dendritic structure is the opposite. This research seeks to provide strategies used with freeze casting to achieve a combination of properties that go beyond the current limitations and create optimized pore structures with a specific focus on three properties: strength, permeability, and surface area.

Such strategies utilize two composite material principles. First, particle reinforcement was implemented to optimize the mechanical and transport properties. Second, surface area was increased with hierarchical design for enhanced capture or catalysis applications. To optimize the mechanical and transport properties, we reinforced high-permeability lamellar structures with reinforcement fillers of silicon carbide (SiC) whiskers and carbon nanotubes (CNTs). The two fillers afford two different mechanisms of reinforcement: structural and material reinforcement.

Additions of 30 vol.% SiC whiskers increased the compressive strength by 325% at a small expense in permeability. Shear failure, common in lamellar structures, was prevented by the interwall bridges produced via particle engulfment during freezing. These bridges were demonstrated by the change in microstructure, stress-strain behavior, and fracture surfaces. A 2D *in-situ* solidification experiment was conducted to observe solidification and particle engulfment directly. We proposed a modified engulfment model to account for the complexity stemming from high-aspect ratio particles and non-planar freezing fronts. Reasonable agreement was found between the model, the simulation based on the model, and the experimental values from the freeze-casting and 2D-solidification experiments.

Freeze-casting with CNTs was explored as an alternative reinforcement strategy, but one which maintains the original pore structure. CNTs were pushed aside by the freezing front to pore walls due to their small diameters for low CNT concentration composites (<4.5 wt.%) such that the original pore structures remained. The compressive strength increased, albeit by smaller percentages (118% for 4.3 wt.%) than those with SiC whiskers. The increase was attributed to the toughening of pore

walls with no diminishing effect on permeability. In addition, CNTs changed the electrical conductivity by ten orders of magnitude with the addition of 8.2 wt.% of the reinforcement.

Finally, conformal coatings via self-assembly of block copolymers (BCP) were produced by infiltration into a freeze-cast lamellar structure and significantly increased the surface area of the underlying scaffold. A bimodal pore size distribution with nanometer-size pores from the BCP self-assembly and micron-size pores from freeze casting was observed. An increase in compressive strengths was achieved with the introduction of pore hierarchy while retaining permeability of the macroporous structure due to enlarged lamellar spacings from the infiltration process.

PUBLISHED CONTENT AND CONTRIBUTIONS

- [1] C. T. Kuo and K. T. Faber. Permeable carbon nanotube-reinforced silicon oxycarbide via freeze casting with enhanced mechanical stability. *Journal of the European Ceramic Society*, 40(6):2470–2479, 2020. doi: 10.1016/j.jeurceramsoc.2019.12.059. URL <https://doi.org/10.1016/j.jeurceramsoc.2019.12.059>.
T. Kuo fabricated and characterized CNT composites, and wrote the manuscript.
- [2] Taijung Kuo, Carl H. Keck, and Katherine T. Faber. Porous SiC-SiOC composites through particle engulfment of high-aspect ratio particles during freeze casting. *Manuscript in preparation*, 2021.
T. Kuo fabricated and characterized SiC composites using SEM and MIP, their permeabilities, and compressive strengths, developed the model and simulated solidification process for freeze casting high-aspect ratio particle, and wrote the manuscript.
- [3] Taijung Kuo, Lisa M. Rueschhoff, Matthew B. Dickerson, Tulsi A. Patel, and Katherine T. Faber. Hierarchical porous SiOC via freeze casting and self-assembly of block copolymers. *Scripta Materialia*, 191:204–209, 2021. doi: 10.1016/j.scriptamat.2020.09.042. URL <https://linkinghub.elsevier.com/retrieve/pii/S1359646220306412>.
T. Kuo fabricated and characterized hierarchical ceramics using SEM, MIP, and N₂ adsorption isotherms, characterized weight loss, volume shrinkage, compressive strengths, and permeabilities, conducted image analysis on X-ray computed tomography (XCT) datasets, and wrote the majority of the manuscript.

TABLE OF CONTENTS

Acknowledgements	iii
Abstract	iv
Published Content and Contributions	vi
Table of Contents	vi
List of Illustrations	ix
List of Tables	xv
Chapter I: Introduction	1
1.1 Motivation and Objectives	1
1.2 Thesis Organization	3
Chapter II: Background	4
2.1 Freeze Casting	4
2.1.1 Solid Contents	6
2.1.2 Solvents and Additives	7
2.1.3 Solidification and Post-freezing Treatments	11
2.1.4 Particle Engulfment	15
2.1.5 Sintering/pyrolysis and Post-freeze Casting Treatments	16
2.2 Self-assembled Block Copolymers	17
2.3 Preceramic Polymers	20
2.3.1 Overview of Polymer-derived Ceramics (PDCs)	20
2.3.2 Polysilsesquioxane	22
2.3.3 Polycarbosilane	23
Chapter III: SiC Whisker-reinforced Composites	25
3.1 Introduction	25
3.2 Experimental Procedures	26
3.2.1 Freeze Casting	26
3.2.1.1 Materials and Synthesis	26
3.2.1.2 Characterization	28
3.2.2 Two-dimensional Solidification Experiments and Simulations	29
3.2.2.1 Experimental Setup	29
3.2.2.2 Viscosity	30
3.2.2.3 Surface Energy	30
3.2.2.4 Freezing Simulations	31
3.3 Results and Discussion	32
3.3.1 Freeze-cast Samples	32
3.3.1.1 Pore Structures	32
3.3.1.2 Mechanical Properties and Permeability	37
3.3.2 Two-dimensional <i>in-situ</i> Solidification Experiments	39
3.3.2.1 Theory	39

3.3.2.2	Engulfment-related Forces and Critical Freezing Front Velocity	40
3.3.2.3	Torque and Whisker Rotation	45
3.3.2.4	Freezing Simulations and Bridge density	47
3.4	Conclusions	50
Chapter IV:	Carbon Nanotube-reinforced Composites	51
4.1	Introduction	51
4.2	Experimental Methods	52
4.2.1	Materials and Processing	52
4.2.2	X-ray Diffraction	54
4.2.3	Electrical Conductivity	54
4.2.4	Permeability	54
4.2.5	Mechanical Properties	56
4.2.5.1	Compressive Strength	56
4.2.5.2	Fracture Toughness	56
4.3	Results and Discussion	57
4.3.1	Carbon Nanotube Dispersion in Solution and Freeze-cast Structures	57
4.3.2	Electrical Conductivity	61
4.3.3	Permeability	63
4.3.4	Mechanical Properties	64
4.4	Conclusions and Implications	71
Chapter V:	Hierarchical Composites via Self-assembly of Block Copolymer	73
5.1	Introduction	73
5.2	Experimental Methods	74
5.2.1	Materials and Processing	74
5.2.2	Pore Structure	76
5.2.3	Permeability	76
5.2.4	Mechanical Properties	76
5.3	Results and Discussion	78
5.4	Conclusions and Implications	87
Chapter VI:	Summary, Conclusions, and Future Work	89
6.1	Summary and Conclusions	89
6.2	Suggestions for Future Work	95
References	97
Appendix A:	Stress-Strain Curves of SiC Whisker Composites and Pure SiOC	120
Appendix B:	Surface Energy Difference as the Origin of the Repulsive Force	121
Appendix C:	Calculation of Torques	123
C.1	Torque from Fluid Motion	123
C.2	Torque from Frictional Force	124
Appendix D:	Examples of Rotation From the Freezing Video	125
Appendix E:	Lamellar Spacing and Freezing Front Velocity	126

LIST OF ILLUSTRATIONS

<i>Number</i>	<i>Page</i>
2.1 Schematic of the freeze casting process showing solution/suspension preparation, solidification, sublimation, and sintering/pyrolysis steps [125].	5
2.2 Critical freezing front velocity, above which particles are engulfed and below which particles are pushed by the freezing front, as a function of particle size and the respective resultant pore structures formed from particles pushed or engulfed by the freezing front. Adapted from [30] with permission from Elsevier.	7
2.3 (a) Non-faceted [113] (Copyright (1998) National Academy of Sciences, USA) and (b) faceted [81] (Reprinted with permission from Elsevier) cellular arrays.	8
2.4 (a) Schematic of a faceted solid-liquid interface showing A. a kink-site, B. an atom/molecule adding to the kink-site, C. an interfacial vacancy, D. an ad-atom, E. exposed underlying lattice plane, and F. an island of ad-atoms (b) System energy as a function of ad-atom coverage, ξ . The change in the relative position of the energy minima demonstrate a transition from an atomically rough interface ($\alpha < 2$) to an atomically smooth interface ($\alpha > 2$) [67]. Reprinted by permission from Springer Nature.	9
2.5 Optical images of the crystal structures formed from different solvents and the SEM images of their respective freeze-cast pore structure. Adapted from [125].	10
2.6 Microstructure selection map of crystal morphology and size depending on temperature gradient and growth rate [93] © 2003 John Wiley & Sons, Inc..	12
2.7 Microstructural transition from planar to cellular to dendritic freezing front (from top to bottom) in a succinonitrile and coumarin 152 binary alloy [113]. Copyright (1998) National Academy of Sciences, USA.	13
2.8 Solvent nucleation control via a wettability gradient enables a long-range pore alignment from [201]. Reprinted with permission from AAAS.	14

2.9	SEM images showing (a) the effects on alignment of a magnetic field on TiO ₂ scaffolds containing 3 wt% Fe ₃ O ₄ (reprinted from [137] with permission from Elsevier) (b) the effects on alignment of an electric field on aqueous slurries (reprinted from [173] with permission from Elsevier), and (c) the effects of acoustic waves on mechanical properties and pore structure [129].	15
2.10	Schematic of the structure and the mechanical property of PMMA-PnBA-PMMA triblock copolymer gel as a function of temperature. Reproduced from [51].	18
2.11	(A) Chemical structures of PMMA-PnBA-PMMA, polycarbosilane, and PMMA. (B) Schematic of resultant morphologies of the gel system and (C) the corresponding atomic force microscopy (AFM) images. Scale bars are 100 nm [21].	19
2.12	Typical classes of silicon-based preceramic polymers as precursors of polymer derived-ceramics [36] © 2010 The American Ceramic Society.	21
2.13	Schematic of the processing and chemical structures of preceramic polymers to polymer-derived ceramics [68, 125].	22
2.14	Two proposed models of the microstructure of polysiloxane-derived SiOC. Reprinted from [183] with permission from Elsevier.	23
3.1	An SEM image of as-received faceted SiC whiskers.	27
3.2	A schematic of (a) freeze casting setup and (b) 2D solidification setup.	30
3.3	A schematic of input variables used in freezing simulation.	32
3.4	SEM images of freeze-cast lamellar structures with (a) 0, (b) 10, (c) 20, (d) 30 vol.% SiC whiskers and (e) 20 vol.% SiC whiskers freeze-cast lamellar structures with SiC-SiOC bridges (blue circles) and SiC whiskers (yellow circles) bridges (f) Example images of bridge density measurements. Green lines mark the counted whisker bridges. (g) Bridge density as a function of the whisker concentration. Error bars represent ± 1 standard deviation.	33
3.5	Pore size distributions from MIP and the corresponding SEM images of freeze-cast pore structures of (a) SiOC using DMC and cyclohexane, adapted from [126], and (b) SiOC and 30 vol.% SiC whisker composites using DMC in this work.	35

3.6	Compressive strength as a function of (a) permeability and (b) relative density. Error bars represent ± 1 standard deviation. (c) Representative stress-strain curves for freeze-cast pure SiOC (dotted black line) and for a freeze-cast 30 vol.% SiC composite (blue line). The insets show SEM images of fracture surfaces of pure SiOC ceramics and 30 vol.% SiC composites with arrows pointing toward the corresponding the stress-strain curves.	37
3.7	(a) A schematic of the acting forces during the engulfment process. (b) An example of a dendrite tip angle measurement. (c) Dendrite tip angle as a function of freezing front velocity. Error bars represent ± 1 standard deviation.	40
3.8	A schematic of solute pileup during the freezing process and the resulting osmotic pressure difference.	43
3.9	Freezing front velocity versus whisker length with experimental data; blue circles represent pushed whiskers; orange circles represent engulfed whiskers. The theoretical critical freezing front velocity (grey line) was calculated with engulfment model described in Section 3.3.2.2.	45
3.10	The torque acting on whiskers as a function of (a) offset distance, and (b) intersecting angle.	46
3.11	(a) Visualization of simulation (SiC concentration = 2 vol.%, $d = 2 \mu\text{m}$, $L = 30 \mu\text{m}$, $V_{ff} = 45 \mu\text{m/s}$). Blue lines represent freezing dendrites. Whiskers are randomly distributed and orientated. (b) Probability of engulfment fraction from the simulation for 10, 20, and 30 vol. % SiC solidification.	48
3.12	Averaged simulated engulfed whisker fraction as a function of (a) Freezing front velocity and (b) whisker length.	49
4.1	(a) Schematic of the experimental setup for permeability measurement [125]. (b) Schematic of the experimental setup for diametral compression (Brazilian disk) test. Disks were placed between compression platens with an aligner before the start of the compression testing to ensure the load was applied along the long axis of pre-crack.	55
4.2	Suspensions with 3 mg/ml CNTs and 300 mg/ml MK (a) without, and (b) with KD1. Representative SEM micrographs of the resulting freeze-cast structures with 1.3 wt.% CNTs (c) without and, (d) with KD1.	58

4.3	Representative SEM micrographs of freeze-cast structures (a) pure SiOC, (b) 1.3, (c) 4.3, (d) 8.2 wt.% CNT composites.	59
4.4	Representative SEM micrographs of freeze-cast walls of (a) pure SiOC, (b) 1.3 (c) 4.3, (d) 8.2 wt.% CNT composites. The white dots, present in 1.3, 4.3, 8.2 wt.% samples, are carbon nanotubes. Sub-micron agglomerates are highlighted with green circles.	60
4.5	(a) XRD pattern of pure SiOC, 4.3, 8.2 wt.% CNT composites and MWCNTs. (b) Background subtraction and peak fitting performed on XRD pattern of 8.2 wt.% CNT composite to identify phases present. 61	61
4.6	Electrical conductivity, calculated without adjustment for porosity, as a function of CNT concentration of freeze-cast composites. The resistance of one pure SiOC sample was above the equipment limit (200 G Ω) of Keithley 614 Electrometer and its conductivity was calculated using the limit. This data point was plotted with a circle and a downward arrow.	62
4.7	(a) Pressure vs. flow velocity to establish permeability of pure SiOC and CNT-SiOC composites. (b) Permeability (circles with lefthand axis) and porosity (triangles with righthand axis) as a function of CNT concentration of freeze-cast composites. Error bars represent \pm one standard deviation.	64
4.8	(a) Representative stress-strain curves of freeze-cast samples. The first load drop around 1 MPa in most samples is suspected to be from the realignment of the washer. Examples of fractured samples after compression with (b) pure SiOC and (c) 8.2 wt.% CNTs. The blue disk-like capping is a cured mineral-filled acrylic applied to avoid crushing behavior common in compression tests of porous ceramics.	65
4.9	SEM micrographs of freeze-cast and pyrolyzed walls of (a) pure SiOC and (b) 8.2 wt.% CNTs. In pure SiOC, the lamellae are smooth with few features and bridges. In the 8.2 wt.% composite, the lamellae are bridged with CNT agglomerates. SEM micrographs of fracture surfaces with (c) pure SiOC and (d) 8.2 wt.% CNTs. The green arrows in (d) point to the agglomerate bridges between lamellae.	67

4.10	(a) Compressive strength and fracture toughness as a function of CNT concentration. (b) Compressive strength vs. permeability constant of freeze-cast CNT-SiOC composites compared with that of pure SiOC both in this work and the values reported by Naviroj [125]. Error bars represent \pm one standard deviation.	68
4.11	Representative SEM micrographs of fracture surfaces of Brazilian disks of (a) pure SiOC and (b) 4.3 wt.% CNTs. The insets in (b) shows a magnified image of a fracture surface of 4.3 wt.% CNT composites. The rough patches, appearing in 4.3 wt.% composites, are clusters of CNT agglomerates.	69
5.1	(a) AFM phase view of as-deposited films (left) and SEM image of pyrolyzed films (right) made with BCP/PCP gel. (b) Schematic of the synthesis process for Hierarchical20. SEM images of pyrolyzed freeze-cast structures of (c) Freezecast20 and (d) Hierarchical20, with (e) enlarged lamellar spacings and (f) porous conformal coating on the freeze-cast pore wall of Hierarchical20.	78
5.2	Pore size distribution of Hierarchical20 and Freezecast20 pore structure from MIP. Smoothing of the data, indicated by solid lines, was performed by averaging sets of five consecutive points minus outliers.	80
5.3	Stages of the lamellar spacing analysis from X-ray CT (A tomogram of Hierarchical20 is used as an example) (a) Original 2D image and segmented image (b) Euclidean distance map (c) 2D skeleton of lamellar pores (d) Graphic representation of lamellar spacing measurements (e) Average lamellar spacings from image analysis of 2D X-ray tomograms.	82
5.4	(a) Permeability as a function of open porosity and (b) compressive strength and Young's modulus as a function of relative density of all Freezecast and Hierarchical20 samples. Error bars represent ± 1 standard deviation. Dotted lines and the dashed line are linear regressions on log-log plots of baseline materials, included to guide the reader.	84
5.5	Strain at maximum stress as a function of relative density of all Freezecast and Hierarchical20 samples. Error bars represent ± 1 standard deviation. Dotted lines is a linear regressions of baseline materials, included to guide the reader.	84

5.6	Representative stress–strain curves of (a) Freezecast20 and Hierarchical20 and (b) Freezecast15, Freezecast25, and Freezecast35. SEM micrographs of fracture surfaces of (c) Freezecast15 and (d) Freezecast35. Examples of fractured samples after compression of (e) Freezecast15 and (f) Freezecast35.	86
6.1	Compressive strength as a function of relative density of freeze-cast pure SiOC from the CNT-reinforced, the SiC-reinforced, and the BCP-hierarchical porous solid projects.	91
6.2	Compressive strength vs. permeability constant of CNT-reinforced, SiC whisker-reinforced, and hierarchical composites, and corresponding fracture surfaces and macro-images of fractured samples. The inset includes the stress-strain curves of freeze-cast pure SiOC of various densities from BCP-hierarchical project for reference.	92
6.3	Compressive strength vs. permeability constant of CNT-reinforced, SiC whisker-reinforced, and hierarchical composites compared with that of pure SiOC reported by Naviroj [125].	94
A.1	Stress-strain curves of freeze-cast pure SiOC ceramics (black lines) and 30 vol.% SiC composites (blue lines)	120
B.1	A schematic of (a) the surface energy difference, and (b) the surface area of the dendrite in contact with the whisker during the engulfment process.	122
D.1	Predicted rotations based on the model and examples of the rotation in the solidification video. Each image sequence is arranged chronologically with (a) original images and (b) images with green lines marking the whisker configuration.	125
E.1	(a) Freezing front velocity and (b) lamellar spacing as functions of sample height. (c) Lamellar spacing as a function of freezing front velocity	127

LIST OF TABLES

<i>Number</i>	<i>Page</i>
2.1 Melting point, heat of fusion, entropic term of Jackson alpha-factor, and pore morphology of common solvents. Adapted from [125]. . . .	9
3.1 Composition of suspension and porosity of the pyrolyzed porous composites.	28
3.2 Values of input variables for simulation.	31
3.3 Comparison of the engulfed whisker ratio between the freeze-cast samples and freezing simulation	49
4.1 Compositions of suspensions and pyrolyzed samples.	54
5.1 Chemical composition (in weight percent) of MK- and SMP-10-derived ceramics. The elemental analyses were conducted with a thermobarometrical redox analysis [154, 185] and by a carbon analyzer [86].	75
5.2 Average porosity after pyrolysis of all Freezecast and Hierarchical20 samples. Six samples were tested for each polymer concentration. . .	75
5.3 Volume and weight changes (in percent) after each processing step of Freezecast20 and Hierarchical20. At least five samples are measured for each step.	80

Chapter 1

INTRODUCTION

1.1 Motivation and Objectives

Pores in ceramic materials have an immense influence on their mechanical properties due to their brittle nature compared to their counterparts in polymers and metals. Nevertheless, ceramics have unique chemical resistance, high-temperature stability, and high strength otherwise unachievable by other materials, making porous ceramics attractive candidates for filters, electrodes, bio-scaffolds, and catalyst supports [42, 46, 58, 71]. Each of these applications has different property requirements, such as its mechanical strength, surface area, or fluid permeability. These properties are determined by pore characteristics—pore size, morphology, and connectivity, etc. Therefore, it is crucial to have the capability of tuning the pore structure to optimize the performance of a final product for a given application.

For transport or filter applications, good mechanical properties ensure product robustness against the fluid backpressure during the operation; high permeability increases product throughput; high surface area creates more reaction or capture sites. However, to increase surface area, structures with micropores (<2 nm) or mesopores (2-50 nm) are preferable but these create high fluid backpressure that demands higher filter strength and more energy to operate compared to the structures with macropores (>50 nm). Furthermore, macroporous materials often have better mechanical and chemical stability [37, 76, 114].

The aforementioned challenges can be mitigated with pores at multiple length-scales by constructing a hierarchical porous structure. For example, a high surface-area mesoporous coating for catalytic functions and an underlying macroporous frame that provides the required mechanical strength and transport property can be coupled. In this case, an optimal combination of mechanical strength and transport property requires the capability of tuning the underlying macroporous scaffold.

Common methods to create macropores (>50 nm) in ceramics include additive manufacturing, direct foaming, the replica technique, and sacrificial templating [54, 169]. Additive manufacturing is capable of creating complex structures precisely, but the process currently lacks industrial scalability. Direct foaming is inexpensive, fast, and easy, but only isotropic, spherical pore structures are achievable. The

replica technique is simple and well-established, but the mechanical properties are usually poor due to the hollow struts in the structures. Sacrificial templating methods provide a variety of pore morphologies and sizes, but extra care is needed during the removal of template to avoid cracking.

Among sacrificial template methods, freeze casting is particularly attractive as it offers tailorability in pore size, morphology, wall thickness, tortuosity, and pore alignment by controlling solidification [32, 47, 48, 61, 146]. Furthermore, freeze casting is readily scalable for the production of porous ceramics with complex structures [36].

Freeze casting utilizes the phase separation between a solvent and dispersed solid or solute during solidification to template the pore structure. The solvent crystallizes in different sizes, shapes, and alignment based on the nature of the solvent and the conditions of solidification. The solvent crystals are subsequently removed by sublimation, leaving behind a pore network. The chemistry and the physical properties of the solids, the dispersing or dissolving component, affect both the solidification process and the surface chemistry of the final product. Polymers, metals, and ceramics have all been used as solids in freeze casting. Moreover, more than one type of solid can be incorporated to fabricate composites. The versatility and tunability make freeze casting an attractive technique for tuning the pore structure to meet the requirements of each application.

In particular, freeze casting with preceramic polymers to fabricate porous ceramic has garnered increasing interest as it offers many processing advantages over that with ceramic powders, including reduced temperatures needed for densify the ceramic walls, better control over freezing front velocity, and greater alignment of the pore structure [4, 124–127, 193].

While freeze casting is useful for tuning the pore structure, optimizing the structure for adequate mechanical and transport properties remains a challenge, as they are often inversely related to each other through porosity. Highly porous structures have low strength and vice versa [4, 125].

Therefore, the goal of this research is to provide strategies for creating optimized pore structures that provide sufficient strength, permeability, and surface area under the framework of freeze-casting. Such strategies are based upon composite material principles of both particle reinforcement and hierarchical design. First, to optimize the mechanical and transport properties, we reinforced a high-permeability pore

structure by reinforcement fillers of silicon carbide (SiC) whiskers and carbon nanotubes (CNTs). The two fillers afford two different mechanisms of reinforcement of pore structures: structural reinforcement across pore walls and material reinforcement within the pore walls. In the former, we explore the phenomenon of whisker engulfment by the freezing solvent to produce interwall bridges. Second, to increase the pore surface area, a high-surface-area conformal coating was created on a pore scaffold. This scaffold can be tuned by the methods outlined in the first part of the thesis to achieve the desired mechanical and transport properties, and its surface area can be increased by the high-surface-area coating. With these strategies, a pore structure can be tuned to meet the requirements for specific applications.

1.2 Thesis Organization

This document is organized as follows: Chapter 2 provides the necessary background on freeze casting, self-assembly block co-polymers, and preceramic polymers. Chapter 3 introduces the structural route of reinforcement with silicon carbide whisker fillers, a modified particle engulfment model for freeze casting high-aspect ratio particles, and a simulation based on the proposed engulfment model. The properties of resultant pore structures, including permeability and compressive strength, are examined. The experimental results are compared with the theoretical results based on the proposed model. Chapter 4 investigates the material route of reinforcement with carbon nanotubes as reinforcement fillers. Requirements of reinforcement fillers for the material route are discussed. The processing and dispersion methods are described, as well as the effect of CNTs on the microstructure, electrical conductivity, permeability, compressive strength, and toughness. Chapter 5 discusses the design and processing of a hierarchical structure via self-assembly of the block copolymer. The processing, and resultant microstructures, compressive strength, permeability and surface area of the hierarchical pore structures are featured. Chapter 6 summarizes the results, compares the mechanical and transport properties of the three porous composites in this work, and concludes with suggestions for future study.

Chapter 2

BACKGROUND

2.1 Freeze Casting

Freeze casting utilizes phase separation and particle rejection during solidification to create pore structures. The process of freeze casting contains four steps, as shown in Fig. 2.1.

In the first step of the process, powders/polymers are dispersed/dissolved in a dispersing medium/solvent (1a and 1b). The solution or suspension is then cast into a mold and frozen under a thermal gradient. Phase separation between the dispersing medium/solvent and the dispersed/dissolved phase occurs. The solvent crystals grow along the direction of the thermal gradient, rejecting the dispersed/dissolved phase to form what will ultimately become pore walls (2). The frozen suspension/solution is sublimed under vacuum, leaving behind a porous body, which is a negative of the solvent crystals (3). Finally, the porous body requires sintering or pyrolyzation to densify or convert the polymer into ceramics if necessary (4a and 4b).

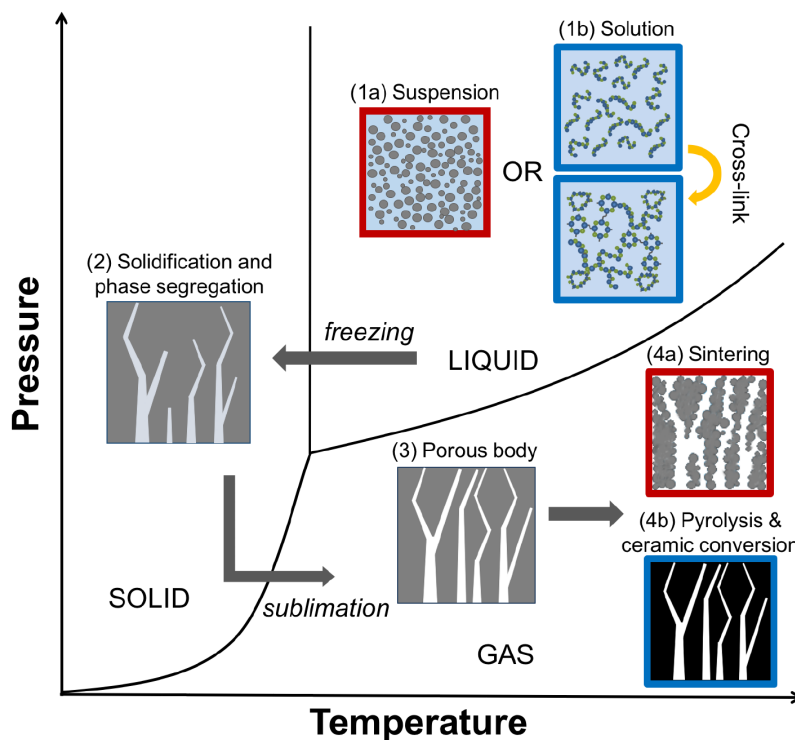


Figure 2.1: Schematic of the freeze casting process showing solution/suspension preparation, solidification, sublimation, and sintering/pyrolysis steps [125].

Although the process of freeze casting requires only four steps, there are plentiful opportunities for tuning the resultant pore structure and its properties [46, 48, 71, 118, 125, 133, 178]. For example, solid contents and solvent/dispersing medium are readily adjustable in the solution/suspension preparation step. Freezing front velocity and thermal gradient during solidification strongly influence the resultant pore structures. In addition to those two processing parameters, external forces and nucleation-controlled tools may be used during the process of freezing. Post-freezing treatments such as coarsening change the pore morphology and pore size. In the sintering/pyrolysis step, firing temperature and atmosphere alter the porosity and chemistry of the pore structure and can facilitate the growth of nanowires via carbothermal reduction. Post-freeze casting processes can also be applied to introduce a functionalized surface, or to increase the surface area. These processing parameters are discussed in detail in the following sections.

2.1.1 Solid Contents

For ceramic processing, both ceramic powders and preceramic polymers are suitable ceramic precursors. Freeze casting with powders allows a wider variety of starting materials for use in bone scaffolds [102], sensors [190], or fuel cells [110]. Magnetic powders are used along with an external magnetic field for a better pore alignment [137].

Freeze casting with preceramic polymers produces pore structures with smoother pore walls, due to the amorphous character of the pyrolyzed ceramic, and a higher anisotropy. Preceramic polymers also have more processing advantages compared to powders, including a lower sintering/pyrolysis temperature and transparency upon dissolution, and therefore enable a precise control of the freezing front velocity as a result of good contrast between the frozen solvent and liquid solution [126].

It should also be noted that metal or polymer starting materials, though less popular than ceramics, are also employed in freeze casting [103, 191]. Freeze-casting with metal powders often produces structures with high oxygen content (sometimes intentionally), which are later reduced with an additional reduction step [137].

Increasing solids loading decreases the porosity, decreases the pore size, and increases the width of pore walls. These three effects all contribute to better mechanical properties [156]. However, the decrease in porosity has an adverse effect on transport properties [160]. Higher solids loading decreases pore connectivity [125] and also results in high viscosity, posing a challenge to obtain stable dispersions or suspensions for the processing [29, 105].

Smaller particles replicate the features of solvent crystals in higher resolution [46]. In addition, freeze casting with small particles generally creates stronger pore structures as the small interparticle pores are more likely to close during sintering [204]. Large particles are also more likely to be engulfed by the freezing front, not pushed away to form pore walls. Upon engulfment, the phase separation phenomenon that freeze casting relies upon ceases to happen, resulting in isotropic pore structures shown in Fig. 2.2. However, small particles are difficult to disperse and raise the viscosity of suspension rapidly as they have a high surface area to volume ratio, which can be detrimental to the processing [105].

Faceted particles or high-aspect ratio particles are used in freeze casting for their ability to enhance mechanical, thermal or electrical properties. Carbon nanotubes (CNTs) are used to create conductive and bio-compatible pore structures, ideal for

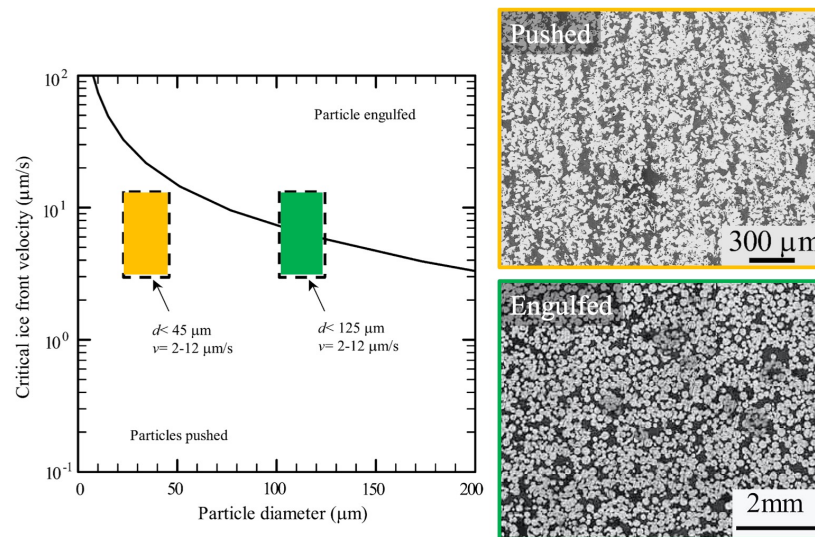


Figure 2.2: Critical freezing front velocity, above which particles are engulfed and below which particles are pushed by the freezing front, as a function of particle size and the respective resultant pore structures formed from particles pushed or engulfed by the freezing front. Adapted from [30] with permission from Elsevier.

a microbial fuel cell [73]. Alumina platelets introduce reinforcing inter-pore bridges [63]. Silicon carbide (SiC) whisker freeze-cast structures are strong, lightweight, and semi-conductive, and have good thermal conductivity [57].

2.1.2 Solvents and Additives

Since the pore structure is a negative of the solvent crystals, pore morphology is controlled by the solvent crystal structure. The shape of the freezing front, i.e. non-faceted (Fig. 2.3(a)) versus faceted (Fig. 2.3(b)), is largely determined by whether the freezing interface is able to accommodate a larger number of ad-atoms. If only specific sites such as kink sites at a step edge on the interface are energetically favorable, the interface grows laterally, advancing one layer at a time, as shown in Fig. 2.4. This type of growth mechanism results in an atomically smooth interface and a faceted crystal that has a preferred growth orientation [67].

An important parameter to predict whether a melt solidifies with faceted or non-faceted interface is the Jackson alpha-factor, α . Jackson and Hunt [80] developed a simple two-layer Bragg–Williams interface model, depicting a solid-liquid interface that is composed of two layers. The equilibrium configuration of ad-atoms and

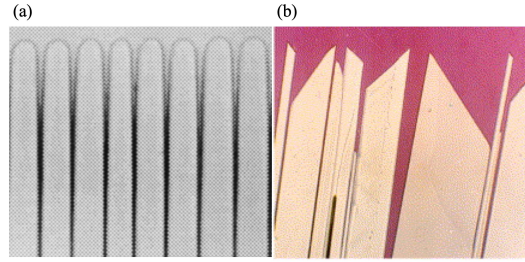


Figure 2.3: (a) Non-faceted [113] (Copyright (1998) National Academy of Sciences, USA) and (b) faceted [81] (Reprinted with permission from Elsevier) cellular arrays.

interfacial vacant sites is determined by the energy of the system, a function of the ad-atom coverage, ξ and the Jackson alpha-factor, α .

Melt systems with $\alpha \leq 2$ have an energy minimum at $\xi = 0.5$, indicating equal densities of ad-atoms and interfacial vacant sites. The interface is then atomically rough. Energy minima occur near $\xi = 0$ and $\xi = 1$ for materials with $\alpha > 2$. The configuration with $\xi \sim 0$ describes an interface with sparse ad-atoms and $\xi \sim 1$ implies an interface almost completely covered with only a few vacant sites. Both situations depict an atomically smooth surface.

The Jackson alpha-factor is composed of two terms, the entropic terms from thermodynamic and the geometric term from crystallography [5].

$$\alpha \equiv \frac{L}{k_B T_m} \times \frac{\eta}{Z} \quad (2.1)$$

where η is the number of in-plane nearest neighbor sites of an atom on the interface, Z is the total number of nearest neighbors of an atom in the crystal, L is the latent heat, k_B is the Boltzmann constant, and T_m is the melting temperature. The geometric term depends on the crystal structure (or the coordination number) and the orientation of the interface, ranging from 0.25 to 1. The entropic term is calculated from the melting point and the latent heat of the solvent.

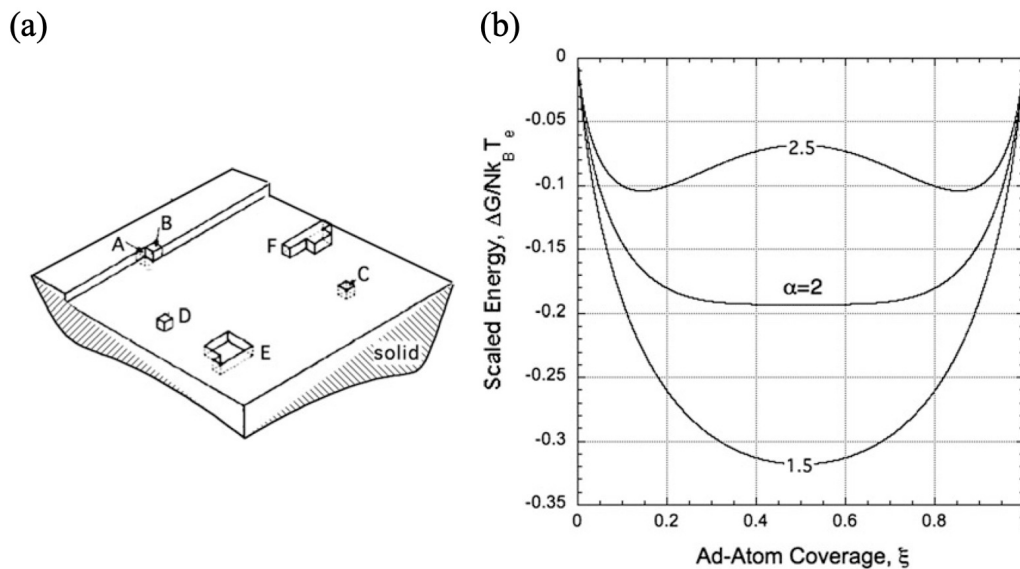


Figure 2.4: (a) Schematic of a faceted solid-liquid interface showing A. a kink-site, B. an atom/molecule adding to the kink-site, C. an interfacial vacancy, D. an ad-atom, E. exposed underlying lattice plane, and F. an island of ad-atoms (b) System energy as a function of ad-atom coverage, ξ . The change in the relative position of the energy minima demonstrate a transition from an atomically rough interface ($\alpha < 2$) to an atomically smooth interface ($\alpha > 2$) [67]. Reprinted by permission from Springer Nature.

Table 2.1: Melting point, heat of fusion, entropic term of Jackson alpha-factor, and pore morphology of common solvents. Adapted from [125].

Solvent	Melting point (°C)	Heat of fusion (kJ/mol)	Entropic term, $L/k_B T_m$	Pore morphology
Cyclooctane	14.6	2.41	1.01	Isotropic
Cyclohexane	6.5	2.68	1.15	Dendritic
t-Butanol	25.3	6.70	2.70	Prismatic
Dimethyl carbonate	3.5	13.22	5.75	Lamellar

Naviroj [125] revealed a striking correlation between Jackson alpha-factor, solvent crystal structures, and the resultant freeze-cast pore structures. Table 2.1 shows that cyclooctane has the lowest entropic term among the chosen solvents, followed by cyclohexane, t-butanol, and dimethyl carbonate. Fig. 2.5 shows optical images of the crystal structures and SEM images of the freeze-cast pore structure from these solvents. Solvents with a particularly low entropic term such as cyclooctane produce seaweed-like crystal structures. The anisotropy of the seaweed-like structure is even

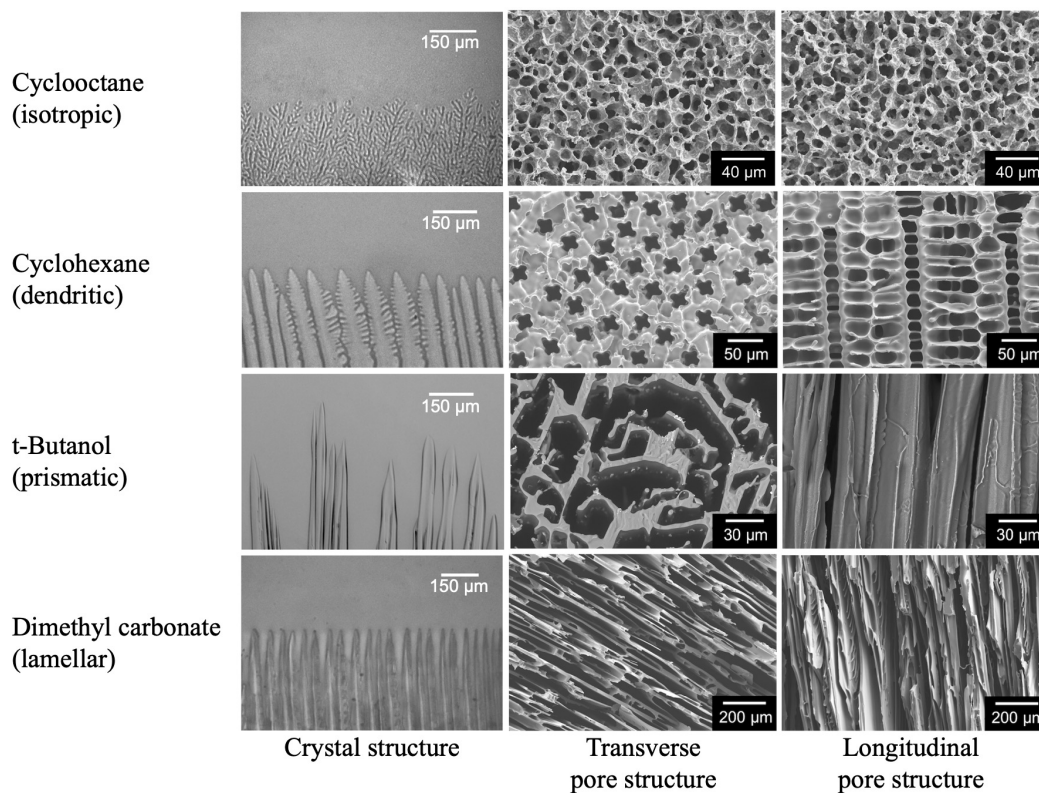


Figure 2.5: Optical images of the crystal structures formed from different solvents and the SEM images of their respective freeze-cast pore structure. Adapted from [125].

lower than that of the dendritic structures, resulting in an almost isotropic pore structure with freeze casting [2]. Freezing with low-entropic term solvents like cyclohexane results in a dendritic freezing front during solidification and dendritic pore structures [91].

As the anisotropy of the solvent increases, the crystal structure shows more faceted features and the resultant pores transitions from dendritic to lamellar. The prismatic structure from freezing t-butanol can be seen as a transitional state between dendritic and lamellar structures. The structure is neither unidirectional as dendritic structure nor is it bi-directional like the lamellar structure, reflecting a medium Jackson alpha-factor.

Finally, the highest-anisotropy solvent forms highly faceted crystals under larger supercooling to overcome the sparsity of the atom attachment site on the interface. The pore structure created by a high-anisotropy solvent such as dimethyl carbonate exhibits a series of smooth, parallel, and two-dimensional lamellae. The Jackson

alpha-factor is a good indicator of the growth mechanism and the anisotropy of the solidifying interface/crystals. In this thesis, dimethyl carbonate is used predominantly. However, if another pore morphology is desired, a different solvent can be chosen based on the Jackson alpha-factor to obtain that specific pore structure.

Additives and co-solvents are often used to alter the crystal formation, and consequently, the pore structure. Glycerol is a common cryoprotectant to reduce the crystal size, create smaller pores and increase interlamellar connections [200]. Polystyrene serves as a structuring agent and improves pore alignment of camphene freeze-cast structure [92]. Various alcohols, such as methanol, ethanol, and isopropanol (IPA), have been added to aqueous freeze-casting systems. Complex freeze-cast structures with more interlamellar bridges are obtained as a result of multi-phase systems and the interaction between alcohol additives and other functional additives such as dispersants and binders [119]. Large freezing point depression is present in co-solvents near the eutectic point [103]. A reduction of the pore size from 20 μm to sub-microns is achieved with a more than 30°C freezing point depression via a dioxane and dimethyl sulfoxide co-solvent system [87].

2.1.3 Solidification and Post-freezing Treatments

Solidification has direct influences on the resultant pore structure as the size and alignment of the solvent crystal links to those of the pore structure. In Section 2.1.2, common pore morphologies—dendritic, prismatic, and lamellar— were discussed. The major difference between them is the anisotropy of the solvent crystals.

Here, a distinction between the anisotropy and the instability of a crystal structure should be made. The anisotropy determines whether the crystal is faceted while the instability categorizes the crystal into planar, cellular, and dendritic regimes shown in the microstructure selection map (Fig. 2.6). Both faceted and non-faceted crystals can be in any of those regimes. For example, Fig. 2.3 (a, b) are both cellular arrays compared to a planar freezing front, yet (a) is non-faceted while (b) is faceted, which is related to the anisotropy. The nomenclature for pore structures refer to pores templated by faceted freezing dendrites as prismatic and lamellar structures, and those by non-faceted dendrites as "dendritic".

The microstructure selection map (Fig. 2.6) shows that different morphologies and crystal sizes can be accessed by two processing parameters, temperature gradient and crystal growth rate (freezing front velocity). Higher freezing front velocity gives rise to finer solidification structures, resulting in finer freeze-cast structures,

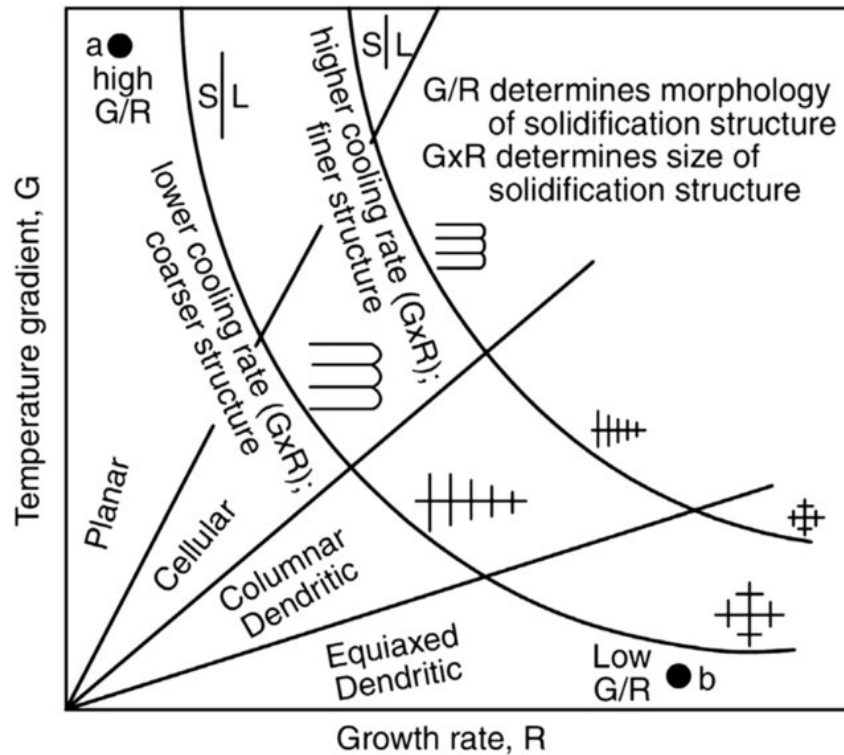


Figure 2.6: Microstructure selection map of crystal morphology and size depending on temperature gradient and growth rate [93] © 2003 John Wiley & Sons, Inc..

and ultimately, smaller pore sizes [49, 156]. Although increasing freezing front velocity and solids loading both reduce pore size, the resultant pore structures are different in porosity, pore wall thickness, and pore connectivity [124].

In a perfectly precise world, the freezing front is planar and at the freezing-point isotherm. However, thermal fluctuations cause interfacial instabilities, exacerbated by the constituent supercooling or undercooling arising from dissolved solutes in the alloy or multi-component system.

In such systems, solubility is higher in the melt than in the crystal. Solute are ejected in front of the freezing front when the solution solidifies into crystals, piling up into a concentration gradient in front of the advancing freezing front. Due to freezing point depression from solutes, the freezing point increases with distance from the interface. If the gradient of the freezing point exceeds the temperature gradient, the freezing front becomes unstable and transitions from planar, to cellular, and finally to dendritic (Fig. 2.7). This phenomenon has been thoroughly discussed by Mullins and Sekerka [121] and Losert et al. [113].

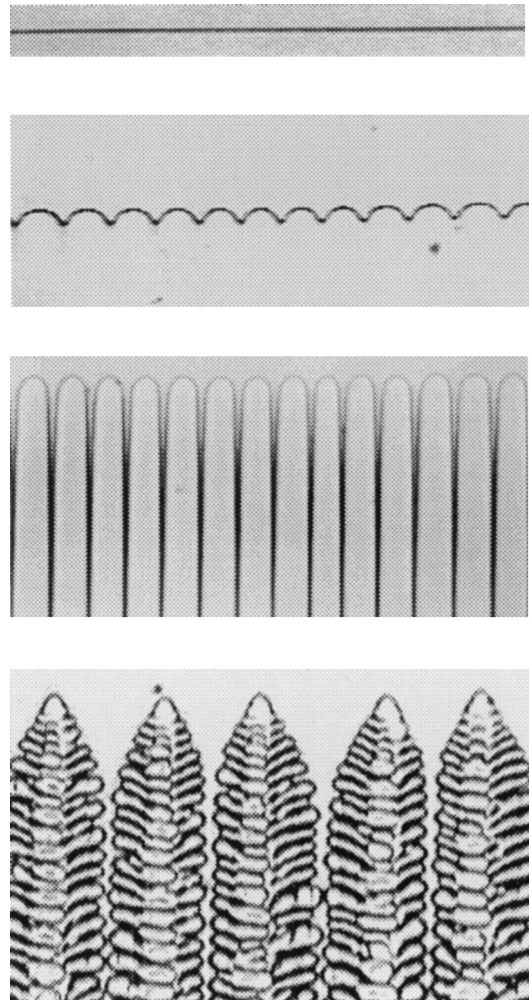


Figure 2.7: Microstructural transition from planar to cellular to dendritic freezing front (from top to bottom) in a succinonitrile and coumarin 152 binary alloy [113]. Copyright (1998) National Academy of Sciences, USA.

The direction and magnitude of the thermal gradient during solidification determines the pore alignment. Solvent crystals freeze in a direction influenced by the thermal gradient and the preferred growth orientation of dendrites. For two-dimensional lamellar structures obtained by freeze casting with water or dimethyl carbonate, a dual thermal gradient is often employed to obtain pore alignment in both directions. Bai et al. [8] introduces a dual thermal gradient by placing a wedge between the solution and the cooling device. The resultant pore structure shows a long-range pore alignment up to 5 mm.

Wang et al. [181] created a highly radial and centrosymmetric graphene oxide pore structure by prescribing a radial thermal gradient combined with a second gradient

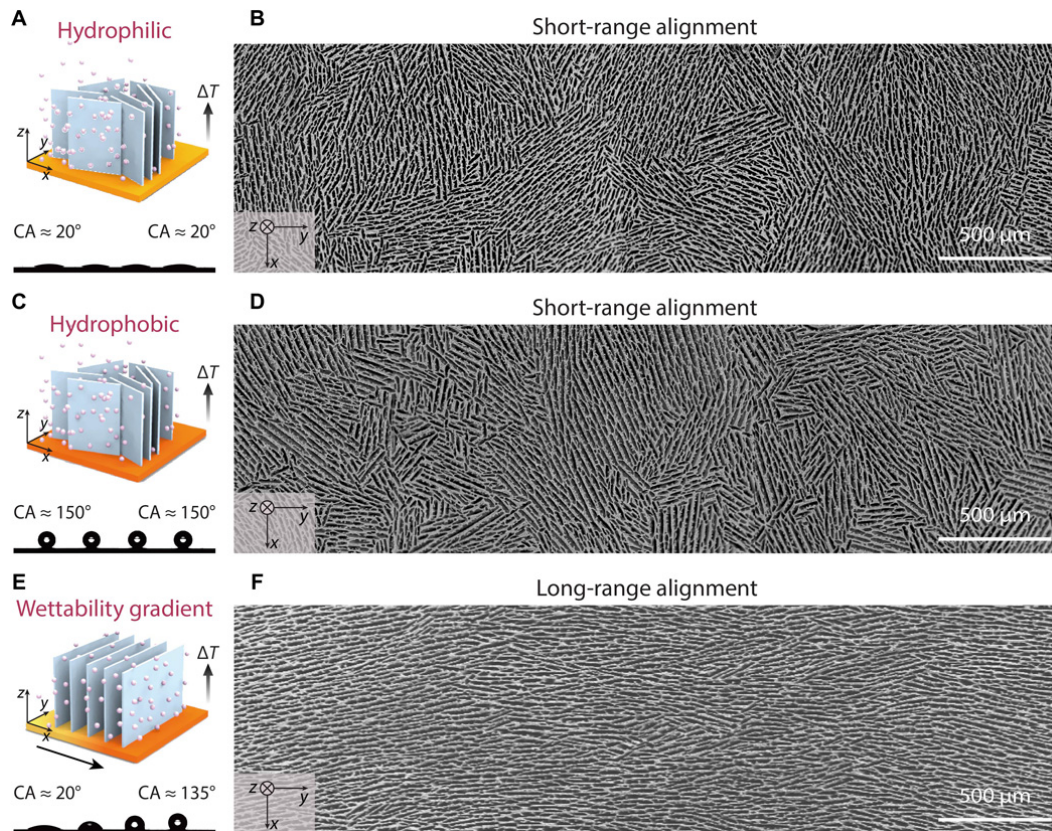


Figure 2.8: Solvent nucleation control via a wettability gradient enables a long-range pore alignment from [201]. Reprinted with permission from AAAS.

perpendicular to the first one. Pore alignment is further improved by limiting nucleation during solidification via a grain selector [127] or a wettability gradient [201].

In addition to the processing parameters discussed previously, external forces such as magnetic, electrostatic, or mechanical (acoustic) force have been used in freeze casting [128]. Fig. 2.9 (a) shows lamellar structures with a long-range alignment by applying a static or rotating magnetic field on the ceramic slurries containing iron oxide (Fe_3O_4) powders during freezing [137]. Tang et al. [173] demonstrates that with an aqueous alumina slurry without magnetic particles, the magnetic field reduces the pore size while the electric field creates aligned lamellae by influencing polar water molecules (Fig. 2.9 (b)). Acoustic waves from ultrasound create a tree-like composite structure with alternating dense and porous concentric rings, resistant to crack propagation (Fig. 2.9 (c)) [129].

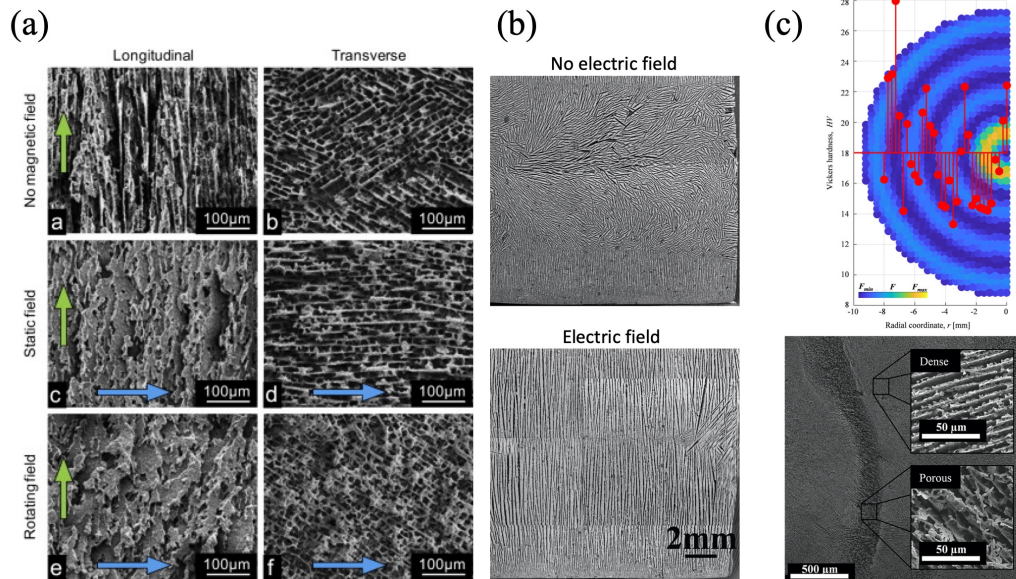


Figure 2.9: SEM images showing (a) the effects on alignment of a magnetic field on TiO_2 scaffolds containing 3 wt% Fe_3O_4 (reprinted from [137] with permission from Elsevier) (b) the effects on alignment of an electric field on aqueous slurries (reprinted from [173] with permission from Elsevier), and (c) the effects of acoustic waves on mechanical properties and pore structure [129].

2.1.4 Particle Engulfment

As previously stated in Section 2.1.1, small particles are more resistant toward engulfment by the freezing front. The two most common variables in particle engulfment are the particle size and the freezing front velocity. For a given particle size, there exists a critical freezing front velocity, above which particles are engulfed and below which particles are pushed by the freezing front.

During the process of solidification of a suspension, particles experience forces including a drag force from fluid motion, a repulsive force from surface energy, a buoyancy force, the gravitational force, an osmotic force, and other applied forces (magnetic, electric, mechanic, etc.) [128, 135]. The balance between the forces determines the critical freezing front velocity for engulfment.

Early engulfment models explored the solidification conditions for spherical particles and planar freezing fronts [175]. The planar freezing front develops a slight curvature when the thermal conductivity of the particle differs from that of the solvent [89] due to the change in heat flux. Shangguan et al. [161] established the mathematical relation between the curvature of freezing front and the relative

thermal conductivity between the particle and the solvent. The shape of the freezing front could cause order-of-magnitude differences in the drag force.

Particles near the freezing front could obstruct the ejection of solutes or impurities into suspensions, resulting in a solute pile-up. The planar freezing front is concave near the particle as a result of freezing point depression caused by the pile-up [138]. Other factors, such as particle roughness, the Gibbs-Thomson effect, and particle wettability, may also influence particle engulfment [19, 26, 134].

If particles are continuously pushed by a planar freezing front, a compacted particle layer builds up in front of the freezing front, exerting an extra viscous force on the particles from particle-particle interaction [151].

If the freezing front is dendritic, a unique dendritic tip radius can be determined for a given freezing front velocity and a thermal gradient along with the solute concentration [14, 17, 33, 98]. The relative location of particles and dendrites affects the outcome of the particle-freezing front interaction. Particles between dendrites are trapped in the inter-dendritic space rather than being engulfed or pushed by the freezing front, termed particle entrapment [52, 53].

Bouville et al. [20] investigates the interaction between high-aspect ratio particles and a lamellar freezing front by modeling faceted particles as clusters of spheres. They deduce that a self-aligning effect on particles comes from compacting motion of thickening dendrites after particle entrapment. The proposed mechanism cannot explain interlamellar bridges seen in freeze-cast structures of faceted particles, nor can it reproduce particle engulfment. The model simplifies the drag force of faceted particle to be the sum of the drag force of individual spheres regardless of the different flow motion arising from having faceted particles. While much effort has been expended on particle engulfment theory, freeze casting high-aspect ratio particles has yet to be properly modeled. This topic is a promising area for research.

2.1.5 Sintering/pyrolysis and Post-freeze Casting Treatments

The porosity of the pore wall structure from ceramic powders is controlled by the sintering temperature and time. Increasing sintering temperature promotes closure of closed pores in the freeze-cast pore walls, decreasing the overall porosity and increasing the mechanical strength of the walls, and therefore, the structure [59]. In contrast, partial sintering or sintering at lower temperatures contributes to higher porosity and surface area [142, 159].

During pyrolysis, preceramic polymers start to degrade around 400°C, opening mi-

ropores (<2 nm) in the structure, as described in detail in 2.3.1. As the temperature increases to 800-1200°C polymers are completely transformed into ceramics and the micropores close up. Wilhelm et al. [186] utilize this property of preceramic polymer and fabricates a polymer-ceramic hybrid material, ceramer, raising the surface area of ceramers close to that of activated carbons.

Catalysts in preceramic polymers promote the formation of nanowires on the surface of pore walls. The pyrolysis atmosphere is shown to affect the type of nanowires formed. Pyrolysis in nitrogen produces silicon nitride nanowires while SiC nanowires are obtained pyrolyzed in argon [177, 178]. Post-sintering processes, such as deposition of a mesoporous (2-50 nm) layer, increase the surface area of the underlying pore scaffold [39].

2.2 Self-assembled Block Copolymers

A block copolymer (BCP) is a copolymer composed of blocks of repeated units. In the melt, diblock and triblock copolymers often self-assemble into structures with nanosized features due to the energy balance between the interfacial energy and the core-chain stretching. The size and the morphology of such features depend on the relative fraction of each block and the block length [25, 116].

However, in a dilute solution, the polymer and solvent interaction is dominant [82]. A symmetric ABA triblock copolymer system is especially of interest for its capability to generate a thermoreversible gel [120, 157]. In the process of preparing a thermoreversible gel, an ABA triblock copolymer is dissolved in a midblock selective solvent at an elevated temperature where both A and B blocks are dissolved in the solvent. As the temperature decreases to the critical micelle temperature (CMT), the A endblocks aggregate into micelles while midblocks being well-solvated and connecting micelles, forming an interconnected network. If the temperature decreases further, the system goes through a glass transition. The endblocks are no longer free to exchange between micelles. The block copolymer system goes from the viscous to the viscoelastic, and finally to the elastic mechanical state as the temperature decreases from above CMT, to below CMT, and to below the glass transition temperature, as shown in Fig. 2.10 [51, 157]. The process is reversed upon heating, hence the name thermoreversible gel. The thermally reversible nature of thermoreversible gelcasting allows for a longer processing window—the system can remain in the liquid state as long as needed above CMT—and for recyclability from failed casts.

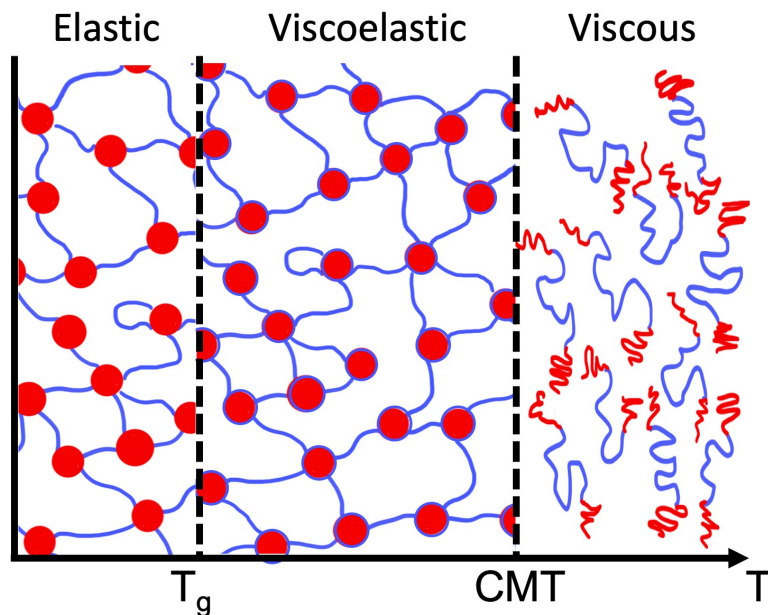


Figure 2.10: Schematic of the structure and the mechanical property of PMMA-PnBA-PMMA triblock copolymer gel as a function of temperature. Reproduced from [51].

Common triblock copolymer systems include styrene- and acrylic-based block copolymers. Styrene-based systems are used as pressure-sensitive adhesives [88], substrates for microfluidic systems [170], and gate insulators [31]. In addition to aforementioned applications, acrylic-based systems find uses in porous ceramic processing [56]. Poly(methyl methacrylate)-poly(*n*-butyl acrylate)-poly(methyl methacrylate) or PMMA-PnBA-PMMA is particularly advantageous among acrylic-based systems because its CMT is above room temperature but lower than 100°C, so a water bath is sufficient to induce the whole range of transition [157]. In the process of creating a porous ceramic with the block copolymer, ceramic powders are dispersed in the block copolymer solution above CMT. The ceramic-block copolymer solution is then cast into the desired bulk shape. As the temperature decreases below CMT, the solution gels and retains the shape of the mold. Finally, the porous ceramic is achieved after subsequent drying, burnout of block copolymer, and sintering [162].

In theory, the block copolymer can be used as a sacrificial template for pores less than 100 nm. In reality, the relative size of the template features to that of the precursor particles determines the resolution of the negatives/replicates [46]. It is difficult to obtain well-dispersed suspensions with nanoparticles small enough to replicate the features of the self-assembled block copolymer where the size of the

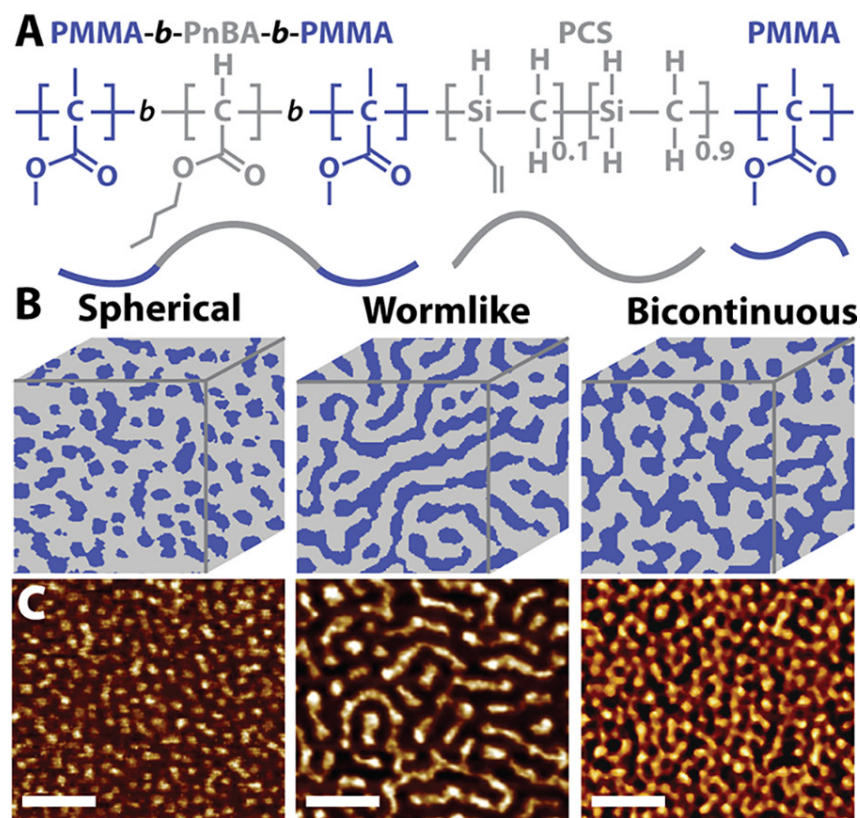


Figure 2.11: (A) Chemical structures of PMMA-PnBA-PMMA, polycarbosilane, and PMMA. (B) Schematic of resultant morphologies of the gel system and (C) the corresponding atomic force microscopy (AFM) images. Scale bars are 100 nm [21].

features is often in the range of 10 to 100 nm [105]. Porous structures created with thermoreversible gel casting with ceramic powders typically require additional sacrificial fillers to serve as templates [56, 162].

One could overcome this obstacle by choosing preceramic polymers as precursors instead of powders. Preceramic polymers have a radius of gyration of less than 10 nm [55, 105, 192], small enough to replicate the features of the self-assembled block copolymer. Rueschhoff et al. [147] create porous ceramic films by depositing a thin film of a PMMA-PnBA-PMMA and polycarbosilane blend. The self-assembled BCP acts as a template for the polycarbosilane and burns away while polycarbosilane is converted into SiC after pyrolysis. Pore morphologies such as interconnected micelles, worm-like, and bicontinuous structures (shown in Fig. 2.11) are obtained by varying the PMMA monomer concentration and relative block length of PMMA to PnBA. The PMMA-PnBA-PMMA and polycarbosilane blend that produces interconnected micelles is used for the study in this thesis.

2.3 Preceramic Polymers

2.3.1 Overview of Polymer-derived Ceramics (PDCs)

Traditionally, ceramic precursors are ceramic powders that can be molded and sintered into dense ceramics. However, since 1960, ceramics have also been synthesized by the pyrolysis of preceramic polymers. Preceramic polymers, as the name suggests, are polymers that are converted into ceramics at elevated temperatures [18, 36, 123].

Preceramic polymers have numerous advantages compared to ceramic powders or other molecular precursor routes. Since preceramic polymers are in the polymeric state before the final conversion process, they open avenues of polymer processing techniques, such as injection molding, extrusion, fiber drawing, and additive manufacturing, that are difficult to use with ceramic powders. They are also readily machinable and prevent tool wear and fracture from machining finishing ceramic components. The radii of gyration of polymers are often smaller than the sizes of commercial ceramic powders, increasing the resolution of replicating templates [55, 105, 192]. Pyrolysis temperatures are generally lower than the sintering temperatures [126]. Moreover, reducing the residual porosity often requires high pressures during ceramic powder sintering, increasing the processing cost.

Preceramic polymers do not have drying problems common to the sol-gel process, which allows almost net-shape forming with fillers [69]. The commercial preceramic polymers are relatively stable and safe to use, one part due to low toxicity compared to monomers used in gelation and the other part because of flammable solvents are not necessary for the processing like ceramic slurries. Theoretically, preceramic polymers have an infinite processing window as they can be processed in the melt and do not require gelation to hold the final shape [36].

These advantages make preceramic polymers a facile precursor for ceramic composites [136, 152], coatings [40, 174], and porous ceramics [35, 95, 179], and in tape casting [68, 75], and additive manufacturing [29, 108, 182].

Preceramic polymers can be grouped into different categories shown in Fig. 2.12 based on the group in the polymer backbone and the sides groups in the polymer. The following sections focus on the two preceramic polymers used in this study, polysilsesquioxane (a subtype of polysiloxane, $\text{CH}_3\text{-SiO}_{1.5}$) and polycarbosilane.

Typically, the processing of preceramic polymers to polymer-derived ceramics includes three steps—shaping and cross-linking, pyrolysis, and crystallization—

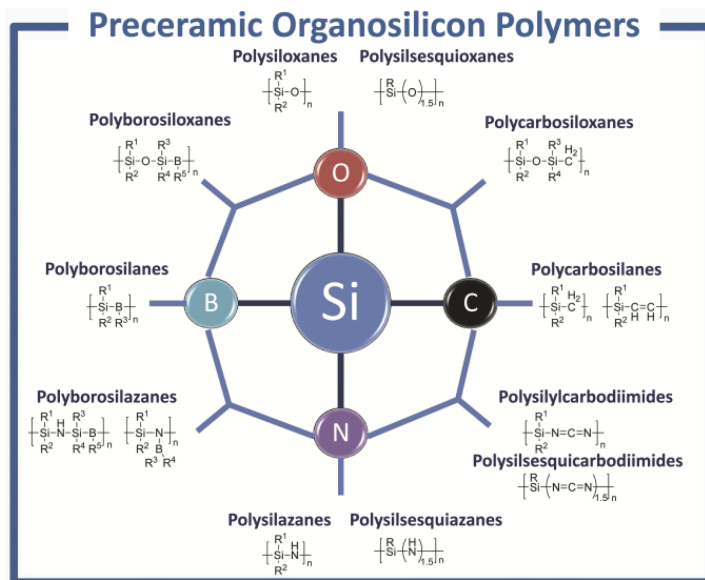


Figure 2.12: Typical classes of silicon-based preceramic polymers as precursors of polymer derived-ceramics [36] © 2010 The American Ceramic Society.

shown in Fig. 2.13. Most polymer shaping techniques are conducted at temperatures below 300°C. Before or during the shape-forming step, the polymers are often cross-linked to form a thermoset and retain its shape via condensation or addition. Initiation of cross-linking can be achieved by heating or by adding catalysts [10, 72, 180]. Other cross-linking methods include oxidative, e-beam, and UV curing but they often come with size limitations or unfavorable side-effects [36]. Cross-linking determines the rheology of the melt and the yield of PDCs [123, 172, 188].

Preceramic polymers (PCPs) start decomposition at about 400-600°C, emitting carbon and hydrogen-based oligomers. Pyrolysis is accompanied by a volume shrinkage, a weight loss, and the formation of micropores [176]. These are problematic for fabricating dense bulk materials as a shrinkage and porosity often facilitate crack formation. Fillers can be used to ameliorate this problem [75]. Pyrolysis of PCPs completes at 800-1100°C, converting polymers into amorphous ceramics, often with short-range orders or nanodomains. Both polysilsesquioxane and polycarbosilane are converted into silicon oxycarbide (SiOC) after pyrolysis at temperatures below 1100°C. Pyrolysis or heat-treatment at temperatures above 1100°C promotes crystallization and converts amorphous SiC to β -SiC with large volume shrinkage.

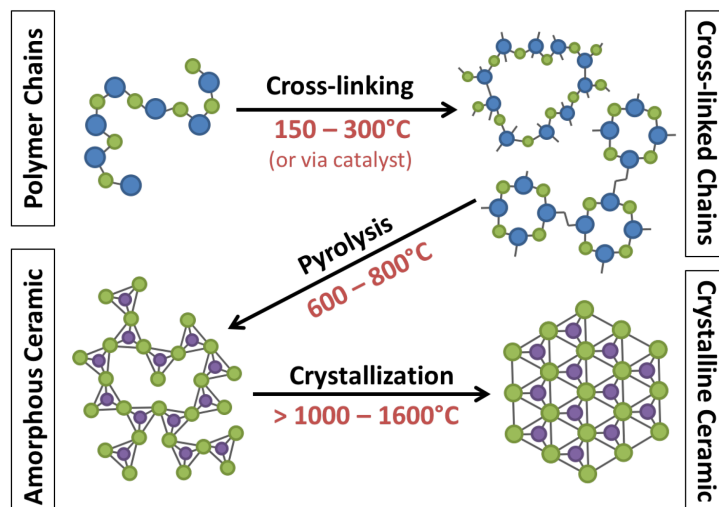


Figure 2.13: Schematic of the processing and chemical structures of preceramic polymers to polymer-derived ceramics [68, 125].

2.3.2 Polysilsesquioxane

Cross-linking of polysilsesquioxane occurs at 100-150°C without a catalyst [10, 189]. Harshe et al. [72] showed that mass loss occurs between 500°C and 1100°C in the pyrolysis of polysilsesquioxane polymer, accompanied by the emission of water, ethanol, and methanol. The loss of Si-CH₃ and C-H bonds at 1000°C analyzed from Fourier-transform infrared spectroscopy (FTIR) [125] signals the completion of the polymer-to-ceramic transition. SiOC pyrolyzed at 1300°C are shown to be X-ray amorphous and forms crystalline β -SiC at temperatures beyond 1300°C.

Two models of the microstructure of polysiloxane-derived SiOC have been proposed as shown in Fig. 2.14. Model 1 describes the SiOC microstructure as silica nanodomains of silica tetrahedra surrounded by interdomain boundaries of graphene layers and the SiC_xO_{4-x} mixed bonds between silica and graphene layers [150, 153].

Model 2 depicts an interconnecting network of the oxygen-rich SiC_xO_{4-x} units with the carbon-rich SiC_xO_{4-x} units filling the space between the network and the free carbon nanodomains. In Model 2, free carbon may form spatially bicontinuous nanodomains if there is more excess carbon as in carbon-rich SiOCs. Recent evidence of experimentally characterized the mass-fractal dimension of the oxygen-rich SiC_xO_{4-x} units is more consistent with Model 2 [184].

Silica in the SiOC remains amorphous up to 1500°C despite the fact that pure silica crystallizes into cristobalite at 1000°C [144, 183]. The inhibition of crystallization

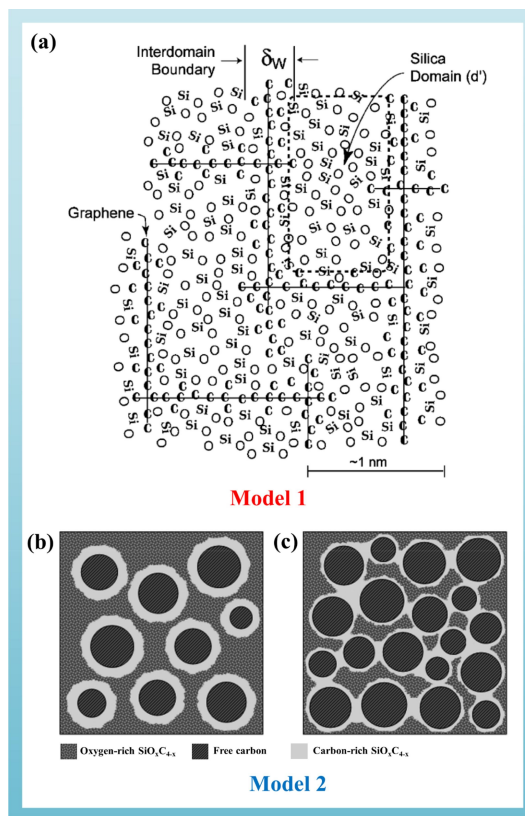


Figure 2.14: Two proposed models of the microstructure of polysiloxane-derived SiOC. Reprinted from [183] with permission from Elsevier.

is likely due to the presence of free carbon [94, 144, 166].

2.3.3 Polycarbosilane

The majority of mass loss in the pyrolysis of polycarbosilane, arising from the escape of hydrogen, methane, and silanes, occurs from 200 to 800°C. Mass loss and volume shrinkage remain fairly constant between 800-1200°C with no gas evolution, indicating the completion of pyrolysis of polycarbosilane at 800°C [100]. Comparing FTIR peaks of cross-linked polycarbosilane and that of its PDCs at 800°C demonstrates that C-H, Si-H, CH_2 peaks disappear, confirming the transition to ceramic state [147].

The microstructure of amorphous SiOC from polycarbosilanes (with oxygen contamination during processing) consists of amorphous SiC nanodomains and free carbon nanodomains. Oxygen contamination results in $\text{SiC}_x\text{O}_{4-x}$ units filling the space between these two nanodomains [183]. Above 1300°C, precipitation of nanoscale β -SiC crystallites starts. However, the complete transformation into bulk

SiC requires the decomposition of O-rich regions and the destruction of the free carbon network, occurring at 1400-1500°C [136]. Chemical compositions of PDCs from polysilsesquioxane and polycarbosilane are listed in Table 5.1.

SiC WHISKER-REINFORCED COMPOSITES

Material in this chapter is reproduced in part from "Porous SiC-SiOC composites through particle engulfment of high-aspect ratio particles during freeze casting", C.T. Kuo, C.H. Keck, K.T. Faber; *Manuscript in preparation*. The work was done in collaboration with Carl H. Keck and Katherine T. Faber. T. Kuo fabricated and characterized SiC composites using SEM and MIP, their permeabilities, and compressive strengths, developed the model and simulated solidification process for freeze casting high-aspect ratio particle, and wrote the manuscript. C.H. Keck calculated the bridge density and measured the viscosity of the polymer solution. K. Faber supervised this work.

3.1 Introduction

As previously mentioned in Section 1.1, two of the most critical properties for most applications of porous solids are strength and permeability. In freeze casting, the most common directional pore structures are lamellar and dendritic [156]. Lamellar structures have a higher permeability, but a lower strength compared to dendritic structures [125]. They often fail in shear with lamellae slipping past one another. Attempts have been made to increase compressive strength while retaining high permeability of lamellar structures by introducing bridges between lamellar walls to prevent shear failure [64, 97]. Bridges, in this case, were a result of large Al_2O_3 platelets in a fine Al_2O_3 powder suspension or of carbon nanotube (CNT) agglomerates in a CNT-polysiloxane polymer suspension.

The current theories behind the formation of interlamellar bridges are not sufficiently sophisticated to describe actual solidification conditions encountered in freeze casting high-aspect ratio particles. Some early models adopted spherical particles and planar freezing fronts or planar freezing fronts with a slight curvature as a result of the differences in thermal conductivity between particles and the solvent [89, 161, 175]. In more recent models, impurity concentrations, particle size, and the Gibbs-Thomson effect are included in determining the shape of freezing fronts [26, 27, 138]. However, the curvature of the freezing front has always been a response to the freezing front's proximity to a particle. The modeled solidification conditions in these works are common in zone refining, where a planar freezing

front is often characteristic.

In contrast to planar freezing fronts in zone refining, lamellar or dendritic freezing fronts are necessary in freeze casting to induce phase separation to create pore structures [30]. The curvature of the freezing front is not a response to the proximity of the particles to one another in freeze casting, but is rather uniquely determined by solidification conditions. Microstructure selection maps show the freezing front morphology (planar, cellular, and dendritic freezing front) as a function of freezing front velocity and temperature gradient [77, 99]. In the dendritic regime, a unique dendritic tip shape can be determined for a given freezing front velocity and a thermal gradient along with the solute concentration [14, 17, 33, 98].

As a result, the previous models often fall short in describing the solidification conditions of freeze casting. Recently, Bouville et al. modeled the interaction between high-aspect ratio particles and a lamellar freezing front [20]. However, the high-aspect ratio particles were treated as a cluster of spherical particles. The force acting on the high-aspect ratio particles was a summation of the forces on individual spherical particles without considering overall fluid dynamics, the origin of the aforementioned force. Therefore, we propose a new model, specifically designed to accurately describe the solidification conditions with high-aspect ratio particles and a lamellar freezing front in freeze casting.

In this chapter, the freeze casting of high-aspect ratio particles is examined by experiments, modeling and simulation to develop a firmer understanding of freezing front-particle interactions. First, interlamellar bridges are introduced via freeze casting with silicon carbide (SiC) whisker-polysiloxane preceramic polymer suspension. The resultant microstructure, permeability, and compressive strength of SiC whisker-silicon oxycarbide (SiOC) porous composites are examined. A 2D freezing setup is implemented to observe solidification *in situ* and a new particle engulfment model is proposed to describe the phenomenon in the 2D solidification experiment. Finally, the experimental results are compared with the calculated and the simulated results based on the proposed model.

3.2 Experimental Procedures

3.2.1 Freeze Casting

3.2.1.1 Materials and Synthesis

Silicon carbide whiskers (purity: >90% whisker, diameter: <2.5 μm , length: 50-80 μm , US Research Nanomaterials, Inc., TX, USA) were chosen as the high-aspect

ratio particles in this study for their relatively simple shape and negligible thermal expansion mismatch with the SiOC matrix. As-received SiC whiskers are confirmed to have a high aspect ratio (>10) and are shown to be faceted in Fig. 3.1.

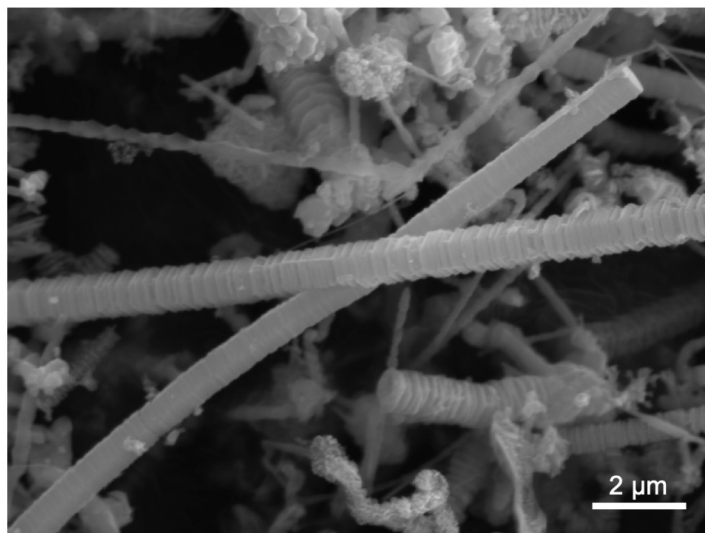


Figure 3.1: An SEM image of as-received faceted SiC whiskers.

Twenty vol.% preceramic polysiloxane polymer (Silres® MK Powder, CH₃-SiO_{1.5}, Wacker Chemie, Munich, Germany) and 3 wt.% (of SiC) dispersant (Hypermer KD1, Croda, NJ, USA) were dissolved in dimethyl carbonate (DMC, Sigma-Aldrich, MO, USA). Then, 10, 20, 30 vol.% SiC whiskers of the solid loading (MK+SiC) were dispersed in MK-DMC solution and sonicated for 20 minutes. Two wt.% of crosslinking agent (N-(2-Aminoethyl)-3-aminopropyltrimethoxysilane, Sigma-Aldrich, MO, USA) was added to the SiC-MK-DMC suspension before freezing. The suspension was poured into a 24-mm diameter glass mold and quenched at -35°C. Fig. 3.2(a) shows a schematic of the freeze setup. Each frozen sample was moved into the freeze dryer until the solvent was removed, leaving a porous polymer ceramic composite behind. The SiC-MK composites were then pyrolyzed at 1100°C under argon for 4 hours and converted into porous SiC-SiOC ceramic composites. A porous MK-derived SiOC ceramic was fabricated as a control sample using a similar procedure without adding SiC whiskers and KD1, or sonicating. The compositions of the suspensions and solution are listed in Table 3.1.

Table 3.1: Composition of suspension and porosity of the pyrolyzed porous composites.

SiC/Solid (vol.%)	MK (ml)	SiC (ml)	KD1 (g)	DMC (ml)	Porosity (%)
0	1.00	0.00	0.00	4.00	76.00
10	1.00	0.11	0.01	3.89	76.88
20	1.00	0.25	0.02	3.75	76.03
30	1.00	0.43	0.04	3.57	73.60

3.2.1.2 Characterization

Microstructure and bridge density were characterized using scanning electron microscopy (ZEISS 1550VP FESEM, Carl Zeiss Microscopy GmbH, Jena, Germany) and a mercury intrusion porosimeter (MIP, AutoPore IV 9500, Micromeritics Instrument Corp., Norcross, GA, US). Pyrolyzed samples were sectioned 3 mm from the base of the sample, perpendicular to the freezing direction. For bridge density measurement, samples were similarly prepared, but infiltrated with epoxy (EpoColor, Buehler, IL, USA), and polished.

Freeze-cast cylinders, 13-mm in diameter and 8-mm tall, were drilled from pyrolyzed samples along the freezing axis for compressive strength measurements. The top and the bottom sides were capped with a high-stiffness acrylic (VariDur 3003, Buehler, IL, USA) to prevent crushing during mechanical testing, common in porous ceramics [117]. Two sets of self-aligning washers were used to ensure the force was applied along the freezing axis of the samples. A pair of SiC blocks were placed between the sample and the washers to ensure an even distribution of force on the sample. The samples were compressed at a displacement rate of 0.05 mm/min and the maximum load in the load-displacement curve was used to calculate the compressive strength. At least three samples were tested for each condition.

Permeability measurements were performed on 13-mm diameter and 5-mm tall pyrolyzed cylinders. The perimeters of the samples were enclosed with VariDur 3003 acrylic to prevent leakage. The samples were clamped inside a tube with a pump forcing water through the samples. A pressure gauge was used to measure fluid pressures. Further details of the experimental setup can be found in [97]. Flow rates were measured at several pressures from 6 to 70 kPa. The permeability was

determined with the Darcy-Forchheimer equation [45, 203]:

$$\frac{\Delta P}{l} = \frac{\mu}{k_1} v + \frac{\rho}{k_2} v^2 \quad (3.1)$$

where ΔP is the pressure drop across the sample, l is the height of the sample, v , μ and ρ are the flow velocity, dynamic viscosity, and density of water, respectively, and k_1 and k_2 are intrinsic and inertial permeabilities, respectively. Given the linearity of the data, the inertia permeability (k_2), accounting for the non-linear part of permeability, is ignored. Three samples were tested for each condition.

3.2.2 Two-dimensional Solidification Experiments and Simulations

3.2.2.1 Experimental Setup

To observe the freezing process in real-time, a two-dimensional (2D) solidification setup was designed, and is shown schematically in Fig. 3.2(b). A 30 μL suspension was placed between two glass slides to produce a 7- μm liquid film to observe dendrite/whisker interactions. The left side of the bottom glass slide was in contact with the cold finger to create a thermal gradient parallel to the glass slides. The suspension was composed of 0.2 vol.% SiC whisker and 20 vol.% MK preceramic polymer solvated with 79.8 vol.% DMC. The concentration of whiskers was dilute to minimize the interparticle interaction and facilitate observation. The concentration of MK polymer was kept constant so that the freezing front shape, size, and dendritic spacings, would be similar to those in freeze casting. The copper cold finger was quickly cooled to and held at -13°C , the temperature producing lamellar spacings and freezing front velocities closest to those producing bulk samples in this freeze casting study. A digital microscope (Digital USB Microscope Camera OT-V1, Opti-Tekscope) was used to record solidification.

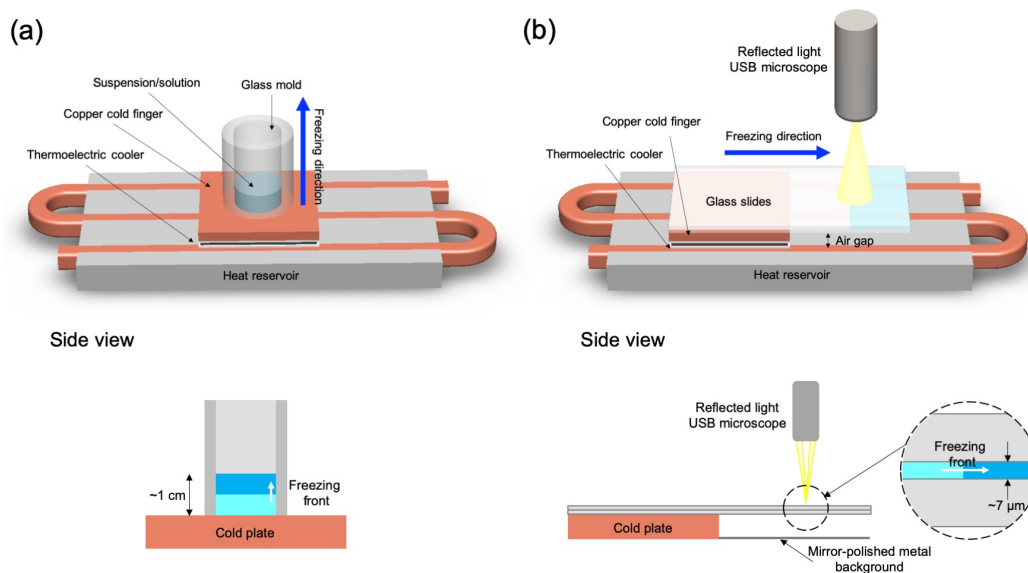


Figure 3.2: A schematic of (a) freeze casting setup and (b) 2D solidification setup.

3.2.2.2 Viscosity

Before the viscosity measurement, 2 wt.% cross-linking agent was added into the solution of 20 wt.% MK-DMC solution at room temperature ($\sim 25^{\circ}\text{C}$). The viscosity measurements were conducted within 20 minutes of the cross-linker addition. This ensured that the viscosity was similar to that displayed during freeze casting. After ~ 4 hours, viscosity changed drastically. The viscosities were determined at several strain rates from 1 to 100 s^{-1} using ARES RFS rheometer (TA Instruments, New Castle, DE, USA) with a cone-and-plate fixture, with a 50-mm diameter parallel cone-plate with a 1° canted surface. The solution displayed shear thinning and the viscosity at the highest strain rate (100 s^{-1}) was used in this study.

3.2.2.3 Surface Energy

To determine the surface energy between the liquid MK-DMC solution and a SiC whisker, γ_{WL} , a droplet experiment was performed. SiC whiskers are assumed to have an oxide layer; SiO_2 was confirmed by X-ray powder diffraction (not shown) of as-received SiC whiskers. A slab of fused silica was cleaned with acetone and DI water and then heated in a drying oven at 100°C for six days. Twenty wt.% MK-DMC solution was dropped onto the silica slab. Contact angles from five optical images were analyzed.

3.2.2.4 Freezing Simulations

Freezing the SiC whisker-polysiloxane-DMC suspension was modeled with a MATLAB script consisting of a 2D simulation cell of $100 \times 300 \mu\text{m}^2$. The cell comprised randomly distributed whiskers and a set of dendrites. The freezing front advanced from left to right in 25-ms time intervals. Each whisker had a randomly generated starting angle and position. The freezing front velocity and the lamellar spacing used in the simulation were measured from a series of SEM images of pore structures and solidification videos of freeze casting. The number of dendrites and whiskers were determined by the lamellar spacing and SiC concentration, respectively. The position offsets were calculated from the distance between each whisker and its nearest dendrite. The values of the input variables are shown schematically in Fig. 3.3, and their values are listed in Table 3.2.

The torque on whiskers were calculated along with the angles that SiC whiskers changed as the freezing front advanced and time progressed. If a whisker was not pushed aside before the freezing front reached within the minimal distance between a particle and freezing front (h), the drag and repulsive force were calculated to determine if the whisker was pushed or engulfed by the freezing front. A whisker would be engulfed if the drag force was larger than the repulsive force and pushed aside if not. Due to the variance in simulation results addressed in Section 3.3.2.4, each engulfed whisker fraction is averaged over 2000 times through repeated simulations for each condition to gain an overall sense of engulfment.

Table 3.2: Values of input variables for simulation.

SiC whisker height, width, d	$2 \mu\text{m}$		
SiC whisker length, L	$70 \mu\text{m}$		
Molecular distance, a_0	$2 \times 10^{-10} \text{ m}$		
Minimal distance, h	$2 \times 10^{-10} \text{ m}$		
Density of SiC whisker, ρ	3216 kg/m^3		
Dynamic viscosity, η	$0.02179 \text{ Pa} \cdot \text{s}$		
*Dendritic tip slope, a	2.83		
	10 vol.%	20 vol.%	30 vol.%
SiC concentration in suspension	2.22%	5.00%	8.57%
*Freezing front velocity, V_{ff}	$22.45 \mu\text{m/s}$	$32.05 \mu\text{m/s}$	$31.9 \mu\text{m/s}$
*Lamellar spacing	$26.66 \mu\text{m}$	$43.81 \mu\text{m}$	$41.52 \mu\text{m}$

* = determined by experiment

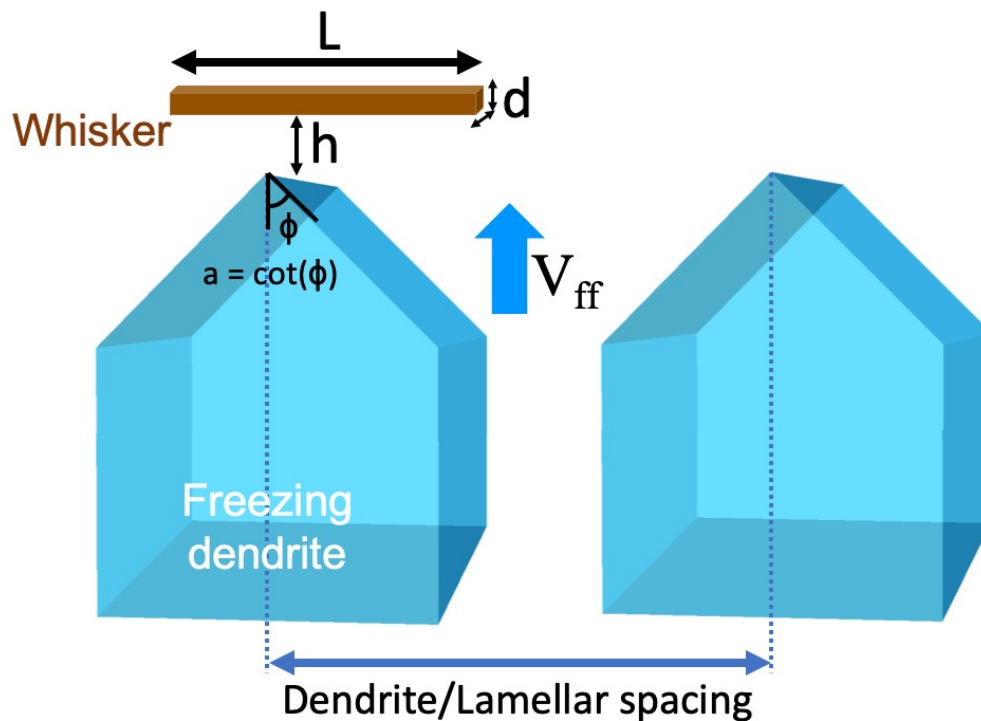


Figure 3.3: A schematic of input variables used in freezing simulation.

3.3 Results and Discussion

3.3.1 Freeze-cast Samples

3.3.1.1 Pore Structures

Shown in Fig. 3.4(a) through (d) are cross-sections of freeze-cast lamellar structures with different concentrations of whiskers. Without added whiskers, few SiOC bridges form during pyrolysis as a result of the polysiloxane being phase-separated into the spaces between the secondary arms of the dendrites during solidification. In contrast, the structures with 20 and 30 vol.% of whiskers have many bridges. In addition to the SiC-SiOC bridges (blue circles), there are many bridges of SiC whiskers (yellow circles), shown in Fig. 3.4(e). SiOC bridges are thicker and continue along the lamellar walls, whereas whisker bridges are thinner and act as individual pillars. We argue that these two bridges were formed via different mechanisms, as evidenced by their different morphologies. SiC-SiOC bridges formed by polysiloxane are phase-separated into the spaces between secondary arms, whereas whisker bridges formed by SiC whiskers are engulfed by the freezing front.

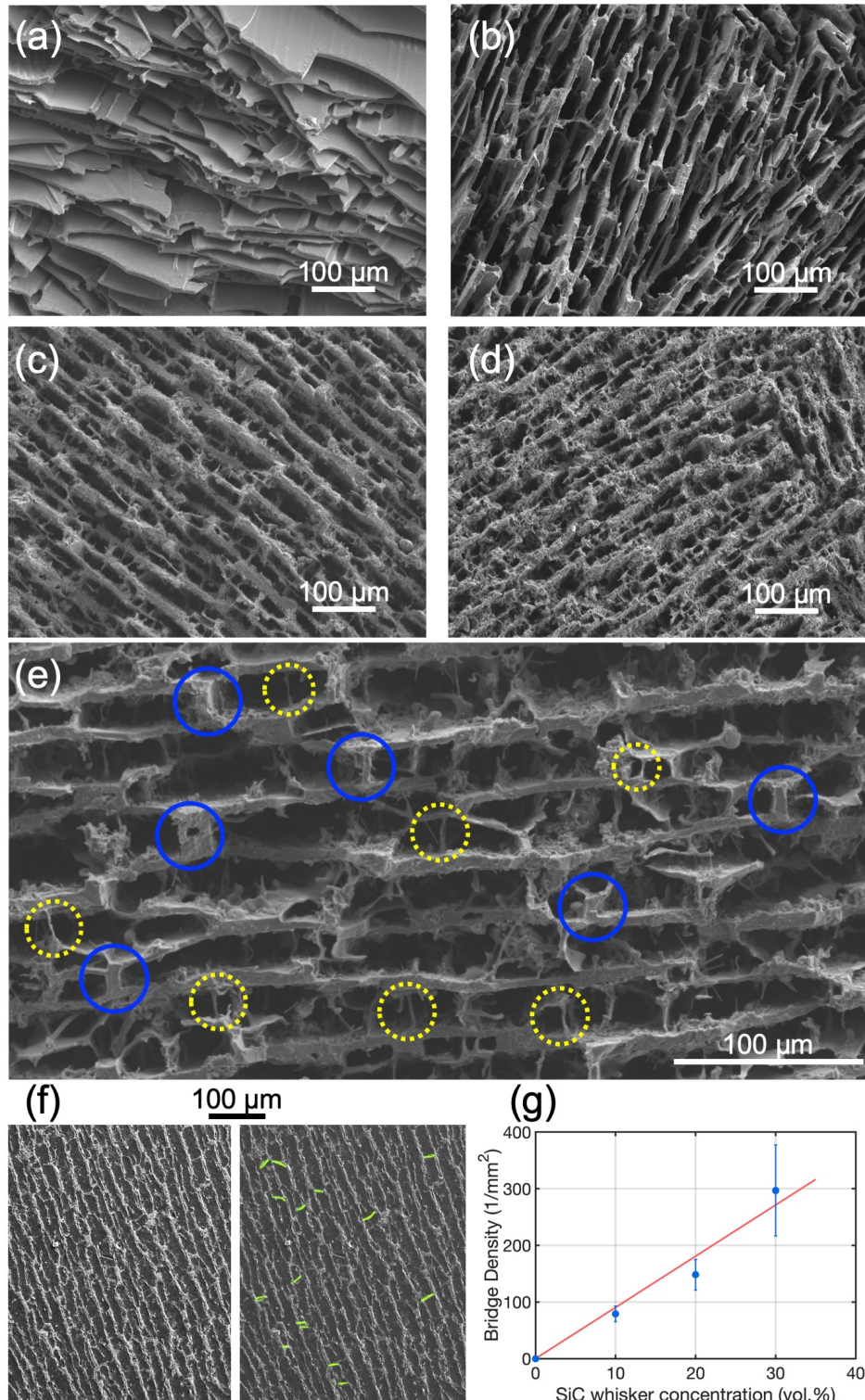


Figure 3.4: SEM images of freeze-cast lamellar structures with (a) 0, (b) 10, (c) 20, (d) 30 vol.% SiC whiskers and (e) 20 vol.% SiC whiskers freeze-cast lamellar structures with SiC-SiOC bridges (blue circles) and SiC whiskers (yellow circles) bridges (f) Example images of bridge density measurements. Green lines mark the counted whisker bridges. (g) Bridge density as a function of the whisker concentration. Error bars represent ± 1 standard deviation.

An important observation is that the whisker bridges are largely perpendicular to the lamellae, indicating the presence of an angular-bias during particle engulfment, leaving behind whisker bridges that are almost all perpendicular to the freezing dendrites, and hence, the lamellae. Whiskers that are parallel to the freezing dendrites during solidification are embedded in the pore walls after freeze casting. The same phenomena can also be seen in freeze casting of SiC whiskers [57], CNTs [70], alumina platelets [63], and graphene sheets [181], showing that the alignment of high-aspect ratio particles is the norm rather than an anomaly. This demonstrates two important phenomena unique to freeze casting high-aspect ratio particles, alignment and partial engulfment of particles.

To quantify the number of bridges, freeze-cast samples were infiltrated with epoxy and sectioned for imaging. After infiltration, only bridges on the sectioned plane were visible (Fig. 3.4(f)). Only SiC whisker bridges were used to calculate the bridge density. SiC-SiOC bridges formed by phase separation into secondary arms were not counted. The number of bridges increases in proportion to the increasing concentration of whiskers with an R^2 value of 0.9661 (Fig. 3.4(g)).

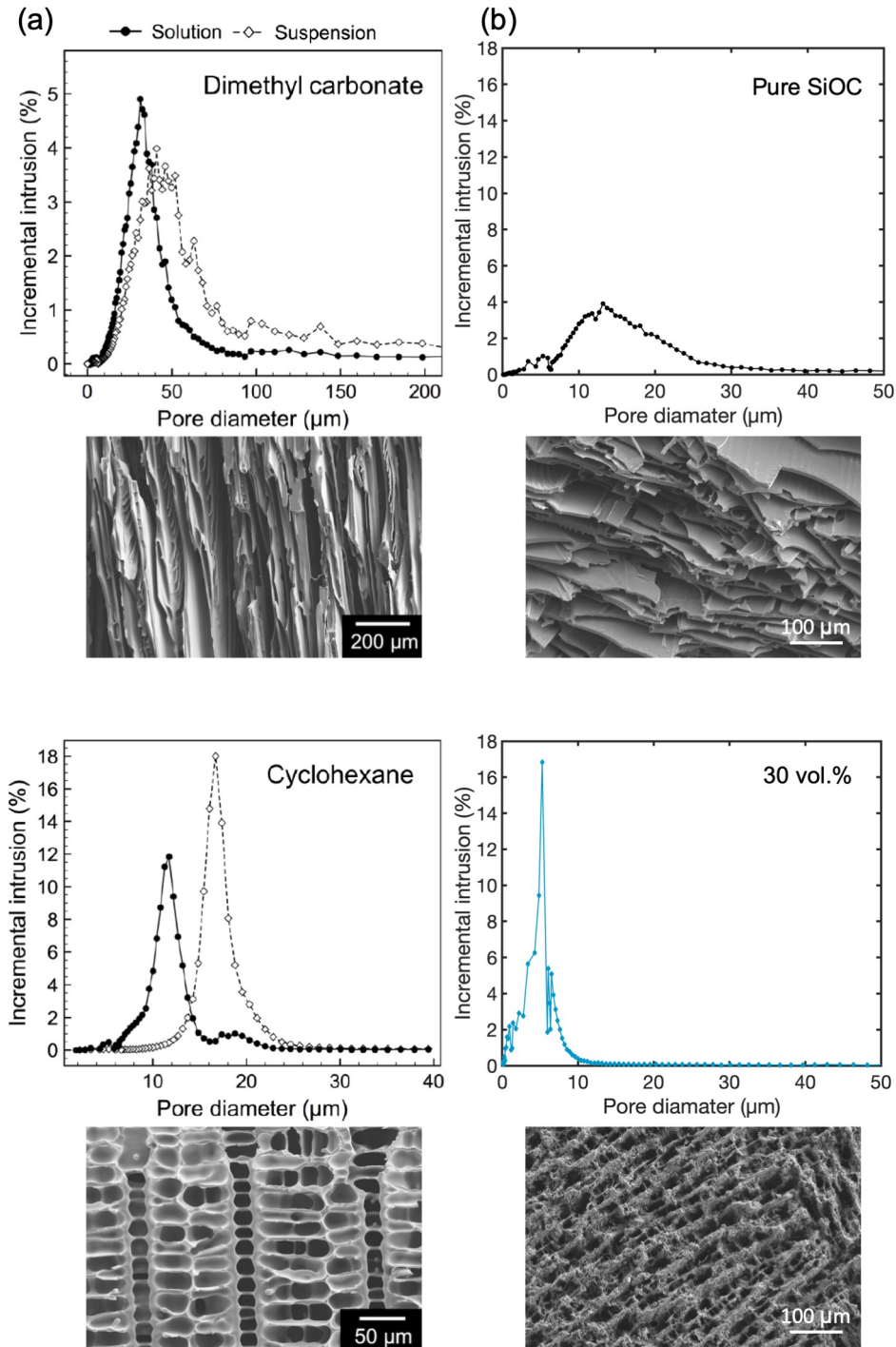


Figure 3.5: Pore size distributions from MIP and the corresponding SEM images of freeze-cast pore structures of (a) SiOC using DMC and cyclohexane, adapted from [126], and (b) SiOC and 30 vol.% SiC whisker composites using DMC in this work.

Naviroj [126] has shown that lamellar structures naturally have a wider pore size

distribution compared to dendritic structures. The pore size of lamellar pores in his work ranges from 10 to 100 μm and the maximum pore volume (intrusion volume) remains less than 5%, while the peak of the dendritic pore size is in the range of 20 μm and the maximum pore volume can be as high as 12% (Fig. 3.5(a)). With the added whiskers as interlamellar bridges, the pore size distribution is narrowed and the maximum pore volume increases from 4% to 17% for 30 vol.% SiC whisker composites, as demonstrated in Fig. 3.5(b).

3.3.1.2 Mechanical Properties and Permeability

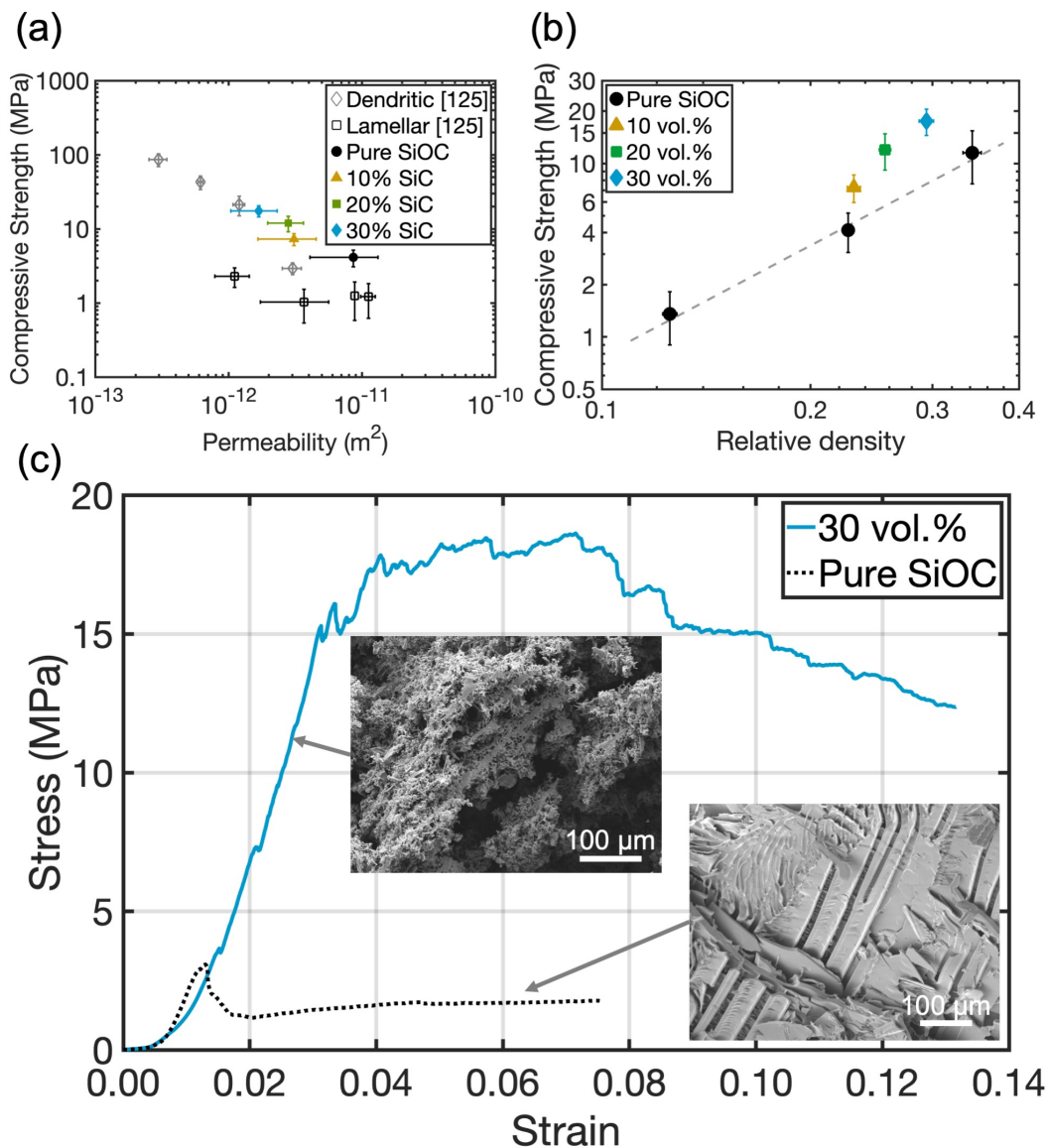


Figure 3.6: Compressive strength as a function of (a) permeability and (b) relative density. Error bars represent ± 1 standard deviation. (c) Representative stress-strain curves for freeze-cast pure SiOC (dotted black line) and for a freeze-cast 30 vol.% SiC composite (blue line). The insets show SEM images of fracture surfaces of pure SiOC ceramics and 30 vol.% SiC composites with arrows pointing toward the corresponding stress-strain curves.

Incorporation of SiC whiskers decreases permeability and increases strength (Fig. 3.6(a)). Although addition of 10 vol.% whiskers might have a stronger effect on permeability (decreases by a factor of 3, albeit with a large uncertainty) than

on strength (doubles), the overall trend is approximately an inverse relationship (approximate slope of -1 on log-log plot). Compared to prior literature on pure SiOC lamellae [125], the range of permeability overlaps with the present study, while 30 vol.% whisker reinforcements achieve strength in the present lamellar structures that is an order of magnitude greater than previously reported.

High-aspect ratio particles serve as reinforcements while maintaining the advantageous high permeability ($> 10^{-12} \text{ m}^2$) of lamellar structures. However, an increase in compressive strength could simply result from higher solids loading [156]. If this were the case, the same reinforcement could be more easily achieved by increasing the MK polymer concentration. Therefore, it is crucial to compare the composites with pure SiOC of similar porosity to shed light on its reinforcement mechanism.

It is well-known that compressive strength increases with increasing relative density following a power-law relation for porous materials [65]:

$$\frac{\alpha}{\alpha_0} = C \left(\frac{\rho}{\rho_0} \right)^n \quad (3.2)$$

where C and n are constants for a given material and pore structure (independent of the porosity of the material), α and α_0 are the strength of the porous and the dense structure, respectively, and ρ and ρ_0 are the bulk density and the true density of the structure, respectively. Pure freeze-cast SiOC ceramics with various porosities, and therefore densities, were used to establish the power-law relation and it was found that compressive strength scales with the square of relative density ($n \approx 2$), indicated by the grey dashed line (Fig. 3.6(b)).

Although strengthening with added SiC whiskers was expected, this strengthening was much higher than predicted from an increase in density alone (indicated by dotted baseline established from freeze-cast pure SiOCs with various density). The compressive strength is shown in Fig. 3.6(b) to increase by 76%, 191%, and 325% with 10, 20, and 30 vol.% SiC whiskers, respectively. We hypothesize the strengthening largely comes from two different effects of adding SiC whiskers. The fraction of SiC whiskers in the freeze-cast walls creates fiber-reinforced composites walls, likely stiffer and tougher than the pure SiOC pore walls. The other effect stems from a change in fracture mode arising from SiC whiskers spanning lamellar pores.

As previously mentioned, lamellar structures often fail in shear fracture due to insufficient interlamellar connections [111]. This is evidenced by the signature porous ceramic stress-strain curve. The stress increases linearly to a peak value at

which point the lamellar walls start to slip over one another, resulting in a large drop in stress. This is followed by a gradual increase in stress due to the densification of the fractured pore structure (dotted black line in Fig. 3.6(c)). In contrast, for SiC whisker composites, interlamellar bridges formed by the added whiskers prevent shear failure. The stress-strain curve of the 30 vol.% whisker composite (blue curve in Fig. 3.6(c)) is interpreted as follows: a series of micro-fracture events begin at about 3% strain and progress cell-by-cell, leading to a stress maximum at approximately 30% strain followed by softening. The change in fracture mode with whisker additions can also be observed from the fracture surfaces (insets in Fig. 3.6(c) with arrows pointing toward the corresponding the stress-strain curves). In pure SiOC ceramics, the fracture surfaces are clean cleavage between lamellar walls, leaving behind intact walls. In contrast, in SiC-reinforced composites, the fracture surface propagates through lamellar walls as the whisker bridges act as interlamellar connections. These two effects from the addition of SiC whiskers (reinforced pore walls and prevention of shear fracture) increase the strength of freeze-cast structures, demonstrating the reinforcing mechanism of high-aspect ratio particles in freeze-cast systems. The stress-strain curves of all 30 vol.% SiC composites and pure SiOC tested are included in Appendix A to demonstrate the consistency in the results.

3.3.2 Two-dimensional *in-situ* Solidification Experiments

3.3.2.1 Theory

To observe the solidification process *in situ*, low particle concentrations are necessary to prevent obstructions in the freezing front views. However, reducing the solids loading dramatically can change the solidification parameters (e.g., rheological properties, heat capacity, and thermal conductivity) and, consequently, change the shape, size and spacings of the freezing dendrites relative to actual freeze-casting conditions [112]. Therefore, using polysiloxane polymer as the major fraction of the "solids loading" has an advantage over using SiC whiskers. Polysiloxane is transparent upon dissolution, and therefore, provides a clear avenue to observe solidification without interference. The SiC whisker concentration is reduced to 0.2 vol.% so that dendrite-whisker interactions can be observed. Since polysiloxane polymer is the major component of the solids loading, reducing SiC whisker concentration does not drastically change the total solids loading. This allows us to observe particle engulfment by freezing dendrites similar to those in conventional freeze-casting systems.

We present a model of an actual freeze-casting system. A schematic of the particle engulfment process is shown in Fig. 3.7(a). The whisker experiences two major forces as the dimethyl carbonate crystals solidify and grow in the direction of the temperature gradient—a drag force and a repulsive force. The single whisker and growing dendrite intersect at an angle θ , and an offset distance b . Theoretically, the model can be extended to 3D.

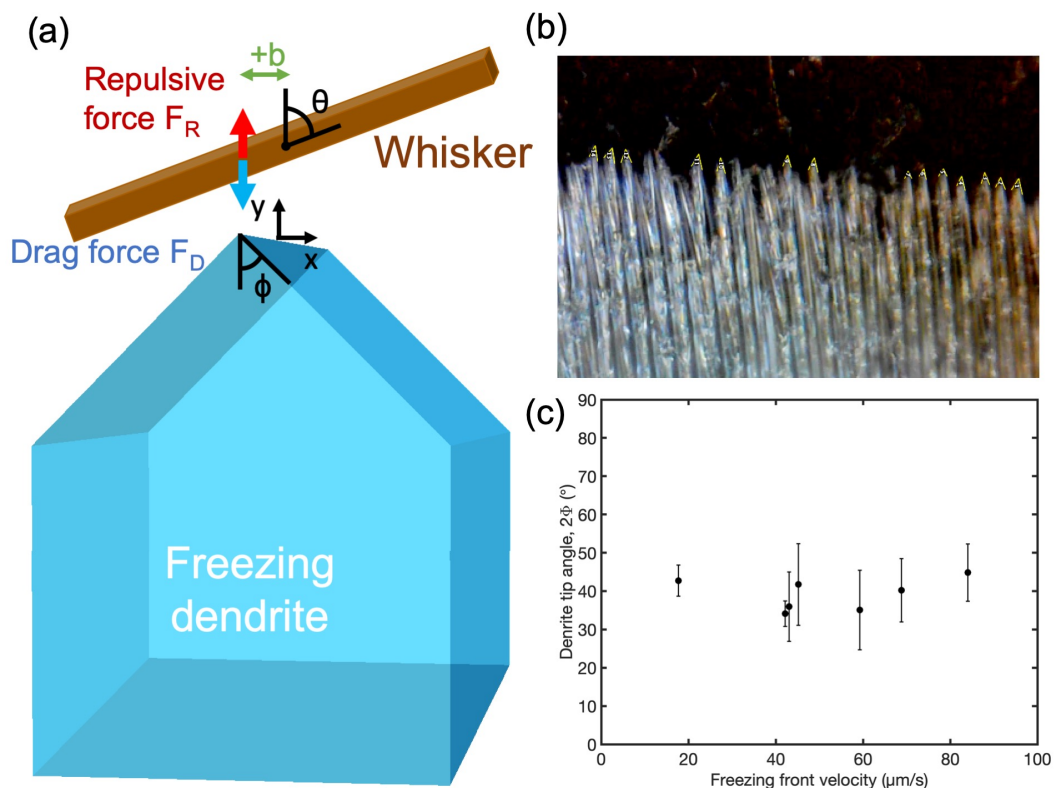


Figure 3.7: (a) A schematic of the acting forces during the engulfment process. (b) An example of a dendrite tip angle measurement. (c) Dendrite tip angle as a function of freezing front velocity. Error bars represent ± 1 standard deviation.

3.3.2.2 Engulfment-related Forces and Critical Freezing Front Velocity

The drag force on a spherical or cylindrical particle with a planar interface is well-known [26, 27, 62, 101]:

$$F_d = -6\pi\eta V_{ff} \left(\frac{R_p^2}{h} \right) \text{ for a sphere, and} \quad (3.3)$$

$$F_d = -3\sqrt{2}\pi\eta V_{ff} \left(\frac{R_p}{h} \right)^{\frac{3}{2}} L \text{ for a cylinder} \quad (3.4)$$

where η is the dynamic viscosity of the solvent, R_P is the particle radius, h is the distance between the particle and the freezing front, V_{ff} is the freezing front velocity, and L is the length of the cylinder. To account for the non-planar shape of the interface, some researchers use the relative thermal conductivity between the particle, K_P , and the solvent, K_L , to calculate the particle-induced curvature of an otherwise planar growth front, R_I [161, 168]

$$F_d = -6\pi\eta V_{ff} \left(\frac{R_P^2}{h} \right) \left(\frac{R_I}{R_I - R_P} \right) = -6\pi\eta V_{ff} \left(\frac{R_P^2}{h} \right) \left(\frac{K_P}{K_L} \right) \quad (3.5)$$

However, in the dendritic regime, the interface shape is largely determined by the freezing front velocity, thermal gradient, and solute concentration in the solution [14, 17, 33, 98]. The theoretical determination of the freezing front (the shape, size and spacings of the freezing dendrites) is not the focus of this study. Instead, we neglect curvature and use the measured angle of the faceted freezing dendrite tips from the 2D solidification experiment for the model: the angles are found to be 39° (Fig. 3.7(b)), largely invariant with respect to the freezing velocity (Fig. 3.7(c)).

When the ice front advances, fluid flows continuously into the gap to maintain the liquid film. This flow creates a pressure difference in the gap and the pressure gives rise to the drag force, which is calculated from the Navier-Stokes equation. In 2D *in-situ* solidification, the flow is restrained to the directions parallel to the glass slides that confine the SiC whisker suspension. We assume that the volume difference between the liquid and solid DMC is negligible. The flow becomes unidirectional and the Navier-Stokes equation can be solved analytically for boundary conditions where the fluid velocity is zero at the solid surfaces, and by applying conservation of mass.

$$\frac{\partial^2 v_x}{\partial y^2} = \frac{1}{\eta} \frac{\partial P}{\partial x}$$

where v_x is the fluid velocity in the x-direction, and η and P are the viscosity and the pressure of the fluid, respectively.

The boundary conditions are as follows:

$$v_x(y = 0) = 0$$

$$v_x(y = h) = 0,$$

and the conservation of mass:

$$\int_0^h v_x(y) \times d \, dy = L \times d \times V_{ff}$$

By solving the Navier-Stokes equation, we arrive at the following expression for the drag force:

$$F_d = -6\eta L^3 dV_{ff} \left\{ \frac{(1 - 2b \csc \theta)^2}{h[L(a - \cot \theta) + 2(h - abL + bL \cot \theta)]^2} + \frac{(2b + \sin \theta)^2}{h[L(a \sin \theta + \cos \theta) + 2(h + abL + bL \cot \theta)]^2} \right\} \quad (3.6)$$

where d is the width and height of the whisker and the dendritic tip slope, a , is equal to $\cot \theta$.

When a planar freezing front ($a = 0$, $b = 0$) is assumed and the whisker is parallel to the freezing front ($\theta = \pi/2$), the drag force reduces to $\frac{3L^3 d\eta V_{ff}}{h_0^3}$. The force scales as $(L/h)^3$, similar to two flat surfaces moving toward each other (h^{-3}), instead of a circular cylinder moving toward a flat surface. In the present case, we adopt a square cylinder morphology instead of the circular cylinders used in previous models because SiC whiskers used in this study are faceted as shown in Fig. 3.1.

The dynamic viscosity, η , of 20 wt.% polysiloxane polymer solution was determined to be 21.79 mPa·s. Other parameters used in the calculation of the drag force include the minimal distance, h , between the freezing front and the whisker, where $h = 2 \times 10^{-10}$ m [19, 89, 161] and atomic distance $a_0 = 2 \times 10^{-10}$ m [19, 89, 151, 161, 175].

The exact origin of the repulsive force is still in dispute. Approaches using the surface energy differences [52, 138] or the disjoining force [66, 143] as the origin have been discussed. We argue that the energy difference before and after the engulfment cannot be "experienced" by the particles before the engulfment and therefore, cannot provide the repulsive forces. (The surface energy approach is discussed in Appendix B for comparison.) Here, we proposed an alternative origin of the repulsive force, the osmotic pressure, Π , from the concentration gradient of the polysiloxane polymers in front of the freezing front.

The solubility of the polymers is higher in the liquid than in the solid. Therefore, as the freezing front advances, rejected solutes may pile up, creating a concentration gradient in front of the freezing front. The concentration difference and, therefore, the osmotic pressure difference across the whisker width produce a repulsive force pushing the whisker forward as shown in Fig. 3.8.

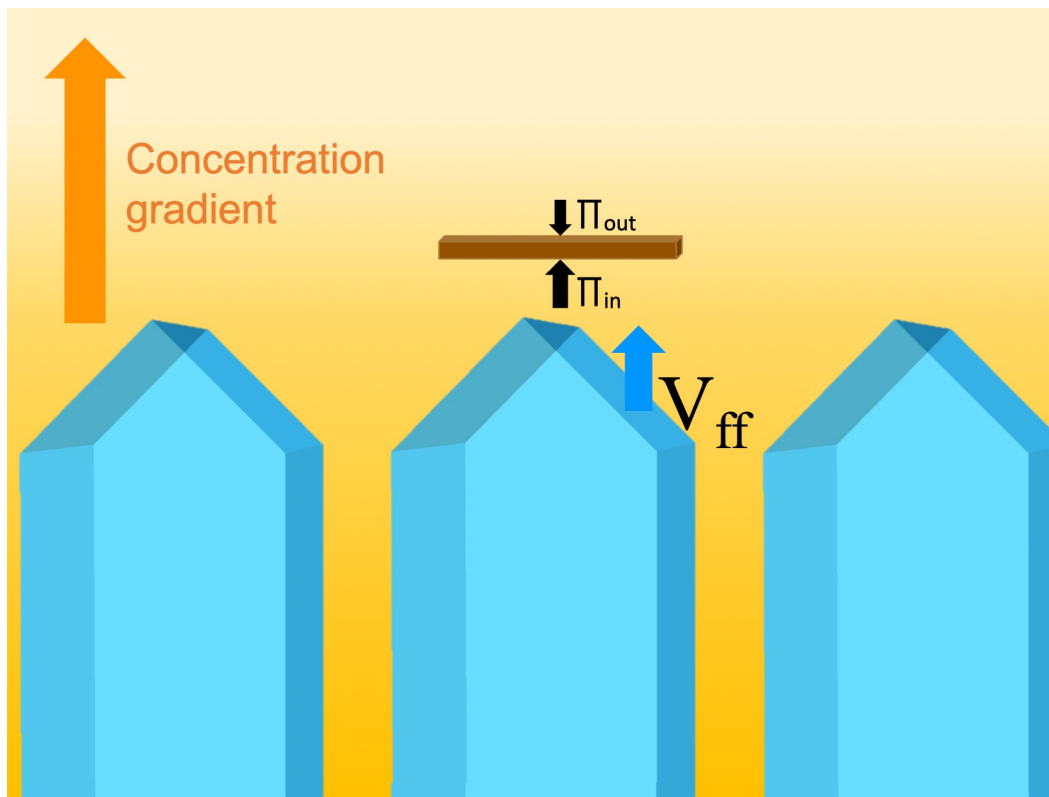


Figure 3.8: A schematic of solute pileup during the freezing process and the resulting osmotic pressure difference.

The difference in the osmotic pressure was estimated to be ~ 3000 Pa following

$$\Delta\Pi = \Delta C \times RT \quad (3.7)$$

where ΔC is difference of solute molar concentration across the whisker, R is the ideal gas constant, and T is the temperature in Kelvin.

Polymers of similar molecular weights to the MK polymer ($M_W = 9400$ g/mol), such as poly(vinyl alcohol) ($M_W = 9000$ g/mol) and poly(ethylene glycol) ($M_W = 8000$ g/mol), are shown to have a solute pileup of 40 to 80 μm and an increase in concentration of 1.5 to 9 times in aqueous solutions with freezing front velocities of 2 to 10 $\mu\text{m/s}$ [24]. The highest concentration of solute pileup decreases with increasing freezing front velocity. The length scale varies as diffusivity over velocity, and diffusivity scales inversely with viscosity. Given that the ratio of viscosities of DMC to water is 0.9, the field of solute pileup and maximum increase of concentration are estimated to be ~ 40 μm and 2 times for freezing front velocities used in this study (~ 20 to 70 $\mu\text{m/s}$), respectively.

The repulsive force was calculated following

$$F_r = \Delta\Pi \times d \times L_{effective} \quad (3.8)$$

where $L_{effective}$ is the length of whisker that is in close contact with the dendrite tip, and is estimated to be about $40 \mu\text{m}$. With a dendritic tip slope of 2.83, the far end of the whisker is far away from the dendrite, and unlikely to experience any force.

From freezing videos, we can see whiskers interact with a translucent area around the opaque whisker. If the translucent area is due to the change in reflective index from the solute pileup, the origin of the repulsive force is likely osmotic pressure as the distance is a few microns away from the dendrite tip. In contrast, if the translucent area is the tapered edge of the dendrite, the origin of the repulsive force may be the disjoining force, since the distance is in submicron or smaller. A higher-resolution microscope would be required to determine the origin of the repulsive force.

Critical freezing front velocities were calculated from $F_d = F_r$. Engulfment occurs when the freezing front velocity exceeds the critical freezing front velocity for a given whisker length. To compare the model with experiments, critical freezing front velocities were determined from solidification videos by measuring the length of the whiskers that are pushed away or engulfed for a given freezing front velocity. Various freezing fronts were achieved by recording the solidification process from different distances to the cooling plate. The measurement error of the freezing front velocities is estimated to be $\pm 5 \mu\text{m/s}$. Only whiskers that are roughly perpendicular to the freezing dendrites and centered were counted. Fig. 3.9 shows reasonable agreement between experimental data and the theoretical critical freezing front velocity (marked by a grey line) for conditions of $b = 0$ (whisker bisected by the freezing front) and $\theta = \pi/2$ (whisker perpendicular to freezing dendrites) in calculating the drag force. Asthana et al. [6] reviewed several engulfment models and found that the theoretical predictions and experimental results models often differ by several orders of magnitude. This makes the agreement between the theoretical and experiment results here especially compelling. This agreement indicates that the model is a sufficiently accurate description of the experiment.

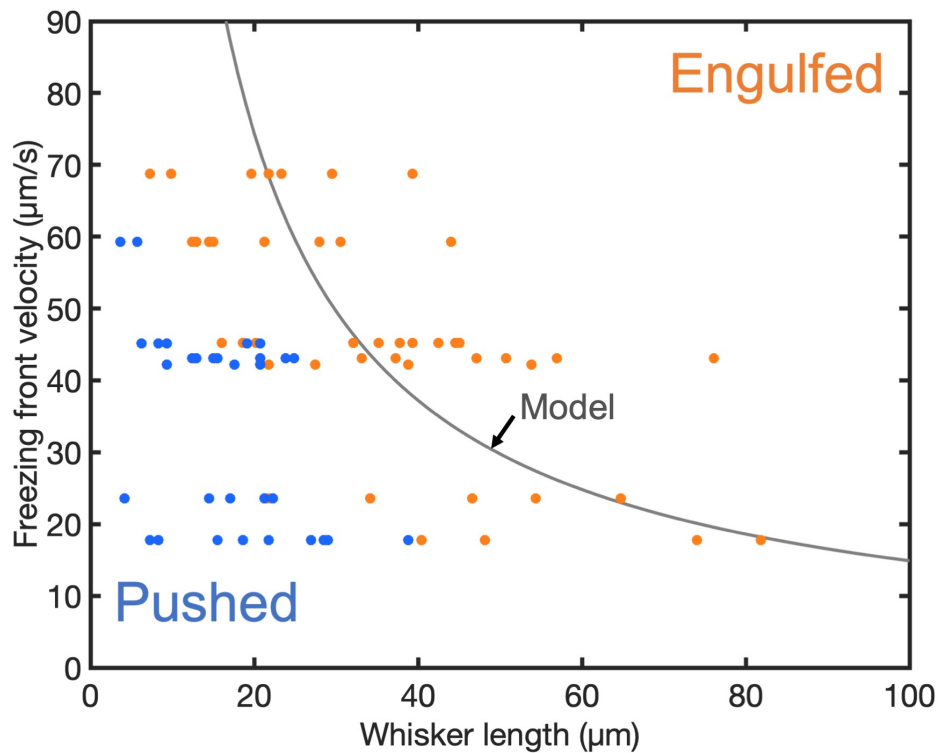


Figure 3.9: Freezing front velocity versus whisker length with experimental data; blue circles represent pushed whiskers; orange circles represent engulfed whiskers. The theoretical critical freezing front velocity (grey line) was calculated with engulfment model described in Section 3.3.2.2.

3.3.2.3 Torque and Whisker Rotation

The fluid motion that gives rise to the drag force also creates torque on the whisker. The intersecting angle θ , and offset distance b , determine the orientation and the magnitude of the torque. The torque is integrated from the pressure difference inside the gap between the whisker and the dendrite. The rotating whisker also experiences a frictional force from the viscous liquid around it. This frictional force always acts against the rotating movement and slows down or prevents rotation. A detailed calculation of torque can be found in Appendix C.

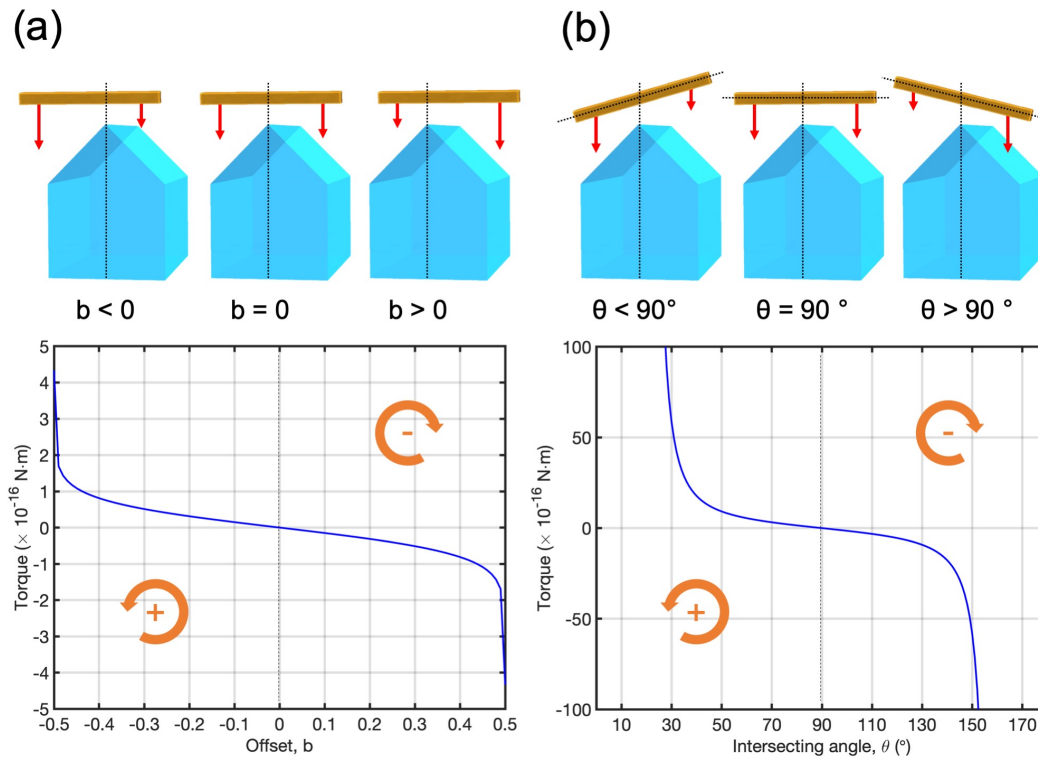


Figure 3.10: The torque acting on whiskers as a function of (a) offset distance, and (b) intersecting angle.

From the model, we find that intersecting angles and offset distances give rise to torque and the subsequent rotation. The rotation arises from the pressure difference caused by the fluid motion that results in the drag force. Only when a whisker is centered ($\theta = \pi/2$) and bisected ($b = 0$) by the dendrite is the torque zero and the whisker does not rotate. If the whisker is not bisected, the whisker rotates toward the longer side of the whisker (3.10(a)), as is expected.

Fig. 3.10(b) shows that whiskers that are not perpendicular to the freezing front ($\theta \neq \pi/2$) experience torque and rotate out of the way of the freezing dendrites, leaving behind whiskers that are mostly parallel or perpendicular to the freezing front and the lamellar walls. These results were observed in the solidification videos with slower freezing front velocities (shown in Appendix D) from the 2D solidification experiments and could explain the aligning effect observed in freeze casting with Al platelets, SiC whiskers, and CNTs [57, 63, 70]. With faster freezing front velocities, long whiskers rarely rotate before being engulfed by the freezing front. This rotation is not limited to large particles that will be engulfed but any particle that encounters

freezing dendrites. The particle rotating to the inter-dendritic space will be further aligned by the compacting motion of thickening dendrites [20]. Interestingly, we also observed fluid backflow, possibly from the density difference between solidified and liquid solvent, which contributes to whiskers moving into interdendritic space.

In the case of spherical particles, particles are either fully engulfed or pushed away. However, partial engulfment—where only a portion of particles is engulfed while the rest are pushed away—is common in freeze casting of high-aspect ratio particles. These two parameters (θ and b), introduced due to the geometry of high-aspect ratio particle and non-planar freezing front, can explain partial engulfment in the case of high-aspect ratio particles. For example, the high-aspect ratio particles can rotate out of the way even if the freezing velocity is above the critical freezing front velocity. The percentage of the engulfed whiskers is determined by the solidification conditions and will be further discussed in the next section.

3.3.2.4 Freezing Simulations and Bridge density

The 2D solidification simulation based on the proposed model can reveal the effect of intersecting angles and offset distances on the engulfment of SiC whiskers. The lamellar spacing and the freezing front velocity were determined experimentally (Appendix E) for 10, 20, 30 vol.% SiC whisker suspensions. The visualization of the simulation is shown in Fig. 3.11(a). Blue lines represent freezing dendrites. Whiskers are randomly distributed and randomly oriented at the start of the simulation (simulation details: whisker concentration, width (d), and length (L) are 2 vol.%, $2\ \mu\text{m}$, and $30\ \mu\text{m}$ respectively. Freezing front velocity is $45\ \mu\text{m/s}$). In this example (Fig. 3.11(a)), some whiskers never interacted with the freezing front, while some were pushed aside/engulfed by the freezing front. This simulation shows both alignment and partial engulfment of whiskers as observed in 2D *in situ* solidification videos and 3D freeze-casting systems. With the simulation, the engulfed whisker fraction is found to vary even for the same freezing conditions, i.e. same freezing front velocity and lamellar spacing (Fig. 3.11(b)). This variance in the engulfed whisker ratio was caused by the starting angles and positions of whiskers.

Previous particle engulfment models of planar freezing front and spherical particles only considered the particle size and freezing front velocity. Here, the variance shows that in addition to the particle size and freezing front velocity, the intersecting angle and offset distance also play a major role in whether a high-aspect ratio particle is engulfed.

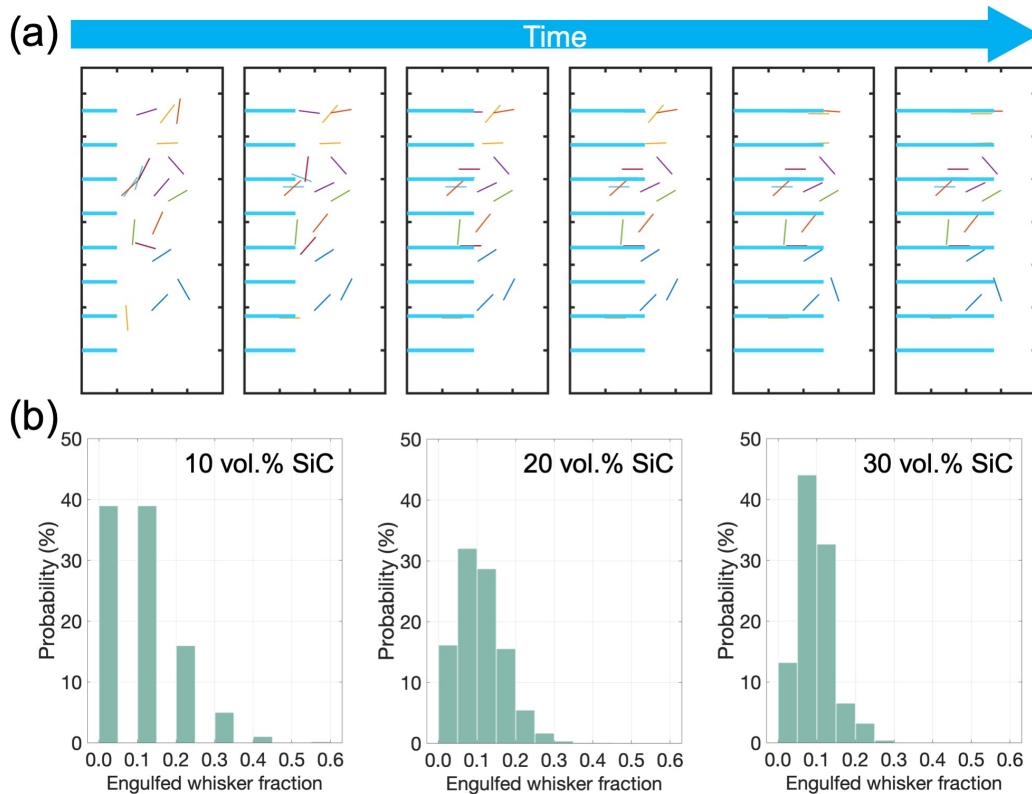


Figure 3.11: (a) Visualization of simulation (SiC concentration = 2 vol.%, $d = 2 \mu\text{m}$, $L = 30 \mu\text{m}$, $V_{ff} = 45 \mu\text{m/s}$). Blue lines represent freezing dendrites. Whiskers are randomly distributed and orientated. (b) Probability of engulfment fraction from the simulation for 10, 20, and 30 vol. % SiC solidification.

Experimental values of engulfed whisker percentages were calculated for each SiC concentration from the bridge density of freeze-cast samples. As previously mentioned in Section 3.2.2.4, each simulated engulfed whisker fraction is averaged from 2000 repeated simulations for each solidification condition to gain an overall sense of engulfment due to the variance in simulation results shown in Fig. 3.11(b). Both experimental and simulated engulfed whisker fractions are reported in Table 3.3 and are of the same order of magnitude. We hypothesize that the force of gravity, present only in freeze-cast experiments, could explain some of the difference between the simulated and the experimental result. Furthermore, the simulation is simplified and does not include the particle-particle interactions and the interaction between a single particle with multiple dendrites. With particle-particle interactions and the interaction of single particles with multiple dendrites, we expect to see a higher fraction of engulfed whiskers due to the interlocking of SiC whiskers in the former case and a higher probability of having at least one dendrite meet engulfment criteria

with a whisker in the latter.

Table 3.3: Comparison of the engulfed whisker ratio between the freeze-cast samples and freezing simulation

SiC whisker/all solid (vol.%)	Experimental engulfed fraction (%)	Simulated engulfed fraction (%)
10.00	14.13 ± 2.48	10.07
20.00	12.68 ± 2.32	9.39
30.00	15.47 ± 4.18	9.54

The model further predicts a higher fraction of engulfment with higher freezing front velocities (Fig. 3.12(a)) and longer whiskers (Fig. 3.12(b)). The higher engulfment fraction is caused by a higher probability of engulfment for individual particles. Both predictions are consistent with the results from previous spherical particle engulfment models.

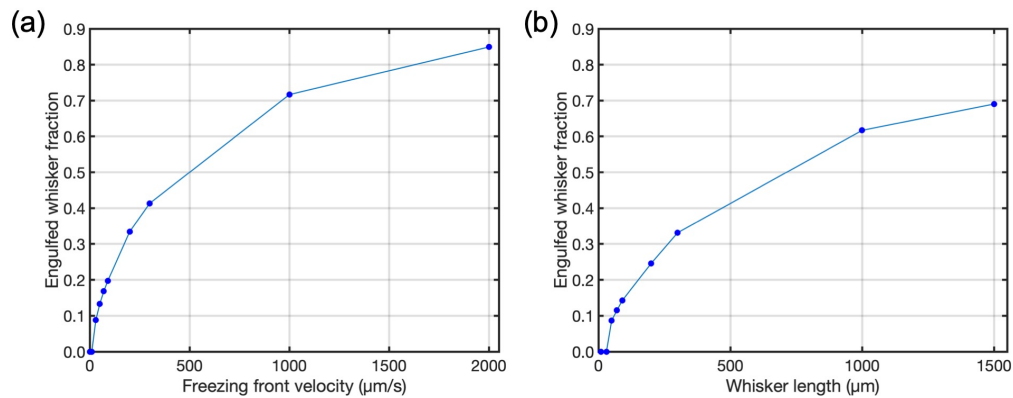


Figure 3.12: Averaged simulated engulfed whisker fraction as a function of (a) Freezing front velocity and (b) whisker length.

These results show that the proposed model and the subsequent simulation are able to reproduce results that are consistent with previous engulfment models, i.e. those that include higher probabilities of engulfment with higher freezing front velocities and large particles. Furthermore, the proposed model and the simulation can produce results unachievable with the previous models, specifically for partial engulfment and alignment effects common in freeze casting high-aspect ratio particles. A deeper understanding of particle engulfment of high-aspect ratio particles gained from this model will allow us to better design the processing of materials in solidification and freeze casting.

3.4 Conclusions

High-permeability lamellar structures often fail in shear fracture at low stress, limiting their wider adoption as filter materials. To achieve better pore morphologies and microstructures, we introduced interlamellar bridges by freeze casting high-aspect ratio SiC whiskers with polysiloxane preceramic polymer. The compressive strength shows a 3-fold increase with 30 vol.% whiskers while maintaining a high permeability in the range of 10^{-12} m². Two types of interlamellar bridges were identified: one formed from particles trapped between secondary dendrite arms and the other from particle engulfment of high-aspect ratio particles (SiC whiskers). The density of interlamellar bridges increases linearly with the concentration of SiC whiskers.

To remedy the deficiency of current engulfment theories, we proposed a new model to account for two new variables, the intersecting angle between a pair of the interacting whisker and freezing dendrite and the offset between the center of a whisker and that of the nearest dendrite, introduced due to the geometry of high-aspect ratio particles and lamellar/dendritic freezing fronts.

The critical freezing front velocity was calculated from the model and the result was in reasonable agreement with the experimental values. Moreover, a simulation based on the proposed model successfully reproduced the whisker rotation, the sequential alignment, and the partial engulfment of high-aspect ratio particles observed in the experiments, while the engulfed whisker fractions from the simulation and those from the experiment were in close range. In addition, the simulation showed higher probabilities of engulfment with higher freezing front velocities and longer whiskers, consistent with the previous engulfment models.

This chapter explored reinforced pore structures with engulfed whiskers with both theory and experiment, providing an in-depth understanding of the freezing process of high-aspect ratio particles, the resultant microstructures, the mechanical properties, and the fracture behavior of porous composites. This research can further improve the prediction of both structure and resultant properties and result in more accurate designs for porous composites with high-aspect ratio particles.

CARBON NANOTUBE-REINFORCED COMPOSITES

Material in this chapter is reproduced in part from "Permeable carbon nanotube-reinforced silicon oxycarbide via freeze casting with enhanced mechanical stability", C.T. Kuo, K.T. Faber; *Journal of the European Ceramic Society*, 40 (2020) 2470–2479. The work was done in collaboration with Katherine T. Faber. T. Kuo fabricated and characterized CNT composites, and wrote the manuscript. K. Faber supervised this work.

4.1 Introduction

Chapter 3 demonstrated that SiC whiskers as reinforcing fillers increase the compressive strength of lamellar structures dramatically at a small expense in permeability by significantly changing the lamellar structure. Here we explore the possibility of retaining the original freeze-cast pore structures with alternative reinforcement methods. To accomplish this, the reinforcing fillers need to fulfill the following requirements. First, the reinforcement must change the strength significantly with small quantities so that there is little risk of altering the freezing dynamics, and by consequence, the structure. The second requirement is for reinforcements to be small enough, and of low enough density relative to the solution, to be pushed by the freezing front and embedded in the walls without protrusion. Lastly, the reinforcements have to be dispersible in the solution/suspension to achieve uniform distribution in the final freeze-cast structures.

In light of these constraints, we chose multi-walled carbon nanotubes (MWCNTs) to be the reinforcing fillers. MWCNTs can have strengths as high as 63 GPa [194] and are known to increase the strength of a matrix as much as five times with as little as 1 wt.% CNT [84]. It has been shown previously that the mechanical properties (e.g. Young's modulus, compressive strength, and toughness) are very sensitive to the quality of dispersion of CNTs in the matrix; the better the dispersion, the stiffer, stronger, and tougher the composite [9]. This gives MWCNTs an advantage over single-walled carbon nanotubes (SWCNTs), since MWCNTs, unlike SWCNTs, are less likely to form bundles, making uniform dispersion in the matrix more feasible [34].

CNTs as reinforcements in polymeric matrices have been well studied [167] and some research has explored ceramic matrices [3, 11, 163]. However, in the latter, the high pressures and temperatures required to densify ceramic powders by hot pressing might deteriorate CNTs, which limits their reinforcing effect [197]. To avoid the damage caused by high temperature and pressure during hot pressing, several groups have previously dispersed CNTs in preceramic polymers and pyrolyzed the suspensions to produce CNT-ceramic composites [74, 85, 152, 199]. Using this approach, CNTs are largely preserved after pyrolysis, resulting in a noticeable reinforcement effect. Gutierrez et al. have reported a series of studies on freeze casting of CNTs [1, 70], where the CNTs were used for their low electrical percolation limit, high conductivity, and excellent biocompatibility, but not as reinforcements.

The work described here is the first where CNTs are used as the reinforcing fillers in a freeze-casting system to create porous CNT-ceramic composites and composite design in such systems is addressed. In this chapter, we will demonstrate both the potential and challenges of incorporating CNT reinforcements in freeze-cast systems. The processing and dispersion methods are described, as well as the effect of reinforcements on the microstructure, electrical conductivity, permeability, compressive strength, and toughness.

4.2 Experimental Methods

4.2.1 Materials and Processing

A commercially available polysiloxane preceramic polymer (Silres[®] MK Powder, Wacker Chemie, CH₃-SiO_{1.5}, Munich, Germany) was dissolved in organic solvents and freeze cast to produce porous silicon oxycarbide (SiOC). MWCNTs (purity: >90 wt.% carbon nanotubes, outside diameter: 8-15 nm, inside diameter: 3-6 nm, length: 30-50 μm, density: 2.1 g/cm³, US Research Nanomaterials, Inc., TX, USA) were introduced to reinforce the porous SiOC matrix. After assessing several combinations of dispersants and solvents, dimethyl carbonate (DMC, m.p.= 2-4°C density: 1.073 g/cm³, Sigma-Aldrich, MO, USA) and Hypermer KD1 (Croda, NJ, USA) were determined to be the optimal solvent and dispersant, respectively, for dispersing carbon nanotubes. Hypermer KD1 is a cationic dispersant, which has been proven effective in dispersing graphene-based nanomaterials [115].

To prepare porous SiOC, MK was first dissolved in DMC. A cross-linking agent (N-(2-Aminoethyl)-3-aminopropyltrimethoxysilane, Geniosil GF 91, Wacker Chemie, Munich, Germany) was added into the MK-DMC solution and stirred for 3 min

before freezing. To prepare CNT-SiOC composites, KD1 was first dissolved in DMC. MWCNTs were then added to the solution and sonicated for 60 min in Branson 3800 Ultrasonic Cleaner (Branson, OH, USA). After sonication, MK was added into the CNT suspension and sonicated for another 60 min. In most composites prepared via solution processing, sonication is one of the most effective ways to break up CNT agglomerates and achieve uniform dispersion in the composites [34]. Geniosil GF 91 was added into the MK-CNT-DMC suspension and stirred for 3 min before freezing.

The suspension or the solution was then poured into a glass mold with an inner diameter of 24 mm, and frozen at a cooling rate of 3°C/min from 10°C to -30°C. After the completion of solidification, the body was dried in a lyophilizer (Virtis Wizard 2.0, SP Scientific, PA, USA) until all solvent was removed. The green sample was then cured at 150°C for 24 h to increase ceramic yield, and pyrolyzed at 1100°C for 4 h with a 2°C/min heating and cooling ramp rate under argon to obtain a CNT-amorphous silicon oxycarbide (SiOC) composite. The pyrolyzed samples were sectioned for SEM micrographs and imaged at their mid-section.

Eight concentrations of CNTs and the respective KD1 concentrations, shown in Table 4.1, were chosen to determine the conductivities of porous CNT-SiOC composites. Four concentrations of CNTs in the pyrolyzed solid, 0.0, 1.3, 4.3, and 8.2 wt.%, were used for all other measurements. To make comparisons easier with other studies, units of mg/ml are used with CNT-preceramic polymer suspensions while wt.% is used with pyrolyzed freeze-cast composites or dense disks for toughness measurements. The units were converted assuming a total decomposition of KD1 and a ceramic yield of 75% for MK [126]. Pyrolyzed freeze-cast CNT-SiOC composites with 1.3, 4.3, and 8.2 wt.% CNTs were made from suspensions with 3, 10, and 20 mg/ml CNTs. The volume percent (vol.%) MWCNTs in the solid scales with the weight percent (wt.%) as follows: 1.5, 4.7, and 9.0 vol.% correspond to 1.3, 4.3, and 8.2 wt.%.

Table 4.1: Compositions of suspensions and pyrolyzed samples.

CNT/DMC (mg/ml)	KD1 (g)	CNT (g)	DMC (g)	MK (g)	CNT concentration of pyrolyzed solid (wt.%)
0	0.00	0.00	10.73	3.00	0.00
0.1	0.02	0.001	10.73	3.00	0.04
0.25	0.02	0.0025	10.73	3.00	0.11
0.5	0.02	0.005	10.73	3.00	0.22
1	0.02	0.01	10.73	3.00	0.44
3	0.06	0.03	10.73	3.00	1.32
10	0.10	0.1	10.73	3.00	4.26
20	0.20	0.2	10.73	3.00	8.16

4.2.2 X-ray Diffraction

Phase compositions of as-received CNTs and samples with 0, 4.26 wt.% and 8.16 wt.% CNTs were evaluated using X-ray diffraction (XRD). Scans were conducted with Cu-K α radiation from 10° to 60° with a scan speed of 0.057°/s (PANalytical X'Pert Pro). Background subtraction and peak fitting were performed to identify phases.

4.2.3 Electrical Conductivity

Resistance measurements were performed at room temperature with a Keithley 614 Electrometer for five lower CNT concentrations (≤ 0.44 wt.%) and a Fluke 115 True-rms Multimeter for three higher CNT concentrations (≥ 1.32 wt.%). Because freeze-cast and pyrolyzed samples have an uneven top surface due to the meniscus formed during freezing, samples were cut at 2 mm from the top surface to produce two parallel surfaces at the ends. The two ends were coated with carbon paste and sandwiched between two copper plates for resistance measurements. The conductivity was calculated without any adjustment for porosity.

$$\sigma = \rho^{-1} = \frac{L}{RA} \quad (4.1)$$

where σ is the conductivity, R is the measured resistance, ρ is the resistivity, and L and A are the length and the contact area of the sample.

4.2.4 Permeability

The permeability of the porous solids was assessed from the flow rate of water over a series of pressure drops. The permeability test setup consisted of a water tank, a pressure sensor (Omega PX409 pressure transducer, Omega Engineering, CT,

USA), a balance, and a voltage-controlled gear pump. (A schematic of the setup is shown in Fig. 4.1(a).) Pressures from 6 to 40 kPa were applied.

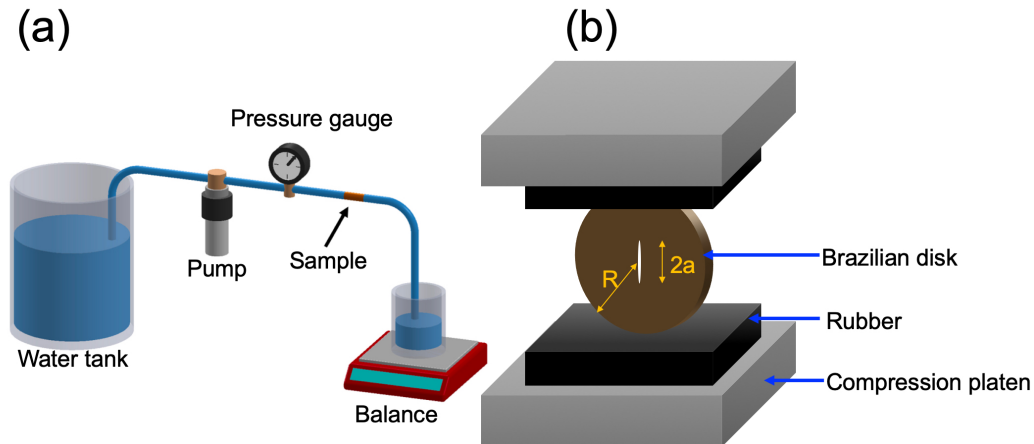


Figure 4.1: (a) Schematic of the experimental setup for permeability measurement [125]. (b) Schematic of the experimental setup for diametral compression (Brazilian disk) test. Disks were placed between compression platens with an aligner before the start of the compression testing to ensure the load was applied along the long axis of pre-crack.

Cylindrical pyrolyzed samples were core-drilled to be 13 mm in diameter, and the circumferences of the samples were enclosed by a low shrinkage mineral-filled acrylic system (VariDur 3003, Buehler, IL, USA) to prevent the leakage from the circular side of the samples. The samples were then sectioned at 4 mm and 9 mm from the sample base, and enclosed along a length of 5 mm tubing for the permeability investigation. Three separate samples were tested for each CNT concentration, and the Darcy-Forchheimer equation was used to determine the permeability constants [78].

$$\frac{\Delta P}{L} = \frac{\mu}{k_1} v + \frac{\rho}{k_2} v^2 \quad (4.2)$$

where ΔP is the pressure drop across the sample, L is the thickness of the sample, μ , ρ , v are, respectively, the dynamic viscosity, the density, and the flow velocity of water, and k_1 , k_2 are the intrinsic and inertial permeability, respectively.

4.2.5 Mechanical Properties

4.2.5.1 Compressive Strength

Uniaxial compression tests were performed on an Instron 4204 universal testing machine (Instron, MA, USA) in constant displacement mode at a displacement rate of 0.1 mm/min. To prepare samples for compressive strength measurements, cylindrical pyrolyzed samples were core-drilled to be 13 mm in diameter. The measurements for compressive strength for brittle porous materials are susceptible to a wide variance, arising from the crushing behavior due to high local contact stresses, leading to inconsistent results. A study by Mehr showed that the incorporation of a rigid interface layer could spread the applied stress more evenly and provide reliable results [117]. Therefore, VariDur 3003 was used to cap both ends of the sample, and a pair of spherical washers were placed between the sample and the compression platens to ensure the compression load was applied along the axis of the sample (A schematic of the setup can be found in [125]).

Three samples were tested for each CNT concentration. The height and diameter were recorded and used to calculate the engineering stress and strain. The compressive strength was determined by the peak of the stress-strain curve.

4.2.5.2 Fracture Toughness

The diametral compression test was performed to determine the fracture toughness of dense CNT-SiOC composites and assess the effect of CNTs on the CNT-SiOC walls. To prepare the Brazilian disks, CNTs were mixed with MK powder via rotation in a polypropylene bottle at 70 rpm for at least 12 h to obtain a uniform mixture. The powder mixture was then sifted through a mesh with 500- μ m nominal sieve opening. The powder mixture was poured into a mold with a diameter of 65 mm. Two pieces of Teflon-coated Mylar of 0.07-mm thickness and 10-mm length were taped together and inserted into the powder mixture to create the pre-crack at the center of the disk after pyrolysis.

The mold was heated at 180°C for 48 h to cure the MK. Pure MK and powder mixtures with 1.3, 4.3 wt.% CNTs produced smooth and dense solids after curing. Mixtures with 8.2 wt.% CNTs were bubble-filled and did not produce a smooth surface, and were therefore not included in the toughness testing. The cured samples were then core-drilled to be 29 mm in diameter. The circumferential side and the edges were polished with 240, 400, 600, 800, and 1200 grit silicon carbide sandpaper to obtain a uniform disk shape. The samples were pyrolyzed in an alumina

crucible filled with SiOC powders pyrolyzed from MK to achieve uniform heating. The samples were heated to 1100°C and held for 4 h with a 2°C /min heating and cooling ramp rate under argon. During pyrolysis, the Mylar decomposed, leaving a pre-crack in the center of the disk. The pre-crack length, thickness, and diameter were recorded for each sample. At least four samples for each CNT concentration were tested.

Two pieces of rubber were placed between the sample and the compression platens to avoid the crushing at contact points mentioned earlier. An aligner was used to set up the disk perpendicular to the compression platens. Once the disk was clamped between two compression platens with 1 N applied force, the aligner was removed before the compression test. The setup is shown in Fig. 4.1(b). Uniaxial compression tests were performed on an Instron 4204 universal testing machine in constant displacement mode at a displacement rate of 0.5 mm/min.

The toughness was calculated following [7, 28]

$$\begin{aligned} N_I &= \frac{\pi R t}{P \sqrt{\pi a}} K_I \\ &= T_1 A_1(\theta) + T_2 A_2(\theta) + T_3 A_3(\theta) + \dots \end{aligned} \quad (4.3)$$

where N_I is the normalized stress intensity, $2a$ is the length of the pre-crack, R is the radius and t is the thickness of the Brazilian disk, P is the applied load, K_I is the stress intensity factor of mode I, and A_i and T_i s are, respectively, angular and numerical constants. For $\theta = 0$, $A_1 = 1$ and $A_i = 0$ if $i \neq 1$, the expression reduced to

$$K_I = \frac{\sqrt{\pi a}}{\pi R t} P \times T_1 \quad (4.4)$$

where T_1 is a function of a/R and was evaluated/interpolated from the values reported in [7] for each sample. The maximum load associated with crack extension is where $K_I = K_{Ic}$.

4.3 Results and Discussion

4.3.1 Carbon Nanotube Dispersion in Solution and Freeze-cast Structures

Fig. 4.2(a, b) illustrate the effect of dispersants on the carbon nanotube dispersion. The suspension without KD1 in Fig. 4.2(a) had a large cluster of interconnected agglomerates. It is believed that although sonication broke up agglomerates, CNT agglomerates re-formed without a dispersant present [107]. The suspension with KD1 and sonication in Fig. 4.2(b) had no visible agglomerates and did not settle

within the duration of the freezing process. Sonication broke up the CNT agglomerates and the dispersant attached to the surfaces of CNTs, preventing them from entangling with other CNTs again. Adding dispersants and sonicating are two essential steps in successfully dispersing carbon nanotubes and forming a stable dispersion to freeze.

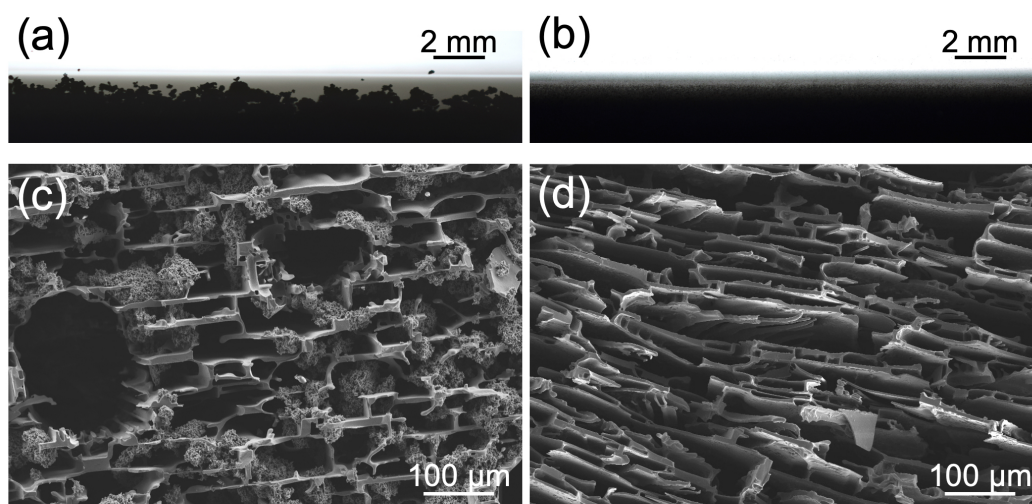


Figure 4.2: Suspensions with 3 mg/ml CNTs and 300 mg/ml MK (a) without, and (b) with KD1. Representative SEM micrographs of the resulting freeze-cast structures with 1.3 wt.% CNTs (c) without and, (d) with KD1.

The effectiveness of the dispersion in suspension has a direct correlation with the uniformity of CNT distribution in freeze-cast structures. Shown in Fig. 4.2(c) is an SEM image of the freeze-cast structure made from the suspension without the dispersant, which had massive agglomerates containing concentrated clusters of CNTs. Macro-pores of more than 100 μm in diameter were created by air bubbles trapped in the suspension due to the high viscosity from poorly-dispersed CNTs. Shown in Fig. 4.2(d) is an SEM image of the freeze-cast structure made from the suspension with the dispersant. It has no visible agglomerates and is similar to typical lamellar freeze-cast structures made with DMC [125]. The comparison demonstrates that the effectiveness of dispersion of CNTs is especially crucial for freeze casting to produce CNT-SiOC composites. In the case of poor CNT dispersion, not only will agglomerates be present, but equally important, the freezing process during freeze casting will be disrupted. With large CNT agglomerates present, the freezing front

splits and engulfs CNTs instead of ejecting them to pore walls as it does with the MK preceramic polymer.

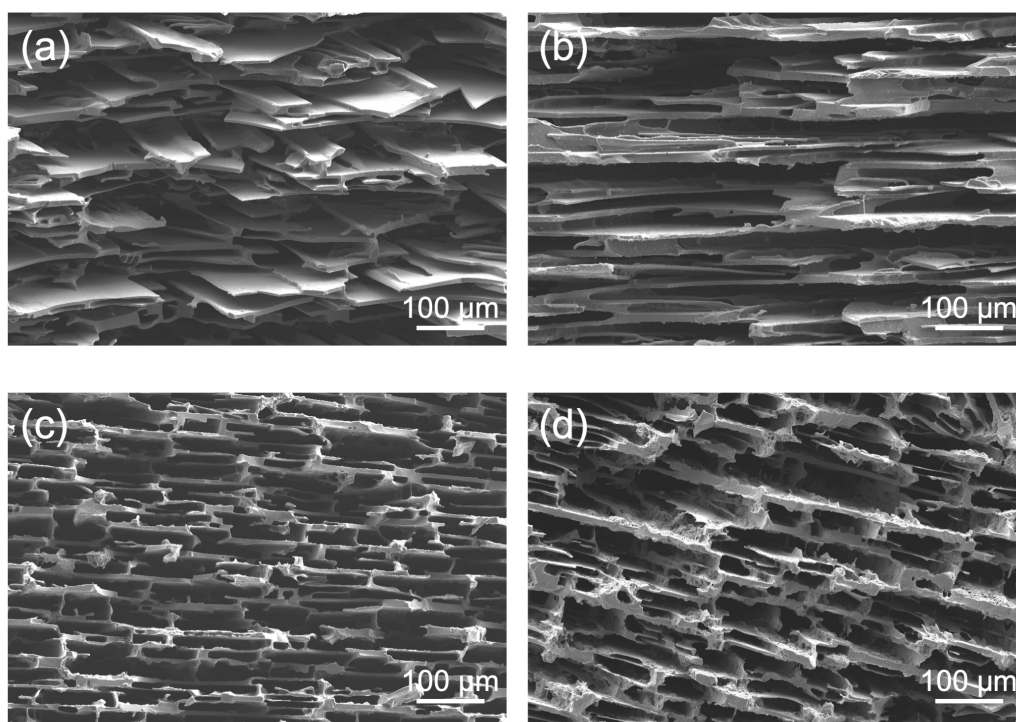


Figure 4.3: Representative SEM micrographs of freeze-cast structures (a) pure SiOC, (b) 1.3, (c) 4.3, (d) 8.2 wt.% CNT composites.

Shown in Fig. 4.3 are SEM images of four freeze-cast samples prepared with both dispersant and sonication, with equal preceramic polymer contents, but with increasing CNTs. With an increasing concentration of CNTs, the agglomerates could not be prevented and protruded from the walls, making the surfaces of walls rougher. If agglomerates were sufficiently large, they formed bridges of CNTs and SiOC between walls as in Fig. 4.3(d). However, despite extra bridges seen in freeze-cast samples with 8.2 wt.% CNTs, overall, the structure did not change significantly compared to CNT-free compositions. Even the freeze-cast structure of the highest CNT concentration (8.2 wt.%) has few small ($<20 \mu\text{m}$) agglomerates, a stark contrast to that made without dispersants in Fig. 4.2(a), having a large number of $>50 \mu\text{m}$ agglomerates with just 1.3 wt.% CNTs.

A closer look at cross-sections of lamellar walls in Fig. 4.4 provides an added view of CNT dispersion—this time within the SiOC walls. We observed localized CNT-

dense regions of 20 to 500 nm, noted by circles in Fig. 4.4(b) through (d), indicative of sub-micron CNT agglomerates, which were reduced in size by several orders of magnitude compared to those of as-received CNTs. As CNT concentration increases, the number of agglomerates increases. No pores or delamination are observed between CNTs and SiOC.

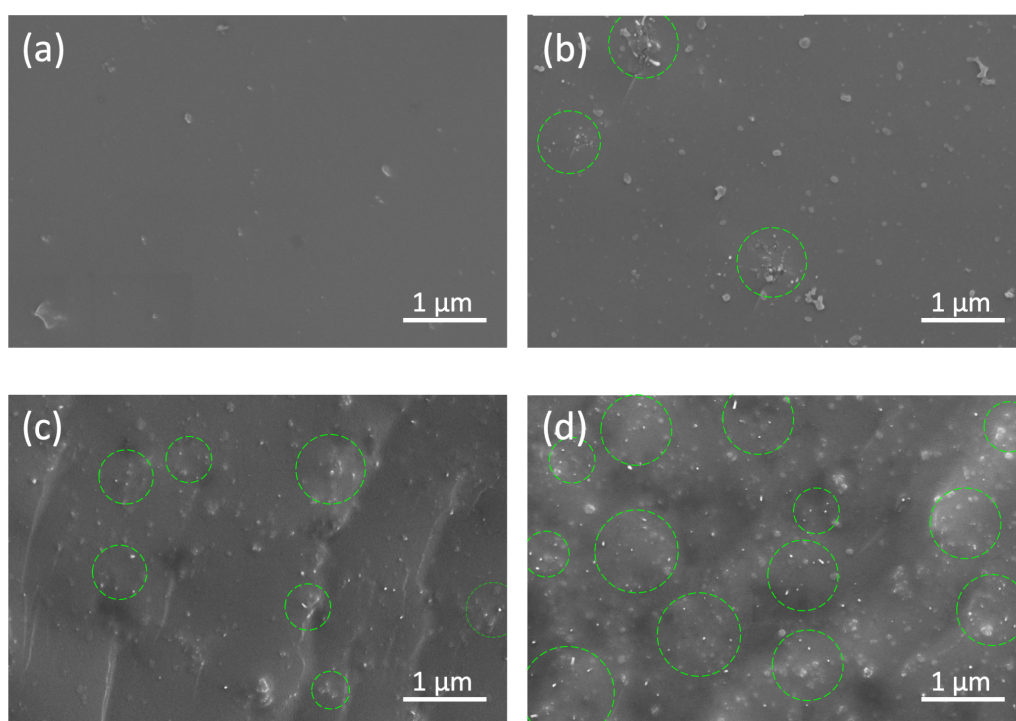


Figure 4.4: Representative SEM micrographs of freeze-cast walls of (a) pure SiOC, (b) 1.3 (c) 4.3, (d) 8.2 wt.% CNT composites. The white dots, present in 1.3, 4.3, 8.2 wt.% samples, are carbon nanotubes. Sub-micron agglomerates are highlighted with green circles.

X-ray diffraction patterns in Fig. 4.5(a) shows that pure SiOC pyrolyzed at 1100°C is structurally amorphous, with a broad peak centered at 23.4°. No distinct crystalline peaks were observed, consistent with the literature [36, 72, 166]. As CNTs are added, new peaks begin to emerge. With peak fitting software, Fityk [187], the XRD pattern was resolved into several peaks, shown in Fig. 4.5(b). Peaks located at 26.0° and 43.6° are attributed to MWCNT. The ratio of the height of the two peaks (ratio ~3) suggest carbons are in the form of MWCNT (ratio ~5) rather than graphite (ratio $\gg 20$) [148]. The peaks from MWCNT confirmed the preservation

of CNTs in the SiOC matrix throughout pyrolysis at 1100°C.

The peak located at 35.6° is likely from SiC [79], formed from the redistribution reactions between Si-O and Si-C bonds and subsequent phase separation of SiOC glass usually at 1200-1400°C [22, 132, 165]. We hypothesize that the extra carbon introduced into the system might have facilitated the formation of SiC. Sujith et al. [171] added graphene nanoplatelets to polysiloxane and also saw peaks of SiC emerge at temperatures as low as 1000°C.

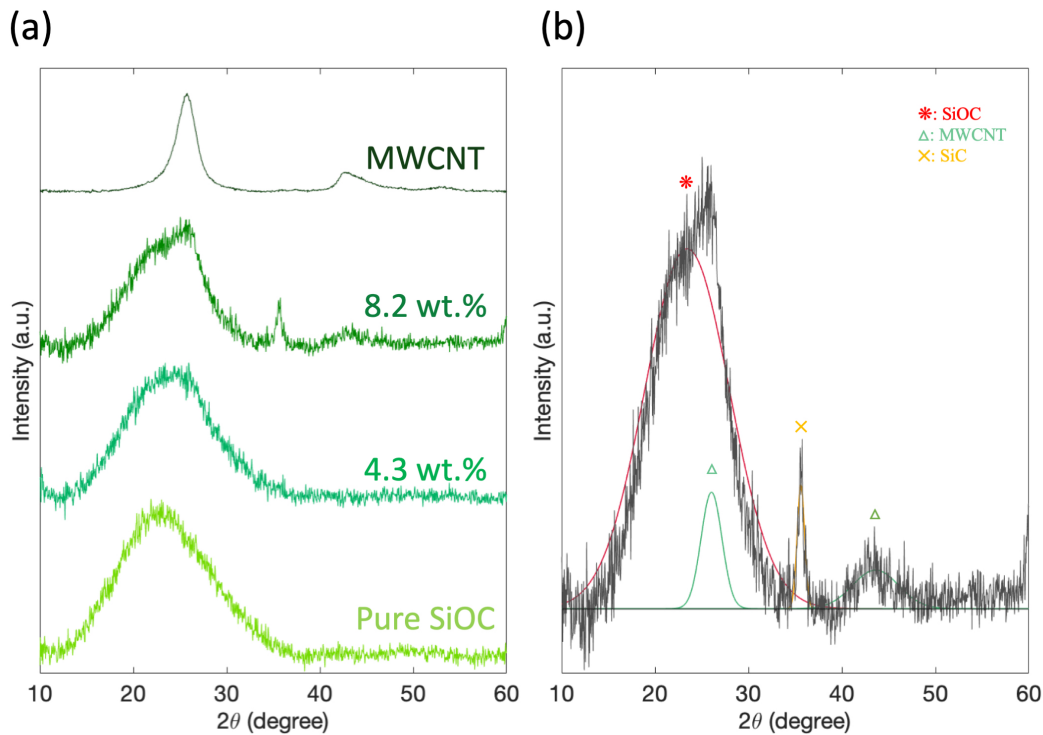


Figure 4.5: (a) XRD pattern of pure SiOC, 4.3, 8.2 wt.% CNT composites and MWCNTs. (b) Background subtraction and peak fitting performed on XRD pattern of 8.2 wt.% CNT composite to identify phases present.

4.3.2 Electrical Conductivity

Plotted in Fig. 4.6 are the conductivities of porous CNT-SiOC composites. Pure SiOC freeze-cast structures are insulating with a conductivity value around 10^{-12} S·cm. Polymer-derived ceramics are typically insulating ($\sigma < 10^{-10}$ S·cm) if pyrolyzed at low temperatures ($< 600^\circ\text{C}$) and semiconducting if pyrolyzed at medium temperatures (800~1400°C) [36], significantly higher than conductivity values of pure SiOC observed here. However, the free carbon concentration and its distri-

bution after pyrolysis play a major role in determining the electrical behavior of polymer-derived ceramics [38]. The ceramics from polysiloxanes have lower carbon contents than those from polycarbosilanes. Among polysiloxanes, MK also produces a much lower carbon content (~ 8 wt.%) compared to those (~ 21 wt.%) from other polysiloxanes (Silres 602, Silres 30, REN 100, H 44, Silres 601, Silres 600 from Wacker Chemie, Munich, Germany) [154]. Therefore, it is expected that ceramics produced from MK will have a lower conductivity than other polymer-derived ceramics. Another factor for the low conductivity observed here is that all the conductivity measurements in [36] were performed on dense ceramics while the conductivity of porous freeze-cast structures was measured here. Conductivity is known to decrease with increasing porosity [104].

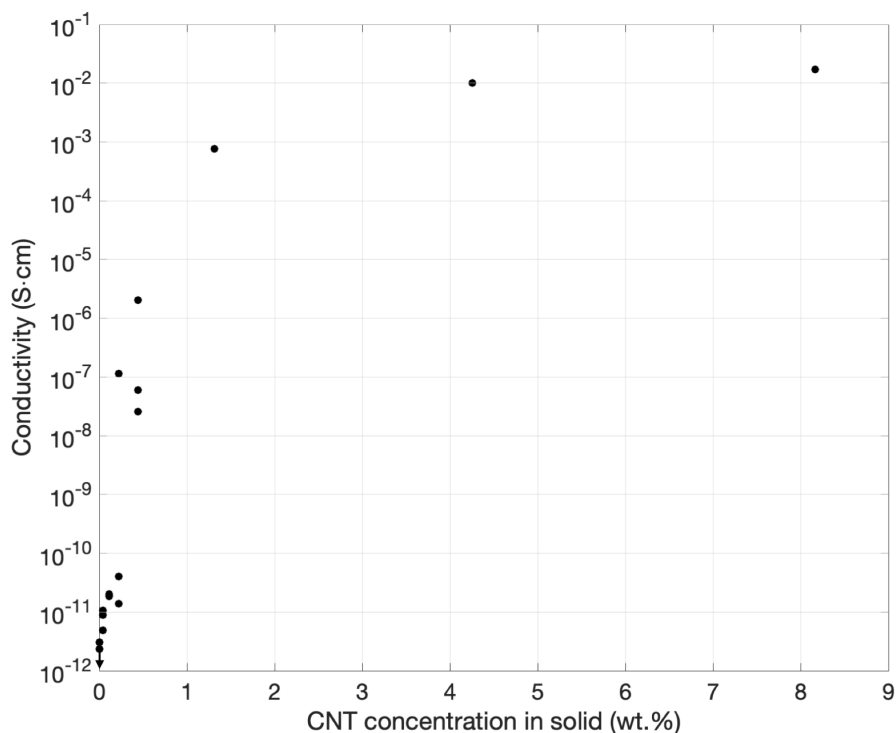


Figure 4.6: Electrical conductivity, calculated without adjustment for porosity, as a function of CNT concentration of freeze-cast composites. The resistance of one pure SiOC sample was above the equipment limit ($200\text{ G}\Omega$) of Keithley 614 Electrometer and its conductivity was calculated using the limit. This data point was plotted with a circle and a downward arrow.

More importantly, a transition from insulating to conductive behavior was observed

with increasing CNT concentration. With as little as 4.3 wt.% CNTs, the conductivity increases by ten orders of magnitude, an indication that the CNTs were largely preserved after the pyrolysis. The critical CNT concentration of electrical percolation was in the range of 0.1 to 0.5 wt.%, well in the range of reported percolation thresholds for nearly 150 CNT-polymer composites reviewed by Bauhofer et al [15].

The excluded volume theory is often used to estimate the electrical percolation limit for non-spherical fillers in a composite. Two conductive fillers would be in contact and increase the conductivity of the composite if the center of one enters a certain surrounding volume of another. This specific volume is the excluded volume of the filler (V_{ex}). The ratio of the excluded volume to the real volume (V) of the filler determines the percolation threshold, Φ_c , and is roughly equal to the inverse of twice the aspect ratio, $D/2L$ [12].

For an aspect ratio ~ 3000 ($D = 12$ nm and $L = 40$ μm), the excluded volume theory predicts a percolation limit of 0.017 vol.%, which is an order of magnitude lower than that observed in the experiment. The discrepancy came from the fact that the excluded volume theory is intended for straight and stiff rods. In addition, the excluded volume theory fails to account for the dispersion and entanglement of objects, which becomes critical for CNTs because of their large aspect ratio. To address these deficiencies, Li et al. [106] introduced two parameters (ξ , ε) to describe the state of the dispersion specifically for CNTs, where ε is a measure of how tightly packed CNTs are in an agglomerate and ξ accounts for the fraction of agglomerates in the dispersion. The percolation limit can be calculated with the following equation:

$$\Phi_c = \frac{\xi\varepsilon\pi}{6} + \frac{27(1-\xi)\pi D^2}{4L^2} \quad (4.5)$$

For high aspect-ratio CNTs dispersed by ultrasonication for hours, Li et al. found ξ and ε to range from 0.01 to 0.05. Based upon Eqn. 4.5, the percolation limit of CNTs was determined to be 0.13 vol.% ($D = 12$ nm, $L = 40$ μm and $\xi = \varepsilon = 0.05$), which closely agrees with the observed percolation limit.

4.3.3 Permeability

Pressure vs. flow rate plots for porous SiOC and CNT-SiOC composites are shown in Fig. 4.7(a), and are largely linear. Inertial permeability (k_2) in Eqn. 4.2 accounts for any non-linearity in the pressure-versus-flow rate data, a common occurrence when the fluid is a gas and the flow velocity is large. Since water was used as the fluid of interest, the inertial permeability term was neglected.

Plotted in Fig. 4.7(b) are the experimental permeability and measured porosity for porous CNT-SiOC composites as a function of CNT concentration. Average permeability constants ranged from 7.9 to $14.9 \times 10^{-12} \text{ m}^2$ with no observable trend with reinforcement fraction. Given the similarity in microstructure (Fig. 4.3), we did not expect to see a significant change in permeability, which was confirmed. Likewise, porosity, often related to permeability, demonstrated no noticeable change with the addition of CNTs. This was expected since the variance in total solid loading in suspensions was less than 1 vol.% (from 19.5 to 20.1 vol.% of the suspension). It is reasonable to deduce that the addition of a small quantity of well-dispersed CNTs neither changes the freeze-cast structures nor the fluid-dynamic properties significantly.

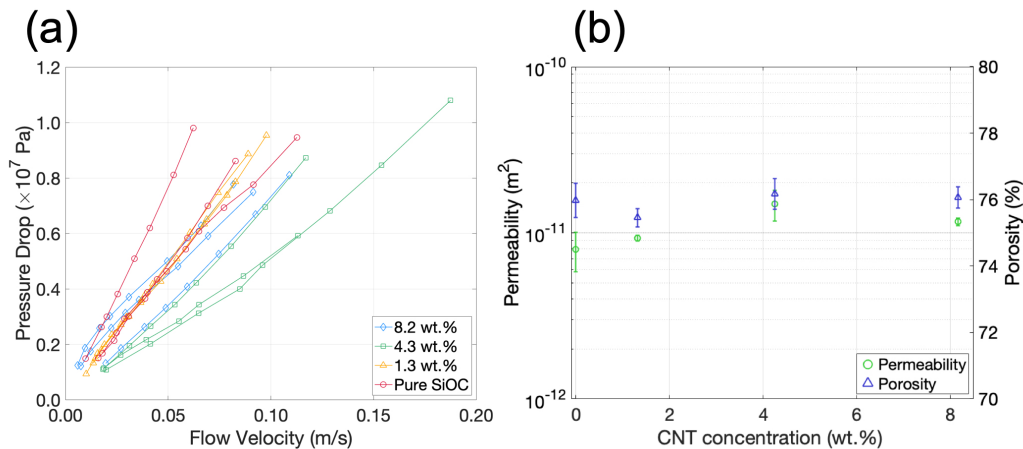


Figure 4.7: (a) Pressure vs. flow velocity to establish permeability of pure SiOC and CNT-SiOC composites. (b) Permeability (circles with lefthand axis) and porosity (triangles with righthand axis) as a function of CNT concentration of freeze-cast composites. Error bars represent \pm one standard deviation.

4.3.4 Mechanical Properties

Shown in Fig. 4.8(a) are representative stress-strain curves of each CNT concentration tested under uniaxial compression. Typically, the fracture behavior for brittle porous structures, as described by Gibson and Ashby, demonstrates a linear rise to a peak followed by a lower stress plateau [65]. This is well-documented in porous structures composed of pure SiOC. With increasing CNT concentration, the stress-

strain curves diverge more and more from the typical fracture behavior. Stress-strain curves of 8.2 wt.% CNT composites sustain a rapidly increasing stress followed by a higher plateau, while CNT concentrations of 1.3 wt.% and 4.3 wt.% show a transient behavior between pure SiOC and 8.2 wt.%. In all cases, CNTs raise the peak stress and plateau in the stress-strain curves.

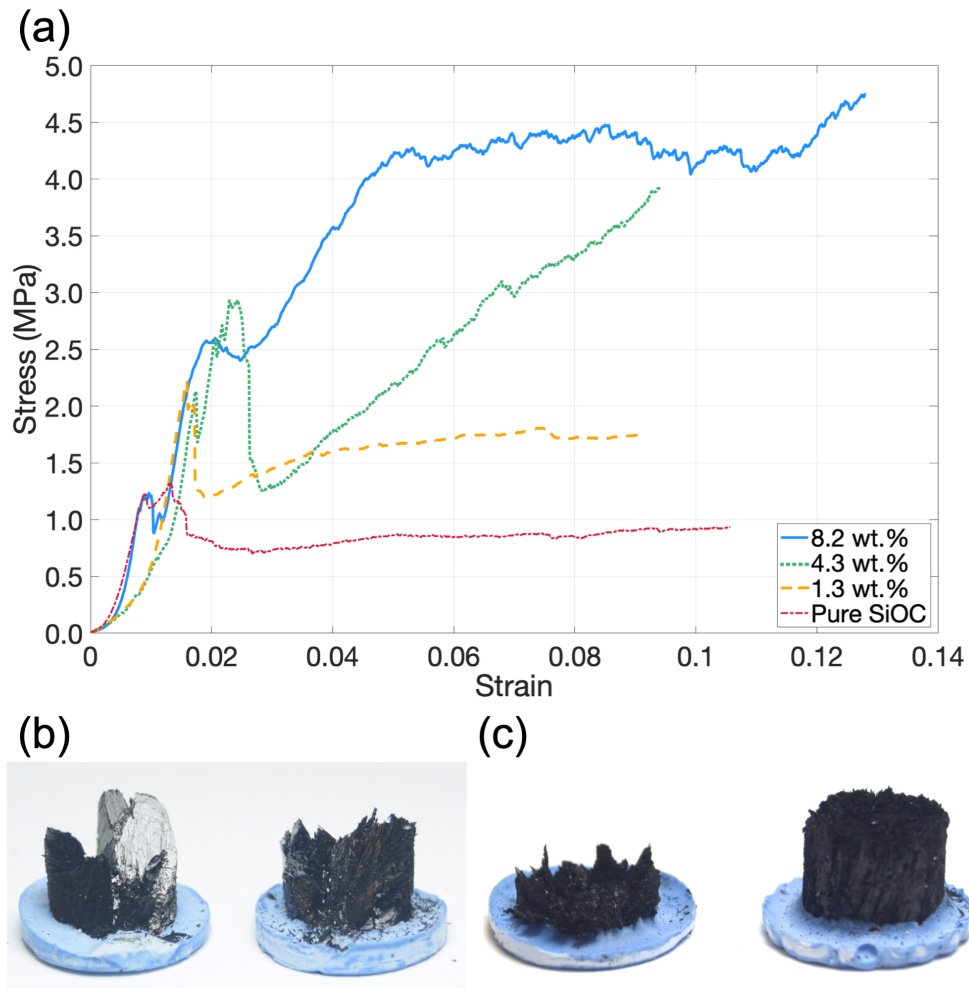


Figure 4.8: (a) Representative stress-strain curves of freeze-cast samples. The first load drop around 1 MPa in most samples is suspected to be from the realignment of the washer. Examples of fractured samples after compression with (b) pure SiOC and (c) 8.2 wt.% CNTs. The blue disk-like capping is a cured mineral-filled acrylic applied to avoid crushing behavior common in compression tests of porous ceramics.

The change in fracture behavior with the addition of CNTs can also be seen in

Fig. 4.8(b, c), macroscopic views of fractured samples of uniaxial compression. In pure SiOC samples, the fracture occurs along lamellar walls, along directions of maximum shear. The samples fail by bridge fracture and lamellar wall sliding, resulting in a substantial load drop as observed early in the stress-strain curve. At the largest CNT concentration tested (8.2 wt.%), fracture occurs perpendicular to the applied force, exhibiting a rough fracture plane. Here samples fail by lamellar wall bending and buckling. The failure arises cell-by-cell, which manifests as an effective hardening accentuated with small load drops.

One likely explanation for this difference in fracture mode (shear vs. wall bending and buckling) with the addition of carbon nanotubes is bridging from CNT agglomerates, as seen in Fig. 4.3(d).

For pure SiOC, DMC produces relatively smooth lamellae with few bridges in-between (Fig. 4.9(a)). As the CNT concentration is increased, the agglomerates, noted first with 4.3 wt.% CNTs, increase in size. If agglomerates are larger than the lamellar spacing, we hypothesize that they form bridges between the lamellar walls, consistent with the images in Fig. 4.9(b). The bridges between lamellar walls make shear failure unfavorable, in contrast to that demonstrated in pure SiOC and SiOC with low CNT concentrations, and ultimately lead to a higher plateau in stress-strain curves.

The evidence of the structural difference contributing to the change in fracture mode can also be observed in the fracture surfaces (Fig. 4.9(c, d)). For pure SiOC, the fracture surface is a clean lamellar surface with little contact between one lamella and another. Lamellae are able to slide over one another easily without breaking lamellar planes. (Fig. 4.9(c)). On the other hand, the fracture surface of the 8.2 wt.% CNT composite exhibits a broken surface of lamellae with bridging agglomerates. The bridges prevent the sliding between lamellae (Fig. 4.9(d)).

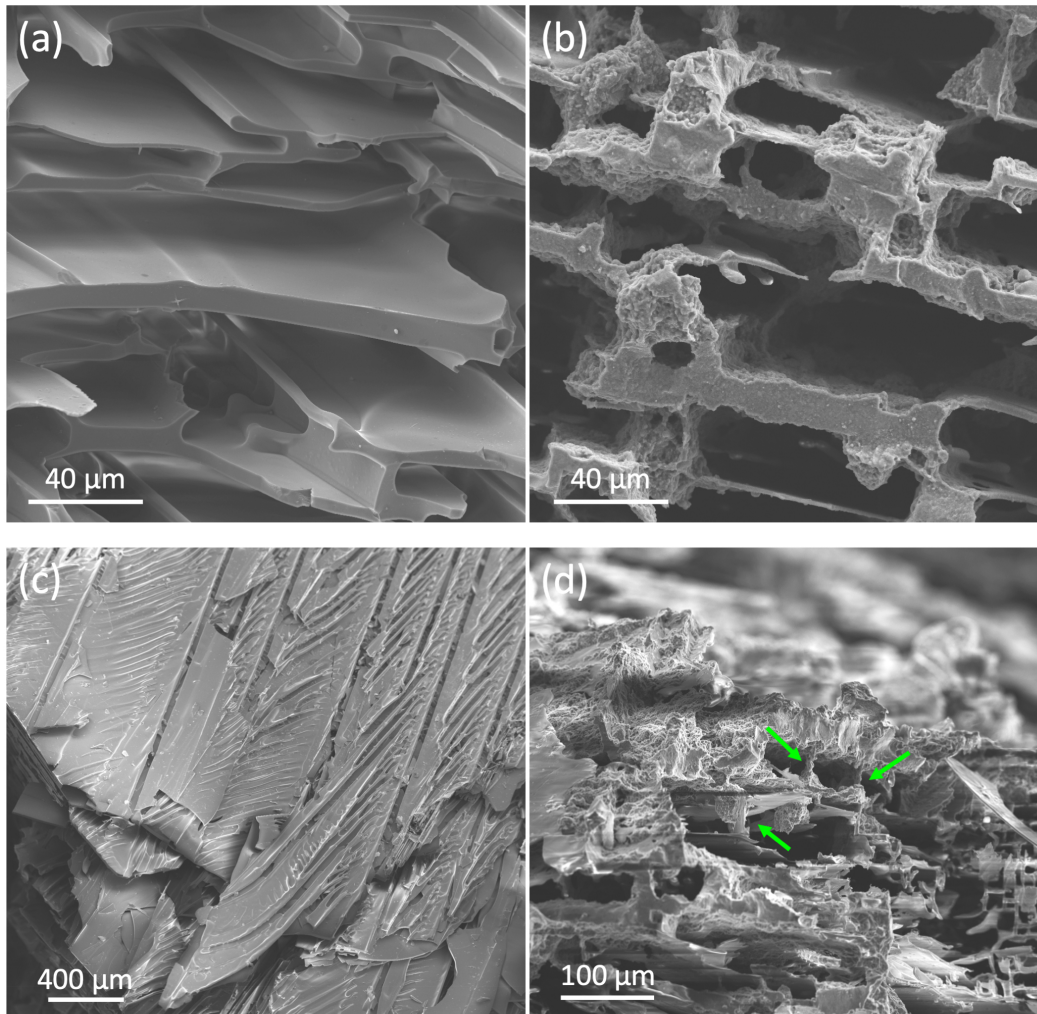


Figure 4.9: SEM micrographs of freeze-cast and pyrolyzed walls of (a) pure SiOC and (b) 8.2 wt.% CNTs. In pure SiOC, the lamellae are smooth with few features and bridges. In the 8.2 wt.% composite, the lamellae are bridged with CNT agglomerates. SEM micrographs of fracture surfaces with (c) pure SiOC and (d) 8.2 wt.% CNTs. The green arrows in (d) point to the agglomerate bridges between lamellae.

The strengthening effect of carbon nanotubes in freeze-cast structures is illustrated in Fig. 4.10(a), which documents the compressive strength as determined by the initial peak load. The strength increases with increasing concentration of CNTs with the exception of SiOC with 8.2 wt.% CNTs. Unlike those for other CNT concentrations, the peak stress can hardly be distinguished from the high plateau, and is therefore not included here. With the exception of agglomeration effects in the 8.2 wt.% CNT composite and discussed in [9], the strengthening enhancement

is consistent with short-fiber reinforcement models, where load can be transferred between the CNT and SiOC matrix [34, 60].

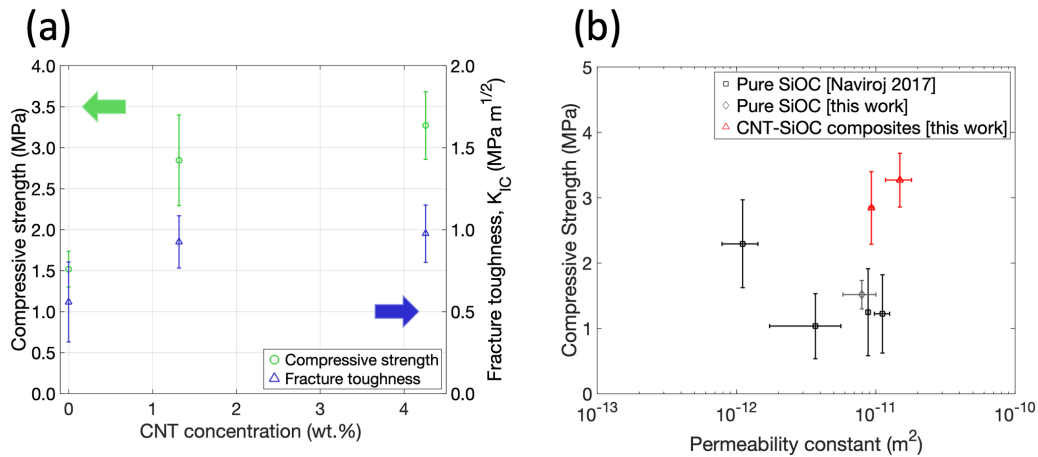


Figure 4.10: (a) Compressive strength and fracture toughness as a function of CNT concentration. (b) Compressive strength vs. permeability constant of freeze-cast CNT-SiOC composites compared with that of pure SiOC both in this work and the values reported by Naviroj [125]. Error bars represent \pm one standard deviation.

To understand the reason for the increase in the peak load, we examined how CNTs influence the fracture toughness of the SiOC-CNT walls. Shown in Fig. 4.10(a) are values of fracture toughness for SiOC samples as a function of CNT concentration. These values follow the same trend as the compressive strength, with 57% and 74% increase for 1.3 wt.% and 4.3 wt.% CNTs, respectively. It is reasonable to argue the freeze-cast walls with higher toughness can withstand a higher stress before fracture as exemplified by an increase the peak load of freeze-cast CNT-SiOC composites.

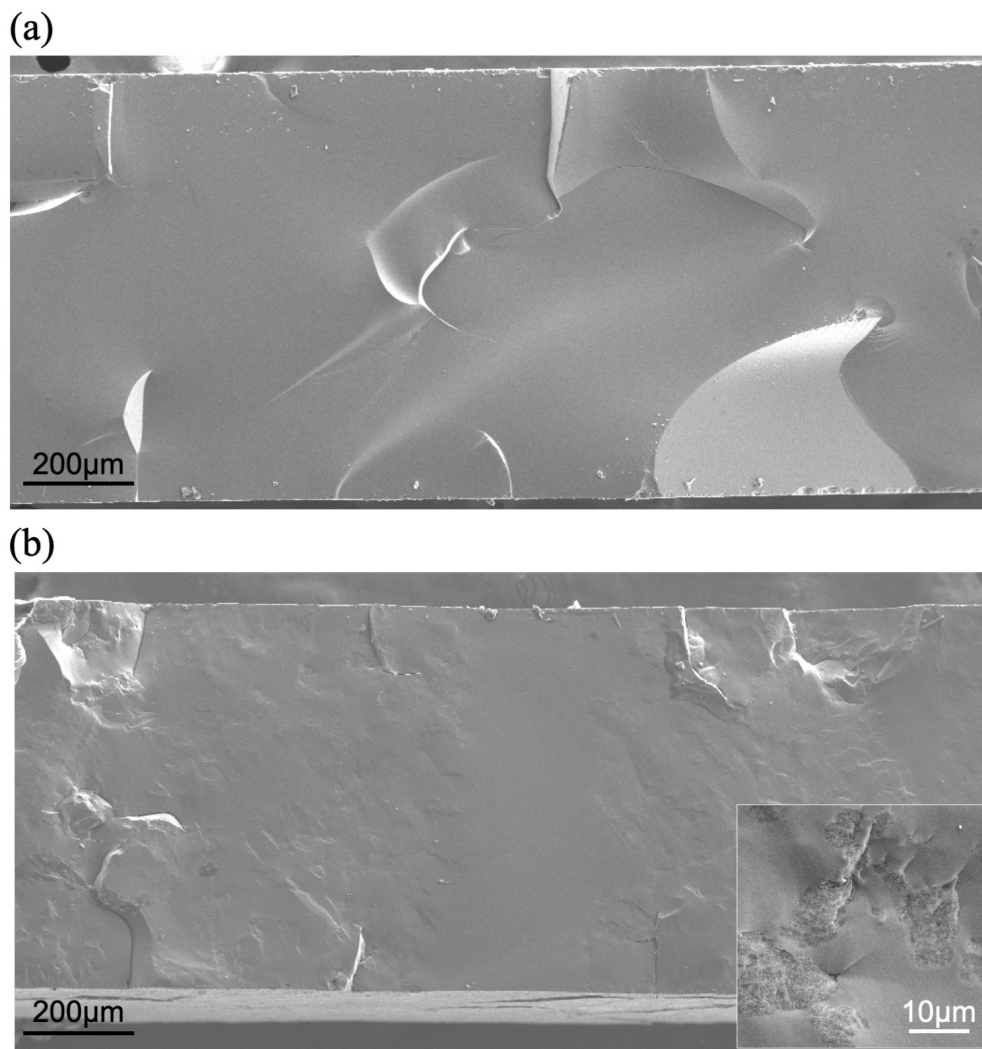


Figure 4.11: Representative SEM micrographs of fracture surfaces of Brazilian disks of (a) pure SiOC and (b) 4.3 wt.% CNTs. The insets in (b) shows a magnified image of a fracture surface of 4.3 wt.% CNT composites. The rough patches, appearing in 4.3 wt.% composites, are clusters of CNT agglomerates.

Fracture surfaces of Brazilian disks of pure SiOC and with 4.3 wt.% CNTs are compared in Fig. 4.11. Pure SiOC (Fig. 4.11 (a)) exhibits the typical glassy and smooth surface of amorphous brittle materials while that of 4.3 wt.% CNT composite (Fig. 4.11(b)) has rough patches where CNT agglomerates are located. The inset shows a magnified image of Fig. 4.11(b). Interestingly, the CNT agglomerates in the Brazilian disk are larger both in size and number than those in freeze-cast CNT composites of the same CNT concentration. It is likely due to the difference in fabrication methods used for freeze-cast samples and Brazilian disks. For Brazilian

disks, the CNT dispersion was achieved through mixing CNTs in powder form with the preceramic polymer powders without sonication or the addition of dispersant.

As previously mentioned, two major challenges with CNT reinforcement of ceramics are the damage done to CNTs by high temperature and pressure required to densify ceramic powders, and difficulties to achieve homogeneous dispersion of CNT with powder process. To prevent damage, some researchers report a low-temperature fast-sintering technique, spark-plasma sintering, while others used preceramic polymers, which convert to bulk ceramics under ambient pressure and relatively low temperature. In this work, we have addressed both issues by utilizing both preceramic polymer and sonication in solution, known to produce well-dispersed CNT composites. We compared our results with CNT-ceramic composites sintered by spark plasma sintering (Zhan et al. [197]) and those made from preceramic polymers (Katsuda et al. [85]). Zhan et al reported 139% and 176% increase in toughness for 5.7 and 10 vol.% (approximately 3.1 and 5.6 wt.%), respectively. Katsuda et al. reported 49% and 72% increase in toughness for 1, 2 wt.%. Both results are on par with the toughness increase we observed.

The reinforcing effect of CNTs on freeze-cast CNT-SiOC composites is demonstrated both in the fracture toughness and compression tests; CNTs in freeze-cast walls result in tougher walls, and consequently increase the peak load of the freeze-cast structure. The agglomerate bridges of CNTs prevent shear failures by making fracture along the lamellar walls unfavorable, leading to a higher plateau in stress-strain curves. The two factors, both introduced by the addition of CNTs, improve the durability of freeze-cast CNT-SiOC composites.

Finally, Fig. 4.10(b) shows compressive strength versus permeability of freeze-cast CNT-SiOC composites compared with that of freeze-cast pure SiOC both from this work and values reported by Naviroj [125]. Freeze-cast pure SiOC samples in [125] have similar values in compressive strength and permeability. The best CNT-SiOC composite, however, achieved a markedly higher compressive strength of 3.3 MPa and a similar permeability constant of $11.7 \times 10^{-12} \text{ m}^2$. It is demonstrated here that by introducing CNTs into the SiOC matrices as reinforcements, the compressive strengths were doubled at virtually no cost to permeability, making this method ideal for fabricating high load-bearing directional porous ceramics for transport and filter applications.

4.4 Conclusions and Implications

Challenges of combining the high aspect ratio reinforcements with freeze-casting to produce porous composites have been systematically addressed. To avoid altering freezing dynamics, the concentrations of fillers were chosen to be less than 2 wt.% of the suspensions. MWCNTs were selected as fillers so that the reinforcement was sufficient even at low concentrations. The addition of dispersants (KD1) combined with sonication was shown to greatly reduce CNT agglomerates, allowing for stable suspensions. Not surprisingly, there was an increase in the size and number of CNT agglomerates with increasing CNT concentration. However, it was shown that if CNTs were well dispersed in suspension, the addition of CNTs would not change the pore structures notably.

The electrical conductivity changed drastically by 10 orders of magnitude with the addition of 8.2 wt.% CNTs, and the transition from insulating to conductive was found to be around 0.1 to 0.5 wt.%. This significant increase in conductivity indicated the preservation of CNTs after pyrolysis. Permeability was largely unaffected by the addition of CNTs and followed a similar trend with porosity as unreinforced lamellar freeze-cast solids.

With the introduction of as little as 1.3 and 4.3 wt.% CNTs in porous SiOC ceramics, the compressive strength increased by 88% and 118%, respectively. Two different fracture behaviors were observed. Freeze-cast samples of pure SiOC fractured in shear parallel to lamellar walls. The stress-strain response featured a peak stress followed by a low-strength plateau. At the highest CNT concentration tested (8.2 wt.%), fracture perpendicular to the load direction and lamellar walls was favored. In stress-strain curves, the peak became less pronounced and more difficult to distinguish from the following high-strength plateau. In addition, the prevention of shear failure by bridges formed from CNT agglomerates increases the stress at which the plateau occurs.

Disks of SiOC and CNT-SiOC were made to investigate the effects of CNTs on the walls. The fracture toughness, determined with diametral compression, increased by 57% and 74 %, respectively, for 1.3 and 4.3 wt.% CNTs added. The toughness follows a similar trend seen in compressive strength. The toughening of bulk disk samples, analogous to the walls, increases the peak stress in the stress-strain curve of the freeze-cast structure. The reinforcing effect of CNTs on the walls, along with prevention of shear failure by CNT bridges, increases the compressive strength, changes the fracture behavior and, overall, improves the load-bearing capabilities of

freeze-cast CNT-SiOC composites. The potential of this method has been demonstrated through measurements of permeability, conductivity, compressive strength, and fracture toughness. CNTs as reinforcements have successfully improved the mechanical properties of porous SiOC without affecting permeability, rendering this technique powerful in fabricating robust porous ceramics.

HIERARCHICAL COMPOSITES VIA SELF-ASSEMBLY OF BLOCK COPOLYMER

Material in this chapter is reproduced in part from "Hierarchical porous SiOC via freeze casting and self-assembly of block copolymers", C.T. Kuo, L.M. Rueschhoff, M.B. Dickerson, T.A. Patel, K.T. Faber; *Scripta Materialia*, 191 (2021) 204–209. The work was done in collaboration with Lisa M. Rueschhoff, Matthew B. Dickerson, Tulsi A. Patel of the Air Force Research Laboratory, and Katherine T. Faber. T. Kuo fabricated and characterized hierarchical ceramics using SEM, MIP, and N₂ adsorption isotherms, characterized weight loss, volume shrinkage, compressive strengths, and permeabilities, conducted image analysis on X-ray computed tomography (XCT) datasets, and wrote the majority of the manuscript. L.M. Rueschhoff characterized the BCP-PCP and its PDC system. T.A. Patel performed XCT. K. Faber and M.B. Dickerson supervised this work.

5.1 Introduction

Chapters 3 and 4 explored the challenges and opportunities of filler-reinforced high-permeability pore structures by SiC whiskers and CNTs, respectively. Once a pore structure is optimized for its mechanical and transport properties, its surface area can be increased by creating a high-surface-area mesoporous coating on top of the original pore structure, effectively constructing a hierarchical structure with large pores for fluid transport and small pores which produce high surface area for capture or catalytic reactions.

Procedures that utilize molecular templates such as surfactants or block copolymers (BCPs) are advantageous for the creation of mesoporous ceramics [39, 96, 139, 158]. Rueschhoff et al. [147] deposited polymer films with a BCP and polycarbosilane preceramic polymer (PCP) blend that formed interconnected spherical micelles. These were pyrolyzed to produce mesoporous silicon carbide-based (SiC-based) ceramic films, shown in Fig. 5.1(a). In this work, we adopt this BCP/PCP system with freeze casting to fabricate a hierarchical structure.

While various synthesis methods of hierarchical structures and their respective surface areas have been discussed in literature [36, 195, 198], mechanical performance

is often overlooked and warrants consideration. Retaining the desired mechanical properties and permeability with added pore hierarchy is often a challenge to practicability for applications such as filters, electrodes, and catalyst supports. In this chapter, we address this challenge by coupling directional freeze casting of a preceramic polymer as the macroporous template with a self-assembled block copolymer-preceramic polymer blend to provide a conformal mesoporous coating on the macropore walls. The processing methodology, and resultant microstructures, compressive strength, permeability and surface area of the hierarchical pore structures are featured.

5.2 Experimental Methods

5.2.1 Materials and Processing

The macroporous scaffold for the hierarchical porous structure was prepared via directional freeze casting as described in [124]. Twenty wt.% polysiloxane preceramic polymer (Silres® MK Powder, $\text{CH}_3\text{-SiO}_{1.5}$, Wacker Chemie, Munich, Germany) was dissolved in dimethyl carbonate (DMC, Sigma-Aldrich, MO, US). Ten $\mu\text{l/g}$ (agent/solution) of cross-linking agent (N-(2-Aminoethyl)-3-aminopropyltrimethoxysilane, Geniosil GF 91, Wacker Chemie, Munich, Germany) was added into the solution. The solution was then poured into a glass mold with an inner diameter of 24 mm, and quenched at -30°C . After solidification, the sample was dried in a lyophilizer (Virtis Wizard 2.0, SP Scientific, PA, US) until the solvent was removed. The bottom one millimeter of the sample was polished off with sandpaper to improve infiltration before curing at 200°C in advance of infiltration with BCP/PCP gel.

The mesoporous coating was prepared via self-assembly of the BCP (Kurarity™ LA4285, PMMA-PnBA-PMMA, Kuraray America, Inc., Houston, TX, US). The BCP and a polycarbosilane preceramic polymer (StarPCSTM SMP-10, Starfire Systems Inc., Glenville, NY, US) were dissolved in 2-ethyl-1-hexanol (2EH, Sigma-Aldrich, MO, US) to form a BCP/PCP gel, a physical polymer blend with no chemical interaction between the two polymers [147]. The freeze-cast scaffold was infiltrated with the BCP/PCP solution at 80°C using vacuum. After infiltration, the sample was dried for at least 4 days, then cured and pyrolyzed at 230 and 900°C , respectively. During pyrolysis, freeze-cast polysiloxane walls were converted into amorphous SiO_2 -rich silicon oxycarbide (SiOC)

[36, 125, 154], while the porous coating formed on the freeze-cast walls through the removal of the fugitive BCP phase and the conversion of polycarbosilane into

amorphous SiOC (Table 5.1) [86]. Elemental analysis of the derived SiOC from the BCP/PCP gel system has been reported in [21, 147]. Thermogravimetric (TGA) analysis [147] indicates a general rule of mixtures for the ceramic yield of a similar BCP/PCP systems, demonstrating that the BCP addition does not change the ceramic yield of the SMP-10. The synthesis process of these hierarchical samples (designated as Hierarchical20) is illustrated in Fig.5.1(b). Fourier-transform infrared spectroscopy (FTIR) spectra of both MK and SMP-10 polymers and the derived SiOC ceramics indicate complete conversion of the preceramic polymers to ceramics after pyrolysis [125, 147].

Table 5.1: Chemical composition (in weight percent) of MK- and SMP-10-derived ceramics. The elemental analyses were conducted with a thermobarometrical redox analysis [154, 185] and by a carbon analyzer [86].

Precursor polymer	SiO ₂	SiC	C
MK [154]	76.01	15.98	8.00
SMP-10 [86]	10.69	82.08	7.21

For comparison, the sample denoted as Freezecast20 had the same polymer concentration as Hierarchical20 in the freeze-casting stage. However, it was pyrolyzed directly after freeze casting without infiltration of BCP/TCP. Three other freeze-cast samples with varying polymer concentrations (Freezecast15, Freezecast25, Freezecast35) were produced to establish baseline compressive strength and permeability. Polymer concentrations and average porosities ranging from 63.0 to 83.1% were determined by Archimedes' method (following ASTM C373) and are summarized in Table 5.2.

Table 5.2: Average porosity after pyrolysis of all Freezecast and Hierarchical20 samples. Six samples were tested for each polymer concentration.

	MK Polymer concentration (wt.%)	Average porosity (%)
Freezecast15	15	83.1 ± 0.4
Freezecast20	20	78.3 ± 0.6
Freezecast25	25	73.1 ± 0.9
Freezecast35	35	63.0 ± 0.8
Hierarchical20	20	72.8 ± 0.7

5.2.2 Pore Structure

The pore structure was imaged using scanning electron microscopy (ZEISS 1550VP FESEM, Carl Zeiss Microscopy GmbH, Jena, Germany) and X-ray computed tomography (X-ray CT, ZEISS Xradia 520 Versa, Carl Zeiss Microscopy GmbH, Jena, Germany). For the latter, a 120 kV and 10 W X-ray source was used with an exposure time of 25 sec. A total of 2401 projections were obtained about the field of view from -180° to 180° , which were manually reconstructed in the Zeiss Reconstructor program; beam hardening was corrected for and 2D reconstructed slices of all three orthogonal planes were written through the Zeiss XMController program. The resulting tomograms have a resolution of $1.52 \mu\text{m}/\text{pixel}$ and were circles with a radius of $736 \mu\text{m}$ in one direction and $1482 \times 1487 \mu\text{m}^2$ rectangles in two directions.

The pore size distribution was determined with a mercury intrusion porosimeter (MIP, AutoPore IV 9500, Micromeritics Instrument Corp., Norcross, GA, US). Nitrogen adsorption data were collected with TriStar II 3020 analyzer (Micromeritics Instrument Corp., Norcross, GA, US). The samples were ground into powders and degassed at 300°C under vacuum for 3 h prior to measurements. The BET surface area [23] was determined under relative pressures of 0.02-0.15 with a correlation coefficient of 0.999.

5.2.3 Permeability

Permeability was determined from the flow rate of water through cylindrical samples ~ 4.5 mm tall and ~ 9.5 mm wide over a series of pressure drops, using an experimental set-up described in [97]. Three samples were tested for each processing condition. The permeability was calculated with Darcy-Forchheimer equation [78]:

$$\frac{\Delta P}{L} = \frac{\mu}{k_1} v + \frac{\rho}{k_2} v^2 \quad (5.1)$$

where ΔP is the pressure drop across the sample, L is the thickness of the sample, and μ , ρ , v are the dynamic viscosity, density, and flow velocity of water, respectively. The parameters k_1 and k_2 are the intrinsic and inertial permeabilities, respectively; the latter describes non-linear flow. Given the linearity of the data collected, the non-linear term was ignored.

5.2.4 Mechanical Properties

To determine the compressive strength and Young's modulus, mechanical tests were performed on cylindrical samples ~ 6 mm tall and ~ 9.5 mm in diameter using an

Instron 5960 Series Universal Testing System (Instron, MA, US). The compressive load was applied parallel to the axis of freezing direction under a constant displacement rate of 0.05 mm/min. The top and bottom of the samples were capped with a low-shrinkage acrylic system (VariDur 3003, Buehler, IL, US) to minimize contact stresses. Details of the setup can be found in [97]. The peak load was used to calculate compressive strength. Three samples were tested for each processing condition.

5.3 Results and Discussion

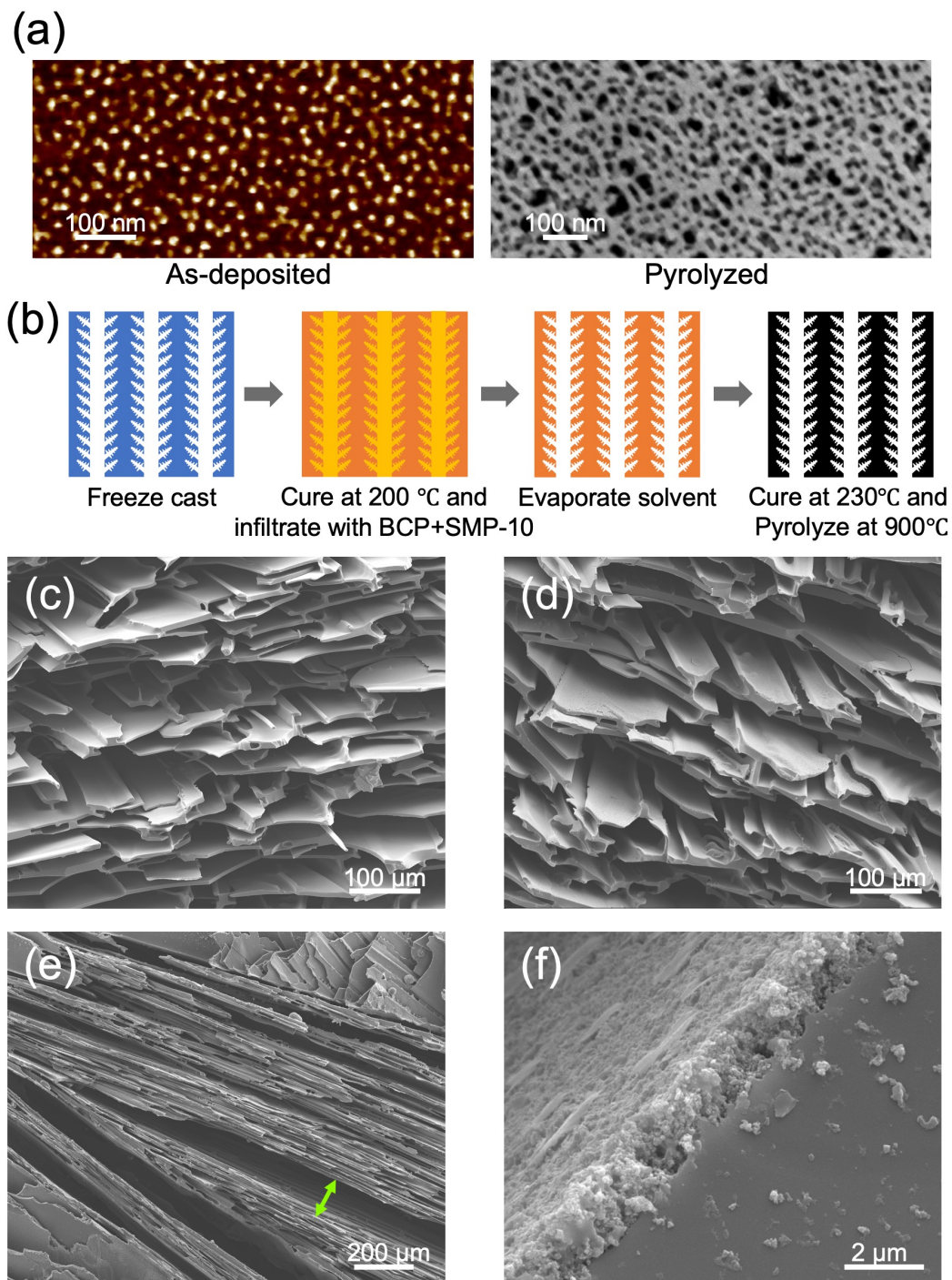


Figure 5.1: (a) AFM phase view of as-deposited films (left) and SEM image of pyrolyzed films (right) made with BCP/PCP gel. (b) Schematic of the synthesis process for Hierarchical20. SEM images of pyrolyzed freeze-cast structures of (c) Frezecast20 and (d) Hierarchical20, with (e) enlarged lamellar spacings and (f) porous conformal coating on the freeze-cast pore wall of Hierarchical20.

Fig. 5.1 shows cross-section SEM images of pyrolyzed (c) Freezecast20 and (d) Hierarchical20. Lamellar freeze-cast structures, typical of DMC, were seen in both Freezecast20 and Hierarchical20. The freeze-cast structure remains largely intact after infiltration and pyrolysis, except for the creation of selected large lamellar spacings shown in Fig. 5.1(e). Fig. 5.1(f) reveals the mesoporous coating on the surface of the freeze-cast pore walls, resulting from the infiltration of BCP/PCP gel. There was no delamination between the coating and the scaffold during the simultaneous conversion of polysiloxane and polycarbosilane into SiOC during pyrolysis. This is in contrast to flaking that is seen in some other synthesis processes for hierarchical structures [39].

This bimodal pore size distribution of the hierarchical pore structure was confirmed with MIP in Fig. 5.2, with peaks around 30 nm and 20 μm for Hierarchical20 sample. Macropores from freeze casting are observed in both Hierarchical20 and Freezecast20 albeit smaller in size and volume for Hierarchical20 due to the mesoporous coating on freeze-cast pore walls. The presence of 30-nm pores from BCP templating was unique to Hierarchical20 and consistent with the nominal size gathered from image analysis reported in [21]. Of the 69.1% porosity in Hierarchical20, 2.3% were smaller than 1 μm .

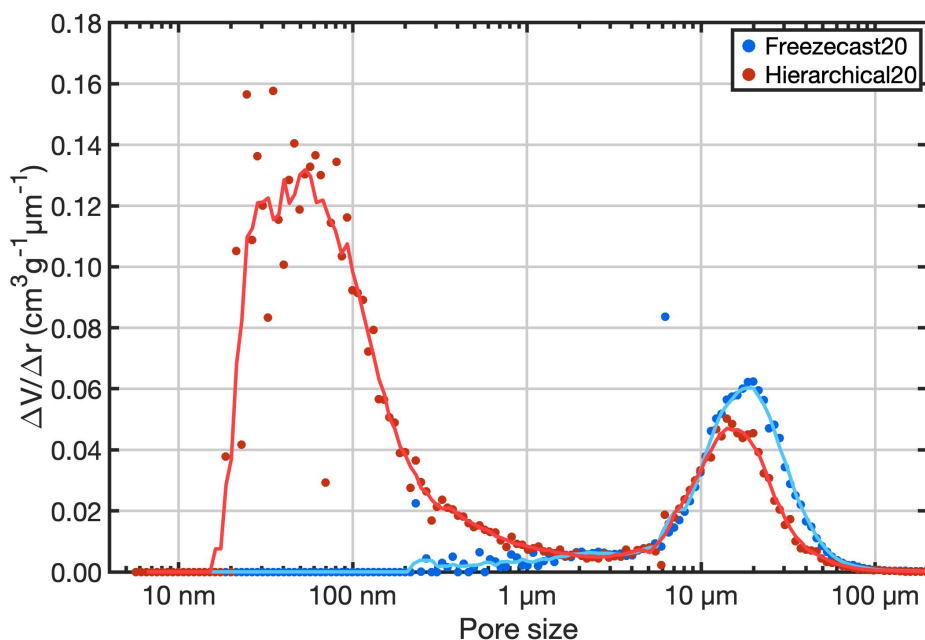


Figure 5.2: Pore size distribution of Hierarchical20 and Freezecast20 pore structure from MIP. Smoothing of the data, indicated by solid lines, was performed by averaging sets of five consecutive points minus outliers.

In Fig. 5.1(e), dilated lamellar spacings were estimated to be nearly ten times larger than surrounding lamellar spacings. The enlarged spacings are likely a result of the infiltration and subsequent drying of the BCP/PCP gel. To understand how infiltration affected the freeze-cast structure quantitatively, volume and weight changes after each processing step were recorded (Table 5.3).

Table 5.3: Volume and weight changes (in percent) after each processing step of Freezecast20 and Hierarchical20. At least five samples are measured for each step.

		Infiltration	Solvent evaporation	Pyrolysis	Total
Freezecast20	Volume (%)	NA	NA	-47.2 ± 1.4	-47.2 ± 1.4
	Weight (%)	NA	NA	-16.3 ± 0.5	-16.3 ± 0.5
Hierarchical20	Volume (%)	$+15.7 \pm 2.4$	-8.0 ± 2.6	-48.5 ± 0.7	-45.2 ± 0.6
	Weight (%)	$+264.3 \pm 5.2$	-61.0 ± 0.7	-25.8 ± 1.0	$+5.4 \pm 0.6$

During infiltration, BCP/PCP gel completely fills the freeze-cast pores and pushes pore walls apart, resulting in an increase in volume. It has been reported that

during the drying stage of similar BCP gel systems, the capillary stresses from the evaporation of solvent could cause warpage [162]. In the current work, the stresses could pull some walls back while leaving others separated, generating a decrease in volume. The infiltration and drying steps combined create a 6% and 42% increase in volume and weight, respectively, before pyrolysis. Pyrolyzed Hierarchical20 shrank less than Freezecast20 (45.2% vs. 47.2%) compared to the freeze-cast green body. The difference in volume change was found to be statistically significant with a p-value of 2.1×10^{-3} . The concentration of enlarged lamellar spacings was determined from stereological arguments [44], but was found to be only 0.27% showing that the freeze-cast structures were still largely preserved. The large increase in weight for Hierarchical20 in contrast to Freezecast20 results in a lower porosity despite the sporadic presence of large lamellar spacings.

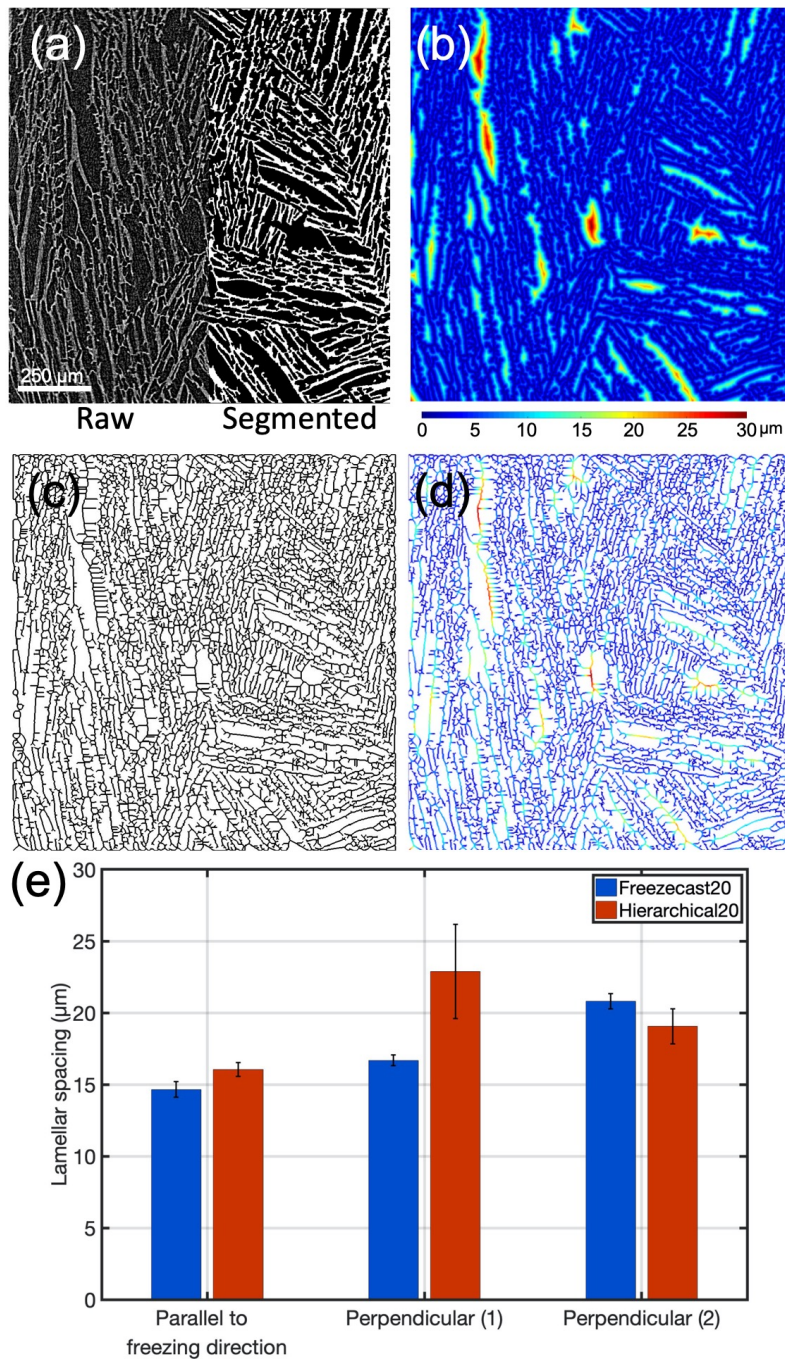


Figure 5.3: Stages of the lamellar spacing analysis from X-ray CT (A tomogram of Hierarchical20 is used as an example) (a) Original 2D image and segmented image (b) Euclidean distance map (c) 2D skeleton of lamellar pores (d) Graphic representation of lamellar spacing measurements (e) Average lamellar spacings from image analysis of 2D X-ray tomograms.

Image analysis was performed on about 300 X-ray tomograms (of 2401 collected)

for Hierarchical20 and Freezecast20 in three directions using MATLAB to assess average interlamellar spacing. Three orthogonal directions were chosen to reflect the overall structure, with one parallel to freezing direction, reflecting the samples' anisotropy, and two directions perpendicular to the freezing direction and each other to account for the effect of image sectioning on lamellar spacing.

Examples of images from the step-wise analysis are shown in Figs. 5.3(a) through (d). Each of the images was cropped, thresholded, and cleaned to perform image segmentation (Fig. 5.3(a)). The distance from any point to its nearest center of lamellar wall was measured to construct the Euclidean distance map (Fig. 5.3(b)). The lamellar pores were then skeletonized (Fig. 5.3(c)). The distances between the pore centers and the centers of nearest walls, i.e. half of the lamellar spacing, were assessed by multiplying the Euclidean distance map (Fig. 5.3(b)) by the pore skeleton (Fig. 5.3(c)) and are mapped in Fig. 5.3(d). The average lamellar spacings of three imaging directions are presented in Fig. 5.3(e). The bar chart shows that, on average, the lamellar spacing increases with the infiltration. The increase is attributed to selectively enlarged lamellar spacings (0.27%) noted in SEM (Fig. 5.1(f)) and in the volume difference ($\sim 3\%$) between pyrolyzed Hierarchical20 and Freezecast20 noted earlier.

From Fig. 5.3(e), the effect of image sectioning was also prominent, as evidenced by the lamellar spacing of Hierarchical20 being much larger than that of Freezecast20 in one perpendicular direction than the other. This is not surprising since lamellae are randomly aligned in the directions perpendicular to the freezing direction. Lamellar spacing would be the smallest if the image was sectioned perpendicular to lamellar walls and the largest (theoretically infinite) if sectioned parallel to the walls. Therefore, the angle of image sectioning in the directions perpendicular to freezing direction can have a large influence on average lamellar spacing. The Freezecast20 sample has a specific surface area of $0.36 \text{ m}^2/\text{g}$, typical for a macroporous material. The hierarchical sample has a specific surface area of $5.23 \text{ m}^2/\text{g}$, which implies that surface area of the conformal mesoporous coating is $25.78 \pm 2.60 \text{ m}^2/\text{g}$, as calculated from the weight and surface area difference between Hierarchical20 and Freezecast20 samples. By depositing the porous coating on the pore walls, the coating provides at least 70 times more surface area than the freeze-cast scaffold. An even higher surface area could possibly be achieved by infiltrating a different BCP that provides a higher surface area.

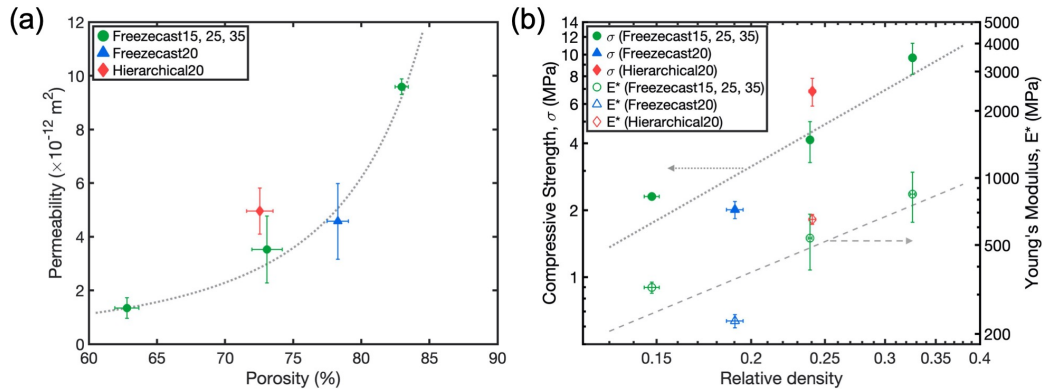


Figure 5.4: (a) Permeability as a function of open porosity and (b) compressive strength and Young's modulus as a function of relative density of all Freezecast and Hierarchical20 samples. Error bars represent ± 1 standard deviation. Dotted lines and the dashed line are linear regressions on log-log plots of baseline materials, included to guide the reader.

Fig. 5.4(a) shows permeability constants for all Freezecast samples compared to Hierarchical20. As noted earlier, the porosity decreased with infiltration. According to the baseline, a decrease in porosity should be accompanied by a decrease in permeability. However, permeability of Hierarchical20 was nearly the same as that of Freezecast20. One likely explanation for this unexpected behavior is the presence of enlarged lamellar spacings (3.4% by volume) as shown in both Fig. 5.1(f) and Fig. 5.3(e) which allowed more flow, and hence produced a higher permeability than anticipated with the lower porosity.

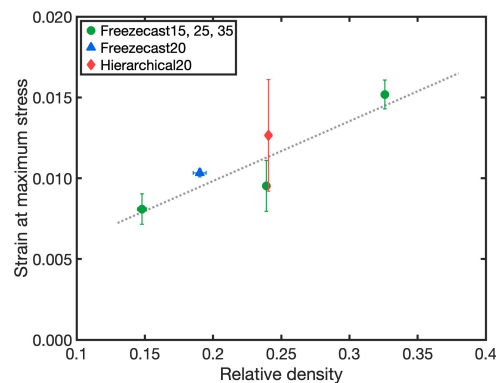


Figure 5.5: Strain at maximum stress as a function of relative density of all Freezecast and Hierarchical20 samples. Error bars represent ± 1 standard deviation. Dotted lines is a linear regressions of baseline materials, included to guide the reader.

The compressive strength and Young's modulus for all Freezecast and Hierarchical20 samples are reported in Fig. 5.4(b) and follow the generally observed trend of increasing strength and Young's modulus with relative density [141]. Gibson and Ashby [65] showed that compressive strength and Young's modulus are power-law functions of relative density. In Fig. 5.4(b), Hierarchical20 is also shown to be within a reasonable range of the same power-law relation established with Freezecast samples and other studies of freeze-cast polysiloxanes-derived ceramics [125]. Likewise, the strain at maximum stress for the Hierarchical20 (Fig. 5.5) is also consistent with that of the Freezecast samples, accounting for density. This agreement demonstrates that the incorporation of a highly-porous conformal coating does not diminish the expected strengthening with increased density.

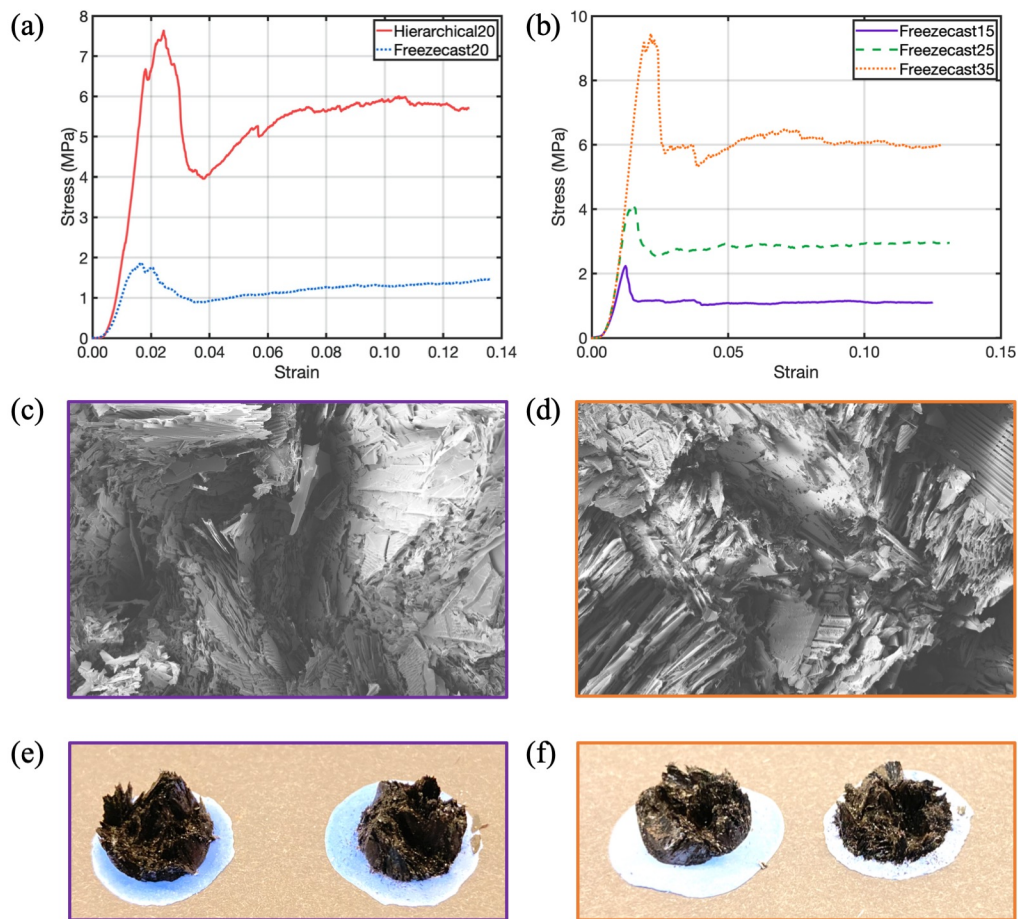


Figure 5.6: Representative stress–strain curves of (a) Freezecast20 and Hierarchical20 and (b) Freezecast15, Freezecast25, and Freezecast35. SEM micrographs of fracture surfaces of (c) Freezecast15 and (d) Freezecast35. Examples of fractured samples after compression of (e) Freezecast15 and (f) Freezecast35.

As previously mentioned in Sections 4.3.4 and 3.3.1.2, brittle lamellar structures with insufficient interlamellar bridges, such as freeze-cast structures from DMC, often fail in shear [111]. In a typical stress-strain curve representing shear failure of a porous lamellar solid, the stress increases linearly to a peak value at which point the interlamellar bridges fracture and lamellar walls slip over one another, resulting in a substantial load drop at strains <3%. The peak is followed by a low stress plateau during crack propagation, and finally a gradual stress increase due to the densification of the fractured pore structure [65]. Fig. 5.6(a) shows that both Freezecast20 and Hierarchical20 failed in shear failure, exhibiting the signature stress-strain response

of porous brittle materials. The stress-strain curves, independently of SEM images, also demonstrate that the introduction of a mesoporous coating has not noticeably changed the structure of the underlying freeze-cast scaffold.

Interestingly, while Freezecast15, Freezecast25, Freezecast35 have fairly different porosities (83.1-63.0%) and mechanical strengths (2.30-9.68 MPa), they all failed in shear as evidenced by similar shapes of the stress-strain curves. Additional evidence of the shear failure was observed in macroscopic (Fig. 5.6(c, d)) and microscopic (Fig. 5.6(e, f)) fracture surfaces of uniaxial compression tests. Largely through-thickness intact lamellar walls can be observed in fracture samples of Freezecast15 (Fig. 5.6(c)) and Freezecast35 (Fig. 5.6(d)), indicating that the fracture occurred along lamellar walls, along directions of maximum shear. Fracture surfaces of Freezecast15 (Fig. 5.6(c)) and Freezecast35 (Fig. 5.6(d)) show clean cleavage fracture between lamellar walls with few connections between one lamella and another. Lamellae are able to slide over one another easily without breaking lamellar planes. These findings imply that the pore structures of various porosities and their resultant fracture behavior are similar despite having higher solids loading. Denser freeze-cast pore structures do not automatically create noticeably more interlamellar bridges than those with lower relative densities.

5.4 Conclusions and Implications

In summary, a bulk hierarchical ceramic structure was achieved via solution-based freeze casting coupled with a conformal coating using self-assembled block copolymers. The hierarchical material demonstrates an increase in surface area and mechanical properties, while retaining permeability of the macroporous structure as a result of the introduction of pore hierarchy. These changes in properties are expected to produce more robust filters, reactors, and electrodes with higher throughput (permeability), higher reaction rate (surface area), and prolonged product life (compressive strength). Furthermore, this study opens new avenues to independently optimize two pore length scales for creating hierarchical pores. In the freeze-casting stage, pore alignment and permeability can be controlled by adopting a grain selector [127] or by thermal gradient control [109].

For solution-based freeze casting using preceramic polymers, compositions are restricted to silicon-based materials. However, provided good interfacial adhesion exists, suspension freeze casting can potentially provide porous templates so that a wide range of starting materials with bio-compatibility [102], ionic conductivity

[110], or shape-memory effect [196, 202] can be used. Conformal coatings with self-assembled block copolymers are also tailorable. Pore size, connectivity and surface area can all be adjusted by changing either the relative block size in the BCP or homopolymer concentrations [83, 90].

SUMMARY, CONCLUSIONS, AND FUTURE WORK

6.1 Summary and Conclusions

This work has successfully supplied strategies for creating optimized pore structures that provide sufficient strength, permeability, and surface area under the framework of freeze-casting based upon composite material principles of both particle reinforcement and hierarchical design.

To optimize the mechanical and transport properties, we first chose a highly permeable lamellar structure of SiOC ceramic fabricated from freeze casting with DMC and polysiloxane. This high-permeability pore structure was reinforced by SiC whiskers and CNTs. The two fillers provided two different reinforcement mechanisms of pore structures—structural reinforcement across pore walls discussed in Chapter 3 and material reinforcement within the pore walls explored in Chapter 4.

Lamellar structures often fail in shear at low stresses. Therefore, in Chapter 3, we utilized the phenomenon of particle engulfment to create SiC whisker interlamellar bridges, which prevented shear failure and increased the compressive strength 3-fold with 30 vol.% whiskers. Whiskers were present both across and inside pore walls, providing reinforcements to the walls and the overall structure. The permeability decreased slightly but maintained in the range of 10^{-12} m² as the porosity of the composites decreased.

In addition, we proposed a new model to remedy the deficiency of current engulfment theories outlined in Section 3.1. The proposed model accounts for two new variables: the intersecting angle between a freezing dendrite and a whisker, and the offset between the center of a whisker and that of the nearest dendrite. These were found to be necessary due to the geometry of high-aspect ratio particles and non-planar freezing fronts. We have implemented a simulation based on the proposed model and a 2D freezing setup to observe solidification *in situ*. The engulfed whisker fraction from the freeze-cast samples was in reasonable agreement with the simulated values. The critical freezing front velocity from the 2D freezing setup agreed with the calculated values from the model. The simulation also reproduced the whisker alignment and the partial engulfment observed in the experiments and showed higher probabilities of engulfment with higher freezing front velocities and longer whiskers, consistent

with previous engulfment models.

We also explored another route as an alternative reinforcing strategy in Chapter 4 for situations where it might be crucial to maintain the original pore structure. CNTs were used as reinforcement fillers and were pushed aside by the freezing front to pore walls due to their small size. The compressive strength increased by 118% with 4.3 wt.% CNTs, likely a result from the 74% increase in pore wall toughness. The pore structure remained similar for low CNT concentration composites (1.3 and 4.3 wt.%). However, CNT agglomerates formed and were engulfed by the freezing front creating interwall bridges as the concentration increased to 8.2 wt.%. The shear failure was prevented by the interwall bridges as in the case of SiC whisker discussed in Chapter 3. Additionally, CNTs were able to change the conductivity by 10 orders of magnitude with the addition of 8.2 wt.% of the reinforcement.

As demonstrated, pore structure can be tuned by the methods outlined in Chapters 3 and 4 to achieve desired mechanical and transport properties. In contrast, Chapter 5 outlined the method to increase the surface area of the pore structure by depositing a high-surface-area conformal coating via self-assembly of BCP. The hierarchical structure displayed bimodal pore size distribution with pores around 30 nm from BCP self-assembly and 20 μm from freeze casting. The surface area of the coating is 70 times higher than that of the scaffold. The introduction of pore hierarchy also resulted in an increase in mechanical properties, while retaining permeability of the macroporous structure.

All the pore structures discussed in this thesis are lamellar structures made from freeze casting with DMC as the solvent, and as such, can be readily compared. It is useful in summary to examine how different composite strategies affect the fracture behavior and the mechanical and transport properties of the various porous solids.

The compressive strength versus relative density of freeze-cast pure SiOC from all three projects—the SiC-reinforced, the CNT-reinforced, and the BCP-hierarchical porous solid—are shown in Fig. 6.1. Pure SiOC from two of the projects, the SiC-reinforced and the BCP-hierarchical projects, are very similar. In fact, a linear regression with $R^2 = 0.9311$, plotted with dotted line, can be determined from these two sets of data. Gibson and Ashby [65] have shown that the compressive strength and relative density follows a power-law relation for brittle porous materials as briefly discussed in Section 3.3.1.2:

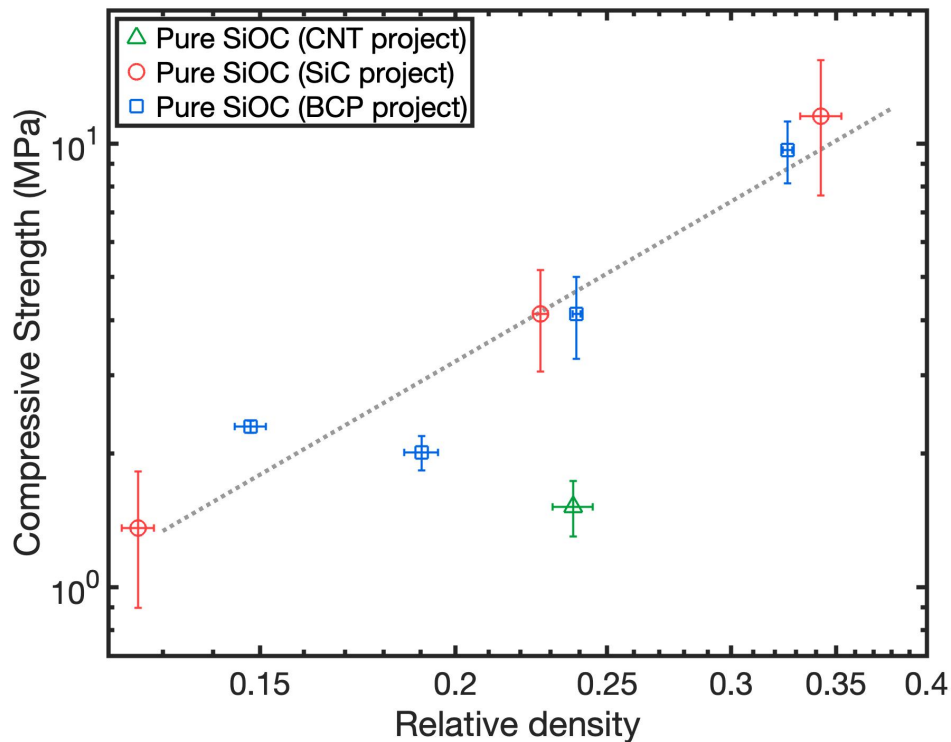


Figure 6.1: Compressive strength as a function of relative density of freeze-cast pure SiOC from the CNT-reinforced, the SiC-reinforced, and the BCP-hierarchical porous solid projects.

$$\frac{\alpha}{\alpha_0} = C \left(\frac{\rho}{\rho_0} \right)^n \quad (6.1)$$

They found n to be 1, $\frac{3}{2}$, and 2 for honeycombs, open-cell, and closed-cell foams, respectively. Seuba et al. [159] observed a contradictory result with $n = 3$ for freeze-cast ceramics that fail in bulking. The scaling factor, n , calculated from these two sets of data in this work is 2.05, similar to that of freeze-cast dendritic structures reported by Naviroj [125] despite having different morphologies. The possible reason for the variation in the scaling factor, n , is that while freeze-cast cellular structures are honeycombs, dendritic or lamellar structures possess a complex geometry that is neither open-cell, close-cell, nor honeycomb-like.

Fig. 6.1 also shows that pure SiOC samples from the CNT-reinforced study have lower strength than those from the other two projects. There are two contributing factors to this result. First, porous SiOC samples from the CNT-reinforced project were frozen with a $-3^\circ/\text{min}$ cooling rate while those from the SiC-reinforced and the

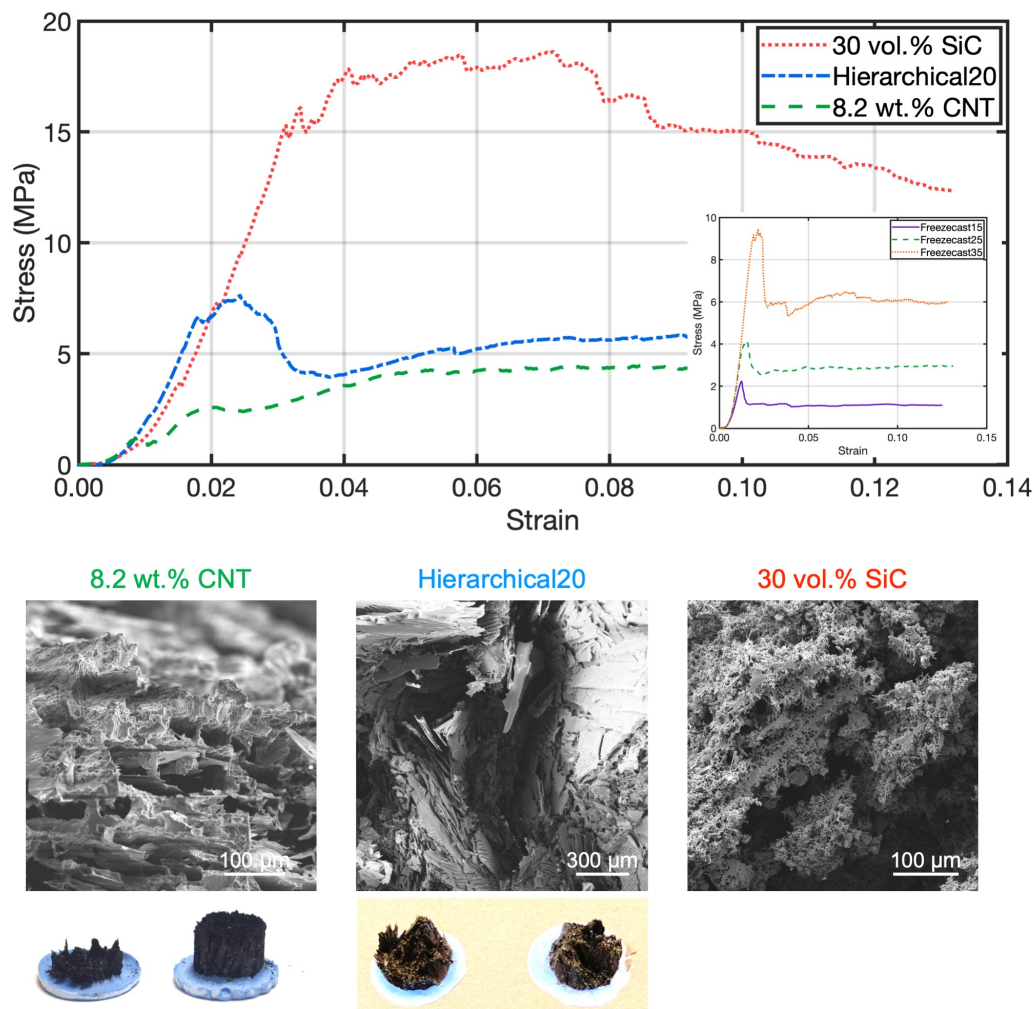


Figure 6.2: Compressive strength vs. permeability constant of CNT-reinforced, SiC whisker-reinforced, and hierarchical composites, and corresponding fracture surfaces and macro-images of fractured samples. The inset includes the stress-strain curves of freeze-cast pure SiOC of various densities from BCP-hierarchical project for reference.

BCP-hierarchical projects were quenched at -35°C and -30°C , respectively. This is expected to result in higher freezing front velocities, finer freeze-cast structures and ultimately higher mechanical strengths [159]. Second, porous SiOC samples from the CNT-reinforced project are taller. For brittle materials, a size effect exists such that samples with larger volumes are more likely to contain a larger flaw, making such samples fail at lower stresses [16, 149, 164].

The stress-strain curves, SEM images of the fracture surfaces, and macro images of fractured samples of CNT-reinforced, SiC whisker-reinforced, and hierarchical

composites are shown in Fig. 6.2. The inset includes the stress-strain curves of freeze-cast pure SiOC of various densities from BCP-hierarchical project for reference. The composite with 30 vol.% SiC whisker has the highest strength followed by Hierarchical20 and the 8.2 wt.% CNT composite, in the same order as their relative density. Two different stress-strain responses are discernible in the figure. Hierarchical composites exhibited the stress-strain behavior of freeze-cast pure SiOC lamellar structures with a linear increase to a peak followed by a lower-stress plateau as previously shown in the inset and Sections 3.3.1.2, 4.3.4, and 5.3.

The shapes of these curves imply that the hierarchical sample failed by shear fracture where it underwent catastrophic failure, as indicated by a large drop in stress. The fracture surface and macroscopic view of the fractured sample of hierarchical composites display large intact lamellae, from which other lamellae slip off after the breaking of few interlamellar connections. This indicates that the introduction of hierarchy to the structure did not change the connectivity of lamellae despite having a higher relative density than those of CNT composites.

In contrast, the stress-strain curves of CNT and SiC composites had no large drops in stress that indicate failure. Instead, a series of micro-fracture events beginning at about 3% strain indicate that the shear failure (manifested as a large drop in stress in a stress-strain curve) was likely prevented by the interlamellar bridges formed by the engulfment of CNT agglomerates or SiC whiskers. The fracture surfaces of CNT and SiC composites both exhibit a broken surface of lamellae with intact interlamellar connections as the fracture propagates through lamellae. These observations demonstrate that the fracture behavior is heavily influenced by the density of interlamellar connections rather than the density of the porous ceramic and that the fracture behavior is independent of relative density or strength.

Finally, Fig. 6.3 compares the compressive strength versus permeability constant of CNT-reinforced, SiC whisker-reinforced, and hierarchical composites with freeze-cast pure SiOC all with lamellar microstructures. Also included is data for pure SiOC, both lamellar and dendritic structures, reported by Naviroj [125]. The figure shows that CNTs and SiC whiskers have successfully reinforced the lamellar structure at little expense of permeability. Interestingly, the hierarchical structure is also in the same range as reinforced composites despite not being reinforced by fillers. As discussed in 5.3, the compressive strength of the hierarchical structure is similar to that of pure SiOC of the same relative density. However, the permeability

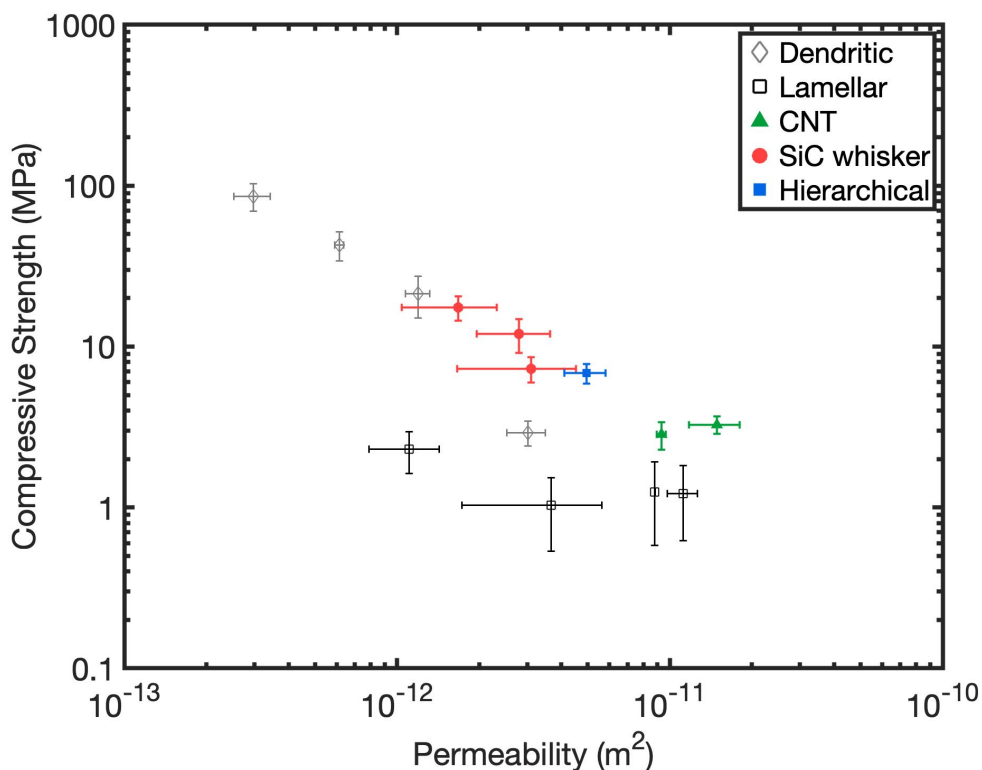


Figure 6.3: Compressive strength vs. permeability constant of CNT-reinforced, SiC whisker-reinforced, and hierarchical composites compared with that of pure SiOC reported by Naviroj [125].

is higher than that of pure SiOC of the same porosity due to the presence of enlarged lamellar spacings. Although unintentional, this demonstrates another strategy to create robust permeable pore structure—instead of reinforcing a highly permeable structure with fillers, increasing the permeability of the structure with lower porosity. These composites have widened the range of mechanical and transport properties and pushed the inversely-related strength and permeability line to the top right corner, where a robust and highly permeable pore structure for filtration and transport lies.

Strategies based upon the design of composites allow us go beyond the current limitation of materials. In this thesis, we have shown that with the provided strategies, robust, highly-permeable and high surface area filtration materials are achievable. The strategies are not limited to the above properties. Other combinations of desirable properties are also possible. For example, robust, bio-compatible CNT-chitosan composites with high surface area are fabricated for bilirubin adsorption [131]. Flexible, thermally stable PVdF-HFP-MgAl₂O₄ with good wettability by electrolytes are

used as battery separator [140]. A lead zirconate titanate-polydimethylsiloxane pressure and shear sensor is self-powered, flexible, and highly active [190] to list a few. Multi-functionality devices can be fabricated with the strategies proposed in this work.

On the scientific side, due to the interplay between each constituent component and processing, the structure, and the resultant properties, the composites are inherently complex. This complexity poses many interesting questions. Particle engulfment discussed in the thesis is an example, where the PCP in suspension affects the shape and the spacing of freezing dendrites, affecting the probability of engulfment for whiskers. The engulfment probability of the whiskers, in turn, affects the mechanical and transport properties of the PDC derived from the said PCP. In this work, we have tackled a few of these questions. However, many are left for the future studies in this burgeoning field of composites via freeze casting.

6.2 Suggestions for Future Work

A stable, well-dispersed CNT suspension is a requirement for CNTs to act as reinforcement fillers that only alter the pore wall chemistry without changing pore structures. As shown in Chapter 4, with higher CNT concentrations, CNT agglomerates form and change the freezing dynamics and subsequently the pore structure. CNT walls can be modified chemically to improve dispersion in a solvent and obtain a stable dispersion in spite of high CNT concentrations. This modification of CNT walls may also improve the adhesion between the matrix and CNTs, further improving its mechanical properties [167]. We have not seen engulfment of any individual CNT. However, Gutiérrez has shown a pore structure with interwall bridges possibly formed via the engulfment of individual CNTs [70].

There are a variety of future directions for particle engulfment theory and experiments. First, the model discussed in Chapter 3 is a simplified, bare-bones model that includes only two major forces, the drag force from the fluid motion and the repulsive force from the surface energy. As discussed in Section 2.1.4, other forces (buoyancy, gravity, osmotic forces, and externally applied forces), factors, such as particle roughness, the Gibbs-Thomson effect, and particle wettability, and particle-particle and multiple-dendrite interactions can be included. With the addition of these parameters, it is likely that an analytical solution, such as that shown in Section 3.3.2.1 would not be possible. Numerical solution of Navier-Stokes equation will have to be attempted instead. The engulfment model could be extended to work with

other high-aspect ratio particles and verified with other freezing casting systems.

On the experimental side, the 2D *in-situ* setup can be adapted to include control of the thermal gradient. The possible minimal distance between a particle and the freezing front, i.e. the gap of the liquid film, has been under debate and is often used as a fitting parameter [6]. This is unlikely to be resolved by adopting a confocal microscope since the gap is on the order of nanometer. However, a confocal microscope can be used to construct 3d images of the dendrite tip shape and the relative location of the center of a dendrite tip and a whisker [43]. Combined with numerical solutions, a confocal microscope may allow us to model the solidification process more accurately.

Chapter 5 shows the introduction of enlarged spacing in the hierarchical structures possibly due to drying pressure of BCP gel. This phenomenon remains the major challenge with thermoreversible gelcasting [162] and other processing methods that utilize the self-assembly of BCP gels. For small-size samples that dry quickly, freeze-drying is able to mitigate the deformation since the solvent stays in the solid state during drying. However, commonly-used solvents for BCP gels, such as 2EH and isopropanol, have low freezing points, which are difficult to maintain over a long period of time required for the drying of larger samples. Alternatively, liquid desiccants have been used to minimize warping by transferring the solvent from the gel body to the desiccant bath [13]. Another logical next step is to construct a device made from hierarchical structures via BCP self-assembly and freeze casting and measure the reaction rate to ascertain if the higher surface area is reflected in the reaction rate or whether the enlarged lamellar spacings diminish the reaction rate.

Last but not least, while compressive strength is often used to characterize the mechanical properties of porous ceramics, burst test for pressure vessels may be more suitable measurement for devices intended for filtration and transport. Maximum pressure before failure of filtration and transport devices should be tested and compared with their compressive strength.

REFERENCES

- [1] Ander Abarrategi, María C. Gutiérrez, Carolina Moreno-Vicente, María J. Hortigüela, Viviana Ramos, José L. López-Lacomba, María L. Ferrer, and Francisco del Monte. Multiwall carbon nanotube scaffolds for tissue engineering purposes. *Biomaterials*, 29(1):94–102, 2008. ISSN 01429612. doi: 10.1016/j.biomaterials.2007.09.021.
- [2] Silvère Akamatsu and Henri Nguyen-Thi. In situ observation of solidification patterns in diffusive conditions. *Acta Materialia*, 108:325–346, 2016. ISSN 13596454. doi: 10.1016/j.actamat.2016.01.024.
- [3] J.-W. An, D.-H. You, and D.-S. Lim. Tribological properties of hot-pressed alumina-CNT composites. *Wear*, 255(1-6):677–681, 2003. ISSN 00431648. doi: 10.1016/S0043-1648(03)00216-3. URL <https://www.sciencedirect.com/science/article/abs/pii/S0043164803002163>.
- [4] Noriaki Arai and Katherine T. Faber. Hierarchical porous ceramics via two-stage freeze casting of preceramic polymers. *Scripta Materialia*, 162:72–76, 2019. ISSN 13596462. doi: 10.1016/j.scriptamat.2018.10.037. URL <https://doi.org/10.1016/j.scriptamat.2018.10.037>.
- [5] Kiyoshi Araki and John W. Halloran. Porous ceramic bodies with interconnected pore channels by a novel freeze casting technique. *Journal of the American Ceramic Society*, 88(5):1108–1114, 2005. ISSN 0002-7820. doi: 10.1111/j.1551-2916.2005.00176.x. URL <http://doi.wiley.com/10.1111/j.1551-2916.2005.00176.x>.
- [6] R. Asthana and S. N. Tewari. The engulfment of foreign particles by a freezing interface. *Journal of Materials Science*, 28:5414–5425, 1993. ISSN 1359-0286. doi: 10.1016/j.cossms.2010.07.001. URL <http://dx.doi.org/10.1016/j.cossms.2010.07.001>.
- [7] C. Atkinson, R. E. Smelser, and J. Sanchez. Combined mode fracture via the cracked Brazilian disk test. *International Journal of Fracture*, 18(4):279–291, 1982. ISSN 03769429. doi: 10.1007/BF00015688. URL <https://link.springer.com/article/10.1007/BF00015688>.
- [8] H. Bai, Y. Chen, B. Delattre, A. P. Tomsia, and R. O. Ritchie. Bioinspired large-scale aligned porous materials assembled with dual temperature gradients. *Nature materials*, 14(1):23–36, 2015. ISSN 1476-1122. doi: 10.1038/nmat4089. URL <http://www.ncbi.nlm.nih.gov/pubmed/25344782>.

- [9] Jinbo Bai and Aïssa Allaoui. Effect of the length and the aggregate size of MWNTs on the improvement efficiency of the mechanical and electrical properties of nanocomposites—experimental investigation. Composites Part A: Applied Science and Manufacturing, 34(8):689–694, 2003. ISSN 1359-835X. doi: 10.1016/S1359-835X(03)00140-4. URL <https://www.sciencedirect.com/science/article/pii/S1359835X03001404>.
- [10] C. Balan and R. Riedel. Rheological investigations of a polymeric precursor for ceramic materials: Experiments and theoretical modeling. Journal of Optoelectronics and Advanced Materials, 8(2):561–567, 2006. ISSN 14544164.
- [11] Cs. Balázsi, Z. Kónya, F. Wéber, L. P. Biró, and P. Arató. Preparation and characterization of carbon nanotube reinforced silicon nitride composites. Materials Science and Engineering C, 23(6-8):1133–1137, 2003. ISSN 09284931. doi: 10.1016/j.msec.2003.09.085.
- [12] I. Balberg, C. H. Anderson, S. Alexander, and N. Wagner. Excluded volume and its relation to the onset of percolation. Physical Review B, 30(7):3933–3943, 1984. doi: 10.1145/634067.634269.
- [13] Abolfazl Barati, Mehrdad Kokabi, and Mohammad Hossein Navid Famili. Drying of gelcast ceramic parts via the liquid desiccant method. Journal of the European Ceramic Society, 23(13):2265–2272, 2003. ISSN 09552219. doi: 10.1016/S0955-2219(03)00045-1.
- [14] A. Barbieri and J. S. Langer. Predictions of dendritic growth rates in the linearized solvability theory. Physical Review A, 39(10):5314–5325, 1989. ISSN 10502947. doi: 10.1103/PhysRevA.39.5314.
- [15] Wolfgang Bauhofer and Josef Z. Kovacs. A review and analysis of electrical percolation in carbon nanotube polymer composites. Composites Science and Technology, 69(10):1486–1498, 2009. ISSN 02663538. doi: 10.1016/j.compscitech.2008.06.018. URL <https://www.sciencedirect.com/science/article/pii/S026635380800239X>.
- [16] Zdeněk P. Bažant and Mohammad T. Kazemi. Size effect in fracture of ceramics and its use to determine fracture energy and effective process zone length. Journal of the American Ceramic Society, 73(7):1841–1853, 1990. ISSN 15512916. doi: 10.1111/j.1151-2916.1990.tb05233.x.
- [17] Martine Ben Amar and Efim Brener. Theory of pattern selection in three-dimensional nonaxisymmetric dendritic growth. Physical Review Letters, 71(4):589–592, 1993. ISSN 00319007. doi: 10.1103/PhysRevLett.71.589.
- [18] Enrico Bernardo, Laura Fiocco, Giulio Parcianello, Enrico Storti, and Paolo Colombo. Advanced ceramics from preceramic polymers modified at the nano-scale: A review. Materials, 7(3):1927–1956, 2014. ISSN 19961944. doi: 10.3390/ma7031927.

- [19] G. F. Bolling and J. Cissé. A theory for the interaction of particles with a solidifying front. *Journal of Crystal Growth*, 10(1):56–66, 1971. ISSN 00220248. doi: 10.1016/0022-0248(71)90046-7.
- [20] Florian Bouville, Eric Maire, and Sylvain Deville. Self-assembly of faceted particles triggered by a moving ice front. *Langmuir*, 30(29):8656–8663, 2014. ISSN 15205827. doi: 10.1021/la404426d.
- [21] John J. Bowen, Lisa M. Rueschhoff, Kara L. Martin, Dayton P. Street, Tulsi A. Patel, Maria J. S. Parvulescu, Nicholas M. Bedford, Hilmar Koerner, Soenke Seifert, and Matthew B. Dickerson. Tailorable micelle morphology in self-assembling block copolymer gels for templating nanoporous ceramics. *Macromolecules*, 53(17):7528–7536, 2020. ISSN 0024-9297. doi: 10.1021/acs.macromol.0c01137. URL <https://dx.doi.org/10.1021/acs.macromol.0c01137>.
- [22] H. Bréquel, J. Parmentier, S. Walter, R. Badheka, G. Trimmel, S. Masse, J. Latournerie, P. Dempsey, C. Turquat, A. Desmartin-Chomel, L. Le Neindre-Prum, U. A. Jayasooriya, D. Hourlier, H. J. Kleebe, G. D. Sorarù, S. Enzo, and F. Babonneau. Systematic structural characterization of the high-temperature behavior of nearly stoichiometric silicon oxycarbide glasses. *Chemistry of Materials*, 16(13):2585–2598, 2004. ISSN 08974756. doi: 10.1021/cm049847a.
- [23] Stephen Brunauer, P H Emmett, and Edward Teller. Adsorption of gases in multimolecular layers. *Journal of the American Chemical Society*, 60(1): 309–319, 1938. ISSN 00027863. doi: citeulike-article-id:4074706\rdoi:10.1021/ja01269a023. URL <http://dx.doi.org/10.1021/ja01269a023>.
- [24] Michael F. Butler. Freeze concentration of solutes at the Ice/solution interface studied by optical interferometry. *Crystal Growth and Design*, 2(6):541–548, 2002. ISSN 15287483. doi: 10.1021/cg025591e.
- [25] Neil S Cameron, Muriel K Corbierre, and Adi Eisenberg. 1998 E.W.R. Steacie award lecture asymmetric amphiphilic block copolymers in solution: A morphological wonderland. *Canadian Journal of Chemistry*, 77(8):1311–1326, 1999. ISSN 0008-4042. doi: 10.1139/v99-141.
- [26] P. Casses and M. A. Azouni-Aidi. A general theoretical approach to the behaviour of foreign particles at advancing solid-liquid interfaces. *Advances in Colloid and Interface Science*, 50(C):103–120, 1994. ISSN 00018686. doi: 10.1016/0001-8686(94)80027-8.
- [27] Adrian V Catalina, Sundeep Mukherjee, and Doru M Stefanescu. A dynamic model for the interaction between a solid particle and an advancing solid / liquid Interface. *Metallurgical and Materials Trans . 31A*, 31:2559–2568, 2000. doi: 10.1007/s11661-000-0200-5.

- [28] Chao-Shi Chen, Ernian Pan, and Bernard Amadei. Fracture mechanics analysis of cracked discs of anisotropic rock using the boundary element method. *International Journal of Rock Mechanics and Mining Sciences*, 35(2):195–218, 1998. ISSN 13651609. doi: 10.1016/S0148-9062(97)00330-6. URL <https://www.sciencedirect.com/science/article/pii/S0148906297003306?via%3Dihub>.
- [29] Hehao Chen, Xiaofeng Wang, Fengdan Xue, Yujuan Huang, Kechao Zhou, and Dou Zhang. 3d printing of SiC ceramic: Direct ink writing with a solution of preceramic polymers. *Journal of the European Ceramic Society*, 38(16):5294–5300, 2018. ISSN 1873619X. doi: 10.1016/j.jeurceramsoc.2018.08.009.
- [30] Yasumasa Chino and David C. Dunand. Directionally freeze-cast titanium foam with aligned, elongated pores. *Acta Materialia*, 56(1):105–113, 2008. ISSN 13596454. doi: 10.1016/j.actamat.2007.09.002.
- [31] Jeong Ho Cho, Jiyoul Lee, Yiyong He, Bongsoo Kim, Timothy P. Lodge, and C. Daniel Frisbie. High-capacitance ion gel gate dielectrics with faster polarization response times for organic thin film transistors. *Advanced Materials*, 20(4):686–690, 2008. ISSN 09359648. doi: 10.1002/adma.200701069. URL <https://onlinelibrary.wiley.com/doi/10.1002/adma.200701069>.
- [32] Cathrine D. Christiansen, Kaspar K. Nielsen, Rajendra K. Bordia, and Rasmus Bjørk. The effect of gelation on statically and dynamically freeze-cast structures. *Journal of the American Ceramic Society*, 102(10):5796–5806, 2019. ISSN 15512916. doi: 10.1111/jace.16500.
- [33] A. J. Clarke, D. Tournet, Y. Song, S. D. Imhoff, P. J. Gibbs, J. W. Gibbs, K. Fezzaa, and A. Karma. Microstructure selection in thin-sample directional solidification of an Al-Cu alloy: In situ X-ray imaging and phase-field simulations. *Acta Materialia*, 129:203–216, 2017. ISSN 13596454. doi: 10.1016/j.actamat.2017.02.047. URL <http://dx.doi.org/10.1016/j.actamat.2017.02.047>.
- [34] Jonathan N. Coleman, Umar Khan, Werner J. Blau, and Yurii K. Gun'ko. Small but strong: A review of the mechanical properties of carbon nanotube-polymer composites. *Carbon*, 44(9):1624–1652, 2006. ISSN 00086223. doi: 10.1016/j.carbon.2006.02.038.
- [35] Paolo Colombo and John R. Hellmann. Ceramic foams from preceramic polymers. *Materials Research Innovations*, 6(5-6):260–272, 2002. ISSN 14328917. doi: 10.1007/s10019-002-0209-z.
- [36] Paolo Colombo, Gabriela Mera, Ralf Riedel, and Gian Domenico Sorarù. Polymer-derived ceramics: 40 Years of research and innovation in advanced

- ceramics. Journal of the American Ceramic Society, 93(7):1805–1837, 2010. ISSN 00027820. doi: 10.1111/j.1551-2916.2010.03876.x.
- [37] Paolo Colombo, Cekdar Vakifahmetoglu, and Stefano Costacurta. Fabrication of ceramic components with hierarchical porosity. Journal of Materials Science, 45(20):5425–5455, 2010. ISSN 00222461. doi: 10.1007/s10853-010-4708-9.
- [38] Jens Cordelair and Peter Greil. Electrical conductivity measurements as a microprobe for structure transitions in polysiloxane derived Si-O-C ceramics. Journal of the European Ceramic Society, 20(12):1947–1957, 2000. ISSN 09552219. doi: 10.1016/S0955-2219(00)00068-6. URL <https://linkinghub.elsevier.com/retrieve/pii/S0955221900000686>.
- [39] Stefano Costacurta, Lisa Biasetto, Eckhard Pippel, Jörg Woltersdorf, and Paolo Colombo. Hierarchical porosity components by infiltration of a ceramic foam. Journal of the American Ceramic Society, 90(7):2172–2177, 2007. ISSN 00027820. doi: 10.1111/j.1551-2916.2007.01658.x.
- [40] Peter Cromme, Michael Scheffler, and Peter Greil. Ceramic tapes from preceramic polymers. Advanced Engineering Materials, 4(11):873–877, 2002. ISSN 14381656. doi: 10.1002/1527-2648(20021105)4:11<873::AID-ADEM873>3.0.CO;2-G. URL [https://doi.org/10.1002/1527-2648\(20021105\)4:11%7D3C873::AID-ADEM873%7D3E3.0.CO;2-G](https://doi.org/10.1002/1527-2648(20021105)4:11%7D3C873::AID-ADEM873%7D3E3.0.CO;2-G).
- [41] D. J. Tritton. Experiments on the flow past a circular cylinder at low Reynolds numbers. Journal of Fluid Mechanics, 6(4):547–567, 1959. doi: 10.1017/S0022112059000829. URL <https://www.cambridge.org/core/journals/journal-of-fluid-mechanics/article/experiments-on-the-flow-past-a-circular-cylinder-at-low-reynolds-numbers/0386A4A3A98750248AEB772532863BB6>.
- [42] L. G. J. de Haart. Deposition and electrical properties of thin porous ceramic electrode layers for solid oxide fuel cell application. Journal of The Electrochemical Society, 138(7):1970, 1991. ISSN 00134651. doi: 10.1149/1.2085910.
- [43] Dmytro Dedovets, Cécile Monteux, and Sylvain Deville. A temperature-controlled stage for laser scanning confocal microscopy and case studies in materials science. Ultramicroscopy, 195:1–11, 2018. ISSN 18792723. doi: 10.1016/j.ultramic.2018.08.009.
- [44] Robert T. DeHoff and Frederick N. Rhines. Quantitative microscopy. McGraw-Hill, New York, 1968. ISBN 978-0070162198.
- [45] Jean François Despois and Andreas Mortensen. Permeability of open-pore microcellular materials. Acta Materialia, 53(5):1381–1388, 2005. ISSN 13596454. doi: 10.1016/j.actamat.2004.11.031.

- [46] Sylvain Deville. Freeze-casting of porous ceramics: A review of current achievements and issues. *Advanced Engineering Materials*, 10(3):155–169, 2008. ISSN 14381656. doi: 10.1002/adem.200700270.
- [47] Sylvain Deville. Freeze-casting of porous biomaterials: Structure, properties and opportunities. *Materials*, 3(3):1913–1927, 2010. ISSN 19961944. doi: 10.3390/ma3031913.
- [48] Sylvain Deville. Ice-templating, freeze casting: Beyond materials processing. *Journal of Materials Research*, 28(17):2202–2219, 2013. ISSN 0884-2914. doi: 10.1557/jmr.2013.105. URL http://www.journals.cambridge.org/abstract/{_}S0884291413001052.
- [49] Sylvain Deville, Eduardo Saiz, and Antoni P. Tomsia. Ice-templated porous alumina structures. *Acta Materialia*, 55(6):1965–1974, 2007. ISSN 13596454. doi: 10.1016/j.actamat.2006.11.003.
- [50] Michael S Ding. Liquid-solid phase equilibria and thermodynamic modeling for binary organic carbonates. *Journal of Chemical & Engineering Data*, 49(2):276–282, 2004. doi: 10.1021/je034134e. URL <https://pubs.acs.org/doi/full/10.1021/je034134e>.
- [51] Peter L. Drzal and Kenneth R. Shull. Origins of mechanical strength and elasticity in thermally reversible, acrylic triblock copolymer gels. *Macromolecules*, 36(6):2000–2008, 2003. ISSN 00249297. doi: 10.1021/ma021255v. URL <https://pubs.acs.org/doi/full/10.1021/ma021255v>.
- [52] B. Dutta and M. K. Surappa. Directional dendritic solidification of a composite slurry: Part II. Particle distribution. *Metallurgical and Materials Transactions A*, 29(4):1329–1339, 1998. ISSN 1073-5623. doi: 10.1007/s11661-998-0259-y. URL <http://link.springer.com/10.1007/s11661-998-0259-y>.
- [53] B. Dutta and M. K. Surappa. Directional dendritic solidification of a composite slurry: Part I. Dendrite morphology. *Metallurgical and Materials Transactions A: Physical Metallurgy and Materials Science*, 29(4):1319–1327, 1998. ISSN 10735623. doi: 10.1007/s11661-998-0258-z.
- [54] Z. C. Eckel, C. Zhou, J. H. Martin, A. J. Jacobsen, W. B. Carter, and T. A. Schaedler. Additive manufacturing of polymer-derived ceramics. *Science*, 351(6268):58–62, 2016. ISSN 0036-8075. doi: 10.1126/science.aad2688. URL <http://www.sciencemag.org/cgi/doi/10.1126/science.aad2688>.
- [55] Bahman Elyassi, Muhammad Sahimi, and Theodore T. Tsotsis. A novel sacrificial interlayer-based method for the preparation of silicon carbide membranes. *Journal of Membrane Science*, 316(1-2):73–79, 2008. ISSN

03767388. doi: 10.1016/j.memsci.2007.09.044. URL <https://www.sciencedirect.com/science/article/pii/S0376738807006795>.

- [56] Kendra A. Erk, David C. Dunand, and Kenneth R. Shull. Titanium with controllable pore fractions by thermoreversible gelcasting of TiH₂. *Acta Materialia*, 56(18):5147–5157, 2008. ISSN 13596454. doi: 10.1016/j.actamat.2008.06.035.
- [57] Claudio Ferraro, Esther Garcia-Tuñon, Victoria G. Rocha, Suelen Barg, Maria Dolores Fariñas, Tomas E. Gomez Alvarez-Arenas, Giorgio Sernicola, Finn Giuliani, and Eduardo Saiz. Light and Strong SiC Networks. *Advanced Functional Materials*, 26(10):1636–1645, 2016. ISSN 16163028. doi: 10.1002/adfm.201504051.
- [58] Qiang Fu, Mohamed N. Rahaman, Fatih Dogan, and B. Sonny Bal. Freeze-cast hydroxyapatite scaffolds for bone tissue engineering applications. *Biomedical Materials*, 3(2):025005, 2008. ISSN 17486041. doi: 10.1088/1748-6041/3/2/025005.
- [59] Qiang Fu, Mohamed N. Rahaman, Fatih Dogan, and B. Sonny Bal. Freeze casting of porous hydroxyapatite scaffolds. II. Sintering, microstructure, and mechanical behavior. *Journal of Biomedical Materials Research - Part B Applied Biomaterials*, 86(2):514–522, 2008. doi: 10.1002/jbm.b.31051. URL <http://doi.wiley.com/10.1002/jbm.b.31051>.
- [60] Shao Yun Fu and Bernd Lauke. Effects of fiber length and fiber orientation distributions on the tensile strength of short-fiber-reinforced polymers. *Composites Science and Technology*, 56(10):1179–1190, 1996. ISSN 02663538. doi: 10.1016/S0266-3538(96)00072-3.
- [61] Manabu Fukushima, Tatsuki Ohji, Hideki Hyuga, Chika Matsunaga, and Yu Ichi Yoshizawa. Effect of gelatin gel strength on microstructures and mechanical properties of cellular ceramics created by gelation freezing route. *Journal of Materials Research*, 32(17):3286–3293, 2017. ISSN 20445326. doi: 10.1557/jmr.2017.94.
- [62] J. W. Garvin and H. S. Udaykumar. Drag on a particle being pushed by a solidification front and its dependence on thermal conductivities. *Journal of Crystal Growth*, 267(3-4):724–737, 2004. doi: 10.1016/j.jcrysgro.2004.03.074.
- [63] Dipankar Ghosh, Mahesh Banda, Hyungsuk Kang, and Nikhil Dhavale. Platelets-induced stiffening and strengthening of ice-templated highly porous alumina scaffolds. *Scripta Materialia*, 125:29–33, 2016. ISSN 13596462. doi: 10.1016/j.scriptamat.2016.07.030. URL <http://dx.doi.org/10.1016/j.scriptamat.2016.07.030>.

- [64] Dipankar Ghosh, Mahesh Banda, Sashanka Akurati, Hyungsuk Kang, and Vivian O. Fakhariadeh. On the brittle fracture characteristics of lamella walls of ice-templated sintered alumina scaffolds and effects of platelets. *Scripta Materialia*, 138:139–144, 2017. ISSN 13596462. doi: 10.1016/j.scriptamat.2017.05.049. URL <http://dx.doi.org/10.1016/j.scriptamat.2017.05.049>.
- [65] Lorna J. Gibson and Michael F. Ashby. *Cellular Solids*. Cambridge University Press, Cambridge, 1997. ISBN 9781139878326. doi: 10.1017/CBO9781139878326. URL <http://ebooks.cambridge.org/ref/id/CBO9781139878326>.
- [66] R. R. Gilpin. A model of the "liquid-like" layer between ice and a substrate with applications to wire regelation and particle migration. *Journal of Colloid And Interface Science*, 68(2):235–251, 1979. ISSN 00219797. doi: 10.1016/0021-9797(79)90277-7.
- [67] Martin Eden Glicksman. *Principles of solidification: An introduction to modern casting and crystal growth concepts*. Springer-Verlag New York, 2011. ISBN 978-1-4419-7343-6. doi: 10.1007/978-1-4419-7344-3.
- [68] P. Greil. Polymer derived engineering ceramics. *Advanced Engineering Materials*, 2(6):339–348, 2000. ISSN 1438-1656. doi: 10.1002/1527-2648(200006)2:6<339::AID-ADEM339>3.0.CO;2-K. URL [http://doi.wiley.com/10.1002/1527-2648\(200006\)2:6{339::AID-ADEM339}3E3.0.CO;2-K](http://doi.wiley.com/10.1002/1527-2648(200006)2:6{339::AID-ADEM339}3E3.0.CO;2-K).
- [69] Peter Greil. Near net shape manufacturing of polymer derived ceramics. *Journal of the European Ceramic Society*, 18(13):1905–1914, 1998. doi: 10.1016/S0955-2219(98)00129-0.
- [70] María C. Gutiérrez, María J. Hortigüela, J. Manuel Amarilla, Ricardo Jiménez, María L. Ferrer, and Francisco Del Monte. Macroporous 3D architectures of self-assembled MWCNT surface decorated with pt nanoparticles as anodes for a direct methanol fuel cell. *Journal of Physical Chemistry C*, 111(15):5557–5560, 2007. ISSN 19327447. doi: 10.1021/jp0714365.
- [71] Emily C. Hammel, Osayande Lord Rufus Ighodaro, and Okenwa I. Okoli. Processing and properties of advanced porous ceramics: An application based review. *Ceramics International*, 40(10):15351–15370, 2014. ISSN 02728842. doi: 10.1016/j.ceramint.2014.06.095. URL <http://www.sciencedirect.com/science/article/pii/S0272884214009900>.
- [72] Rahul Harshe, Corneliu Balan, and Ralf Riedel. Amorphous Si(Al)OC ceramic from polysiloxanes: Bulk ceramic processing, crystallization behavior and applications. *Journal of the European Ceramic Society*, 24(12):3471–3482, 2004. ISSN 09552219. doi: 10.1016/j.jeurceramsoc.2003.10.016.

- [73] Ziming He, Jing Liu, Yan Qiao, Chang Ming Li, and Timothy Thatt Yang Tan. Architecture engineering of hierarchically porous chitosan/vacuum-stripped graphene scaffold as bioanode for high performance microbial fuel cell. Nano Letters, 12(9):4738–4741, 2012. ISSN 15306984. doi: 10.1021/nl302175j.
- [74] Amanda L. Higginbotham, Pdraig G. Moloney, Michael C. Waid, Juan G. Duque, Carter Kittrell, Howard K. Schmidt, Jason J. Stephenson, Sivaram Arepalli, Leonard L. Yowell, and James M. Tour. Carbon nanotube composite curing through absorption of microwave radiation. Composites Science and Technology, 68(15-16):3087–3092, 2008. ISSN 02663538. doi: 10.1016/j.compscitech.2008.07.004. URL <https://www.sciencedirect.com/science/article/pii/S0266353808002595>.
- [75] Dachamir Hotza, Rafael K. Nishihora, Ricardo A. F. Machado, Pierre-Marie Geffroy, Thierry Chartier, and Samuel Bernard. Tape casting of preceramic polymers toward advanced ceramics: A review. International Journal of Ceramic Engineering & Science, 1(1):21–41, 2019. doi: 10.1002/ces2.10009. URL <https://onlinelibrary.wiley.com/doi/abs/10.1002/ces2.10009>.
- [76] Nicola Huesing, Christina Raab, Viktoria Torma, Anna Roig, and Herwig Peterlik. Periodically mesostructured silica monoliths from diol-modified silanes. Chemistry of Materials, 15(14):2690–2692, 2003. ISSN 08974756. doi: 10.1021/cm034036c.
- [77] J. D. Hunt and S. Z. Lu. Numerical modeling of cellular/dendritic array growth: Spacing and structure predictions. Metallurgical and Materials Transactions A: Physical Metallurgy and Materials Science, 27(3):611–623, 1996. ISSN 10735623. doi: 10.1007/BF02648950. URL <https://link.springer.com/article/10.1007/BF02648950>.
- [78] M. D M Innocentini, R. K. Faleiros, R. Pisani, I. Thijs, J. Luyten, and S. Mullens. Permeability of porous gelcast scaffolds for bone tissue engineering. Journal of Porous Materials, 17(5):615–627, 2010. ISSN 13802224. doi: 10.1007/s10934-009-9331-2.
- [79] R. J. Iwanowski, K. Fronc, W. Paszkowicz, and M. Heinonen. XPS and XRD study of crystalline 3C-SiC grown by sublimation method. Journal of Alloys and Compounds, 286(1-2):143–147, 1999. ISSN 09258388. doi: 10.1016/S0925-8388(98)00994-3.
- [80] K. A. Jackson and J. D. Hunt. Transparent compounds that freeze like metals. Acta Metallurgica, 13(11):1212–1215, 1965. ISSN 00016160. doi: 10.1016/0001-6160(65)90061-1.
- [81] Kenneth A. Jackson. Constitutional supercooling surface roughening. Journal of Crystal Growth, 264(4):519–529, 2004. ISSN 00220248. doi: 10.1016/j.jcrysgro.2003.12.074.

- [82] Samson A Jenekhe and X Linda Chen. Self-assembled aggregates of rod-coil block copolymers and their solubilization and encapsulation of Fullerenes. *Science*, 279(5358):1903–1907, 1998. ISSN 00368075. doi: 10.1126/science.279.5358.1903.
- [83] Unyong Jeong, Du Yeol Ryu, Jin Kon Kim, Dong Ha Kim, Xiadong Wu, and Thomas P. Russell. Precise control of nanopore size in thin film using mixtures of asymmetric block copolymer and homopolymer. *Macromolecules*, 36(26): 10126–10129, 2003. ISSN 00249297. doi: 10.1021/ma034976i.
- [84] Moncy V. Jose, Derrick Dean, James Tyner, Gary Price, and Elijah Nyairo. Polypropylene/carbon nanotube nanocomposite fibers: Process–morphology–property relationships. *Journal of Applied Polymer Science*, 103(6):3844–3850, 2007. ISSN 00218995. doi: 10.1002/app.25475. URL <http://doi.wiley.com/10.1002/app.25475>.
- [85] Yuji Katsuda, Peter Gerstel, Janakiraman Narayanan, Joachim Bill, and Fritz Aldinger. Reinforcement of precursor-derived Si-C-N ceramics with carbon nanotubes. *Journal of the European Ceramic Society*, 26(15):3399–3405, 2006. ISSN 09552219. doi: 10.1016/j.jeurceramsoc.2005.10.014.
- [86] Sarabjeet Kaur, Ralf Riedel, and Emanuel Ionescu. Pressureless fabrication of dense monolithic SiC ceramics from a polycarbosilane. *Journal of the European Ceramic Society*, 34(15):3571–3578, 2014. ISSN 09552219. doi: 10.1016/j.jeurceramsoc.2014.05.002. URL <http://dx.doi.org/10.1016/j.jeurceramsoc.2014.05.002>.
- [87] Byoung Soo Kim and Jonghwi Lee. Pore size reduction in directional crystallization processing of porous polymeric membranes. *Journal of Nanoscience and Nanotechnology*, 13(3):2276–2283, 2013. ISSN 15334880. doi: 10.1166/jnn.2013.7096.
- [88] Dae Jun Kim, Hyun Joong Kim, and Goan Hee Yoon. Effect of substrate and tackifier on peel strength of SIS (styrene-isoprene-styrene)-based HMPSAs. *International Journal of Adhesion and Adhesives*, 25(4):288–295, 2005. ISSN 01437496. doi: 10.1016/j.ijadhadh.2004.10.001.
- [89] J. K. Kim and P. K. Rohatgi. An analytical solution of the critical interface velocity for the encapsulating of insoluble particles by a moving solid/liquid interface. *Metallurgical and Materials Transactions A: Physical Metallurgy and Materials Science*, 29(1):351–358, 1998. ISSN 10735623. doi: 10.1007/s11661-998-0186-y.
- [90] H. Kishi, Y. Kunimitsu, Y. Nakashima, T. Abe, J. Imade, S. Oshita, Y. Morishita, and M. Asada. Control of nanostructures generated in epoxy matrices blended with PMMA-b-PnBA-b-PMMA triblock copolymers. *Express Polymer Letters*, 9(1):23–35, 2015. ISSN 1788618X. doi: 10.3144/expresspolymlett.2015.4.

- [91] Ryo Kobayashi. Modeling and numerical simulations of dendritic crystal growth. *Physica D: Nonlinear Phenomena*, 63(3-4):410–423, 1993. doi: 10.1016/0167-2789(93)90120-P.
- [92] Young-Hag Koh, Eun-Jung Lee, Byung-Ho Yoon, Ju-Ha Song, Hyoun-Ee Kim, and Hae-Won Kim. Effect of polystyrene addition on freeze casting of ceramic/camphene slurry for ultra-high porosity ceramics with aligned pore channels. *Journal of the American Ceramic Society*, 89(12):3646–3653, 2006. doi: 10.1111/j.1551-2916.2006.01311.x. URL <https://ceramics.onlinelibrary.wiley.com/doi/pdf/10.1111/j.1551-2916.2006.01311.x>.
- [93] Sindo Kou. *Welding Metallurgy*. Wiley, Hoboken, NJ, USA, 2002. ISBN 0471434914. doi: 10.1002/0471434027. URL <http://doi.wiley.com/10.1002/0471434027>.
- [94] Edwin Kroke, Ya Li Li, Christoph Konetschny, Emmanuel Lecomte, Claudia Fasel, and Ralf Riedel. Silazane derived ceramics and related materials. *Materials Science and Engineering R: Reports*, 26(4):97–199, 2000. ISSN 0927796X. doi: 10.1016/s0927-796x(00)00008-5.
- [95] B. V. Manoj Kumar and Young-Wook Kim. Processing of polysiloxane-derived porous ceramics: A review, 2010. ISSN 14686996. URL <https://www.tandfonline.com/doi/abs/10.1088/1468-6996/11/4/044303>.
- [96] Parveen Kumar and Vadim V. Guliyants. Periodic mesoporous organic-inorganic hybrid materials: Applications in membrane separations and adsorption. *Microporous and Mesoporous Materials*, 132(1-2):1–14, 2010. ISSN 13871811. doi: 10.1016/j.micromeso.2010.02.007. URL <http://dx.doi.org/10.1016/j.micromeso.2010.02.007>.
- [97] C. T. Kuo and K. T. Faber. Permeable carbon nanotube-reinforced silicon oxycarbide via freeze casting with enhanced mechanical stability. *Journal of the European Ceramic Society*, 40(6):2470–2479, 2020. ISSN 1873619X. doi: 10.1016/j.jeurceramsoc.2019.12.059. URL <https://doi.org/10.1016/j.jeurceramsoc.2019.12.059>.
- [98] W Kurz and D J Fisher. Dendrite growth at the limit of stability: tip radius and spacing. *Acta Metallurgica*, 29(1):11–20, 1981. URL [https://doi.org/10.1016/0001-6160\(81\)90082-1](https://doi.org/10.1016/0001-6160(81)90082-1).
- [99] W Kurz and D J Fisher. *Fundamentals of solidification*. Trans Tech Publications, Switzerland, 1998. ISBN 9783035732399. URL <http://caltech.tind.io/record/635426>.
- [100] Natalie M. Larson and Frank W. Zok. In-situ 3D visualization of composite microstructure during polymer-to-ceramic conversion. *Acta Materialia*, 144: 579–589, 2018. ISSN 13596454. doi: 10.1016/j.actamat.2017.10.054. URL <https://doi.org/10.1016/j.actamat.2017.10.054>.

- [101] L. Gary Leal. Advanced transport phenomena: Fluid mechanics and convective transport processes. Cambridge University Press, 2007. ISBN 9780511800245. doi: 10.1017/CBO9780511800245. URL <https://www.cambridge.org/core/books/advanced-transport-phenomena/9F2A633638780413DA73C6CB70A1D341>.
- [102] Hyun Lee, Tae Sik Jang, Juha Song, Hyoun Ee Kim, and Hyun Do Jung. The production of porous hydroxyapatite scaffolds with graded porosity by sequential freeze-casting. Materials, 10(4):1–12, 2017. ISSN 19961944. doi: 10.3390/ma10040367.
- [103] Min Kyung Lee and Jonghwi Lee. Mimicking permafrost formation for the preparation of porous polymer membranes. Polymer, 74:176–181, 2015. ISSN 00323861. doi: 10.1016/j.polymer.2015.08.014. URL <http://dx.doi.org/10.1016/j.polymer.2015.08.014>.
- [104] Robert Lemlich. A theory for the limiting conductivity of polyhedral foam at low density. Journal of Colloid and Interface Science, 64(1):107–110, 1978. ISSN 0021-9797. doi: 10.1016/0021-9797(78)90339-9. URL <https://www.sciencedirect.com/science/article/pii/S0021979778903399>.
- [105] Jennifer A. Lewis. Colloidal processing of ceramics. Journal of the American Ceramic Society, 2009. ISSN 17436753. doi: 10.1179/1743676111Y.0000000075.
- [106] Jing Li, Peng Cheng Ma, Wing Sze Chow, Chi Kai To, Ben Zhong Tang, and Jang Kyo Kim. Correlations between percolation threshold, dispersion state, and aspect ratio of carbon nanotubes. Advanced Functional Materials, 17(16):3207–3215, 2007. ISSN 1616301X. doi: 10.1002/adfm.200700065.
- [107] Z F Li, G H Luo, W P Zhou, F Wei, R Xiang, and Y P Liu. The quantitative characterization of the concentration and dispersion of multi-walled carbon nanotubes in suspension by spectrophotometry. Nanotechnology, 17(15):3692–3698, 2006. ISSN 0957-4484. doi: 10.1088/0957-4484/17/15/012. URL <http://stacks.iop.org/0957-4484/17/i=15/a=012?key=crossref.731fd34a92c5e005c0ddb2478d74913b>.
- [108] Ziyong Li, Zhangwei Chen, Jian Liu, Yuelong Fu, Changyong Liu, Pei Wang, Mingguang Jiang, and Changshi Lao. Additive manufacturing of lightweight and high-strength polymer-derived SiOC ceramics. Virtual and Physical Prototyping, 0(0):1–15, 2020. ISSN 17452767. doi: 10.1080/17452759.2019.1710919. URL <https://doi.org/10.1080/17452759.2019.1710919>.
- [109] Hong Qing Liang, Ke Jia Ji, Li Yun Zha, Wen Bing Hu, Yang Ou, and Zhi Kang Xu. Polymer membranes with vertically oriented pores constructed by 2D freezing at ambient temperature. ACS Applied Materials

- and Interfaces, 8(22):14174–14181, 2016. ISSN 19448252. doi: 10.1021/acsami.6b03071.
- [110] A. Z. Lichtner, D. Jauffrès, D. Roussel, F. Charlot, C. L. Martin, and R. K. Bordia. Dispersion, connectivity and tortuosity of hierarchical porosity composite SOFC cathodes prepared by freeze-casting. Journal of the European Ceramic Society, 35(2):585–595, 2015. ISSN 09552219. doi: 10.1016/j.jeurceramsoc.2014.09.030. URL <http://dx.doi.org/10.1016/j.jeurceramsoc.2014.09.030>.
- [111] Aaron Lichtner, Denis Roussel, David Jauffrès, Christophe L. Martin, and Rajendra K. Bordia. Effect of macropore anisotropy on the mechanical response of hierarchically porous ceramics. Journal of the American Ceramic Society, 99(3):979–987, 2016. ISSN 15512916. doi: 10.1111/jace.14004.
- [112] J. Lipton, M. E. Glicksman, and W. Kurz. Dendritic growth into undercooled alloy metals. Materials Science and Engineering, 65(1):57–63, 1984. ISSN 00255416. doi: 10.1016/0025-5416(84)90199-X.
- [113] W. Losert, B. Q. Shi, and H. Z. Cummins. Evolution of dendritic patterns during alloy solidification: Onset of the initial instability. Proceedings of the National Academy of Sciences of the United States of America, 95(2):431–438, 1998. ISSN 00278424. doi: 10.1073/pnas.95.2.431. URL <https://www.pnas.org/content/95/2/431>.
- [114] Harsh Maheshwari, John D. Roehling, Bryce A. Turner, Jamal Abdinor, Tien B. Tran-Roehling, Milind D. Deo, Michael H. Bartl, Subhash H. Risbud, and Klaus van Benthem. Robust mesoporous silica compacts: multi-scale characterization of microstructural changes related to physical–mechanical properties. Journal of Materials Science, 51(9):4470–4480, 2016. ISSN 15734803. doi: 10.1007/s10853-016-9759-0.
- [115] Rocío Mateos, Soledad Vera, Mercedes Valiente, Ana Díez-Pascual, and María San Andrés. Comparison of anionic, cationic and nonionic surfactants as dispersing agents for graphene based on the fluorescence of riboflavin. Nanomaterials, 7(11):403, 2017. doi: 10.3390/nano7110403.
- [116] M. W. Matsen and F. S. Bates. Origins of complex self-assembly in block copolymers. Macromolecules, 29(23):7641–7644, 1996. ISSN 00249297. doi: 10.1021/ma960744q. URL <https://pubs.acs.org/sharingguidelines>.
- [117] Mehrad Mehr, Calvin Davis, Kazi Sadman, Ryan J. Hooper, Michele V. Manuel, and Juan C. Nino. Epoxy interface method enables enhanced compressive testing of highly porous and brittle materials. Ceramics International, 42(1):1150–1159, 2016. ISSN 02728842. doi: 10.1016/j.ceramint.2015.09.045.

- [118] Sarah Miller. Directional freeze casting of porous ceramics: Effects of processing parameters on pore network characteristics. PhD thesis, Northwestern University, 2016.
- [119] Sarah Miller, Xianghui Xiao, John Setlock, Serene Farmer, and Katherine Faber. Freeze-cast yttria-stabilized zirconia pore networks: Effects of alcohol additives. International Journal of Applied Ceramic Technology, 15(2):296–306, 2018. ISSN 17447402. doi: 10.1111/ijac.12794.
- [120] John K. Montgomery, Adele S. Botha, Peter L. Drzal, Kenneth R. Shull, and K. T. Faber. A thermoreversible gelcasting technique for ceramic laminates. Scripta Materialia, 48(6):785–789, 2003. ISSN 13596462. doi: 10.1016/S1359-6462(02)00517-1.
- [121] W W Mullins and R F Sekerka. Stability of a planar interface during solidification of a dilute binary alloy. Journal of Applied Physics J. Appl. Phys, 35(86), 1964. doi: 10.1063/1.371278. URL <http://dx.doi.org/10.1063/1.1713333><http://scitation.aip.org/content/aip/journal/jap/35/2?ver=pdfcov>.
- [122] Lawrence Eugene: Murr. Interfacial phenomena in metals and alloys. Addison-Wesley, Reading, 1975. ISBN 0201048841. URL <https://onlinelibrary.wiley.com/doi/abs/10.1002/piuz.19770080108>.
- [123] Masaki Narisawa. Silicone resin applications for ceramic precursors and composites. Materials, 3(6):3518–3536, 2010. ISSN 19961944. doi: 10.3390/ma3063518.
- [124] M. Naviroj, S. M. Miller, P. Colombo, and K. T. Faber. Directionally aligned macroporous SiOC via freeze casting of preceramic polymers. Journal of the European Ceramic Society, 35(8):2225–2232, 2015. ISSN 09552219. doi: 10.1016/j.jeurceramsoc.2015.02.013. URL <http://dx.doi.org/10.1016/j.jeurceramsoc.2015.02.013>.
- [125] Maninpat Naviroj. Silicon-based porous ceramics via freeze casting of preceramic polymers. PhD thesis, Northwestern University, 2017.
- [126] Maninpat Naviroj, Peter W. Voorhees, and Katherine T. Faber. Suspension- and solution-based freeze casting for porous ceramics. Journal of Materials Research, 32(17):3372–3382, 2017. ISSN 0884-2914. doi: 10.1557/jmr.2017.133.
- [127] Maninpat Naviroj, Melody M. Wang, Matthew T. Johnson, and Katherine T. Faber. Nucleation-controlled freeze casting of preceramic polymers for uniaxial pores in Si-based ceramics. Scripta Materialia, 130:32–36, 2017. ISSN 13596462. doi: 10.1016/j.scriptamat.2016.10.038. URL <http://dx.doi.org/10.1016/j.scriptamat.2016.10.038>.

- [128] Pooya Niksiar, Frances Su, Michael Frank, Taylor Ogden, Steven Naleway, Marc Meyers, Joanna McKittrick, and Michael Porter. External field assisted freeze casting. *Ceramics*, 2(1):208–234, 2019. ISSN 2571-6131. doi: 10.3390/ceramics2010018.
- [129] Taylor A. Ogden, Milo Prisbrey, Isaac Nelson, Bart Raeymaekers, and Steven E. Naleway. Ultrasound freeze casting: Fabricating bioinspired porous scaffolds through combining freeze casting and ultrasound directed self-assembly. *Materials and Design*, 164:107561, 2019. ISSN 18734197. doi: 10.1016/j.matdes.2018.107561. URL <https://doi.org/10.1016/j.matdes.2018.107561>.
- [130] R. A. Oriani. The surface tension of liquid metals and the excess binding energy of surface atoms. *The Journal of Chemical Physics*, 18(5):575–578, 1950. ISSN 00219606. doi: 10.1063/1.1747704. URL <http://aip.scitation.org/doi/10.1063/1.1747704>.
- [131] An Ouyang, Qianming Gong, and Ji Liang. Carbon nanotube-chitosan composite beads with radially aligned channels and nanotube-exposed walls for bilirubin adsorption. *Advanced Engineering Materials*, 17(4):460–466, 2015. ISSN 15272648. doi: 10.1002/adem.201400250.
- [132] Carlo G Pantano, Carlo G Pantano, Anant K Singh, Anant K Singh, Hanxi Zhang, and Hanxi Zhang. Silicon oxycarbide glasses. *Journal of Sol-Gel Science and Technology*, 14:7–25, 1999. ISSN 1573-4846. doi: 10.1023/A:1008765829012.
- [133] K. M. Pawelec, A. Husmann, S. M. Best, and R. E. Cameron. Altering crystal growth and annealing in ice-templated scaffolds. *Journal of Materials Science*, 50(23):7537–7543, 2015. ISSN 15734803. doi: 10.1007/s10853-015-9343-z.
- [134] S. S. L. Peppin, J. A. W. Elliott, and M. Grae Worster. Solidification of colloidal suspensions. *J. Fluid Mech*, 554:147–166, 2006. doi: 10.1017/S0022112006009268.
- [135] C. Pfeiler, B.G. Thomas, M. Wu, A. Ludwig, and A. Kharicha. Solidification and particle entrapment during continuous casting of steel. *Steel Research International*, 79(8):599–607, 2008. doi: 10.2374/SRI08SP024-79-2008-599. URL <https://onlinelibrary.wiley.com/doi/abs/10.1002/srin.200806172>.
- [136] David L. Poerschke, Angus Braithwaite, Daesung Park, and Fredrick Lauten. Crystallization behavior of polymer-derived Si-O-C for ceramic matrix composite processing. *Acta Materialia*, 147:329–341, 2018. ISSN 13596454. doi: 10.1016/j.actamat.2018.01.052. URL <https://doi.org/10.1016/j.actamat.2018.01.052>.

- [137] Michael M. Porter, Michael Yeh, James Strawson, Thomas Goehring, Samuel Lujan, Philip Siripasopsotorn, Marc A. Meyers, and Joanna McKittrick. Magnetic freeze casting inspired by nature. Materials Science and Engineering A, 556:741–750, 2012. ISSN 09215093. doi: 10.1016/j.msea.2012.07.058. URL <http://dx.doi.org/10.1016/j.msea.2012.07.058>.
- [138] Jürgen Pötschke and Volker Rogge. On the behaviour of foreign particles at an advancing solid-liquid interface. Journal of Crystal Growth, 94(3):726–738, 1989. ISSN 00220248. doi: 10.1016/0022-0248(89)90097-3.
- [139] Eric Prouzet, Frederic Cot, Georges Nabias, André Larbot, Patricia Kooyman, and Thomas J. Pinnavaia. Assembly of mesoporous silica molecular sieves based on nonionic ethoxylated sorbitan esters as structure directors. Chemistry of Materials, 11(6):1498–1503, 1999. ISSN 08974756. doi: 10.1021/cm9810281.
- [140] M. Raja, N. Angulakshmi, S. Thomas, T. Prem Kumar, and A. Manuel Stephan. Thin, flexible and thermally stable ceramic membranes as separator for lithium-ion batteries. Journal of Membrane Science, 471:103–109, 2014. ISSN 18733123. doi: 10.1016/j.memsci.2014.07.058. URL <http://dx.doi.org/10.1016/j.memsci.2014.07.058>.
- [141] U. Ramamurty and A. Paul. Variability in mechanical properties of a metal foam. Acta Materialia, 52(4):869–876, 2004. ISSN 13596454. doi: 10.1016/j.actamat.2003.10.021.
- [142] Aurelia I. Cuba Ramos and David C. Dunand. Preparation and characterization of directionally freeze-cast copper foams. Metals, 2(3):265–273, 2012. ISSN 2075-4701. doi: 10.3390/met2030265. URL <http://www.mdpi.com/2075-4701/2/3/265>.
- [143] A. W. Rempel and M. G. Worster. Interaction between a particle and an advancing solidification front. Journal of Crystal Growth, 205(3):427–440, 1999. ISSN 00220248. doi: 10.1016/S0022-0248(99)00290-0.
- [144] Gary M. Renlund, Svante Prochazka, and Robert H. Doremus. Silicon oxycarbide glasses: Part II. Structure and properties. Journal of Materials Research, 6(12):2723–2734, 1991. ISSN 0884-2914. doi: 10.1557/JMR.1991.2723. URL [http://www.journals.cambridge.org/abstract_{_}S0884291400014679](http://www.journals.cambridge.org/abstract/_jS0884291400014679).
- [145] A. Rodríguez, J. Canosa, A. Domínguez, and J. Tojo. Isobaric vapour-liquid equilibria of dimethyl carbonate with alkanes and cyclohexane at 101.3 kPa. Fluid Phase Equilibria, 198(1):95–109, 2002. ISSN 03783812. doi: 10.1016/S0378-3812(01)00761-0.
- [146] Jesús M. Rodríguez-Parra, Rodrigo Moreno, and María Isabel Nieto. Effect of cooling rate on the microstructure and porosity of alumina produced by

freeze casting. Journal of the Serbian Chemical Society, 77(12):1775–1785, 2012. ISSN 03525139. doi: 10.2298/JSC121018132R.

- [147] Lisa M. Rueschhoff, Luke A. Baldwin, Robert Wheeler, Matthew J. Dalton, Hilmar Koerner, John D. Berrigan, Nicholas M. Bedford, Soenke Seifert, Michael K. Cinibulk, and Matthew B. Dickerson. Fabricating ceramic nanostructures with ductile-like compression behavior via rapid self-assembly of block copolymer and preceramic polymer blends. ACS Applied Nano Materials, 2(1):250–257, 2019. ISSN 25740970. doi: 10.1021/acsanm.8b01820.
- [148] Kadambinee Sa, Prakash C. Mahakul, B. V.R.S. Subramanyam, Jagatpati Raiguru, Sonali Das, Injamul Alam, and Pitamber Mahanandia. Effect of reduced graphene oxide-carbon nanotubes hybrid nanofillers in mechanical properties of polymer nanocomposites. IOP Conference Series: Materials Science and Engineering, 338(1), 2018. ISSN 1757899X. doi: 10.1088/1757-899X/338/1/012055.
- [149] I. Sabree, J. E. Gough, and B. Derby. Mechanical properties of porous ceramic scaffolds: Influence of internal dimensions. Ceramics International, 41(7): 8425–8432, 2015. ISSN 02728842. doi: 10.1016/j.ceramint.2015.03.044.
- [150] Atanu Saha, Rishi Raj, and Don L. Williamson. A model for the nanodomains in polymer-derived SiCO. Journal of the American Ceramic Society, 89(7): 2188–2195, 2006. ISSN 0002-7820. doi: 10.1111/j.1551-2916.2006.00920.x. URL <http://doi.wiley.com/10.1111/j.1551-2916.2006.00920.x>.
- [151] Brice Saint-Michel, Marc Georgelin, Sylvain Deville, and Alain Pocheau. Interaction of Multiple Particles with a Solidification Front: From Compacted Particle Layer to Particle Trapping. Langmuir, 33(23):5617–5627, 2017. ISSN 15205827. doi: 10.1021/acs.langmuir.7b00472.
- [152] Sourangsu Sarkar, Jianhua Zou, Jianhua Liu, Chengying Xu, Linan An, and Lei Zhai. Polymer-derived ceramic composite fibers with aligned pristine multiwalled carbon nanotubes. ACS Applied Materials and Interfaces, 2(4): 1150–1156, 2010. ISSN 19448244. doi: 10.1021/am1000085.
- [153] A. Scarmi, G. D. Sorarù, and R. Raj. The role of carbon in unexpected visco(an)elastic behavior of amorphous silicon oxycarbide above 1273 K. Journal of Non-Crystalline Solids, 351(27-29):2238–2243, 2005. ISSN 00223093. doi: 10.1016/j.jnoncrysol.2005.06.008.
- [154] M. Scheffler, T. Gambaryan-Roisman, T. Takahashi, J. Kaschta, H. Muenstedt, P. Buhler, and P. Greil. Pyrolytic decomposition of preceramic organo polysiloxane. Ceramic transactions, 115:239–250, 2000. URL <https://www.tib.eu/en/search/id/BLCP%7B3ACN042344424/Pyrolytic-Decomposition-of-Preceramic-Organopolysiloxanes/>.

- [155] Caroline A. Schneider, Wayne S. Rasband, and Kevin W. Eliceiri. NIH Image to ImageJ: 25 years of image analysis. *Nature Methods*, 9(7):671–675, 2012. ISSN 15487091. doi: 10.1038/nmeth.2089.
- [156] Kristen L. Scotti and David C. Dunand. Freeze casting – A review of processing, microstructure and properties via the open data repository, FreezeCasting.net. *Progress in Materials Science*, 94:243–305, 2018. ISSN 00796425. doi: 10.1016/j.pmatsci.2018.01.001. URL <https://doi.org/10.1016/j.pmatsci.2018.01.001>.
- [157] Michelle E. Seitz, Wesley R. Burghardt, K. T. Faber, and Kenneth R. Shull. Self-assembly and stress relaxation in acrylic triblock copolymer gels. *Macromolecules*, 40(4):1218–1226, 2007. ISSN 00249297. doi: 10.1021/ma061993+.
- [158] Tapas Sen, Gordon J.T. Tiddy, John L. Casci, and Michael W. Anderson. One-pot synthesis of hierarchically ordered porous-silica materials with three orders of length scale. *Angewandte Chemie - International Edition*, 42(38):4649–4653, 2003. ISSN 14337851. doi: 10.1002/anie.200351479.
- [159] Jordi Seuba, Sylvain Deville, Christian Guizard, and Adam J. Stevenson. Mechanical properties and failure behavior of unidirectional porous ceramics. *Scientific Reports*, 6(1):24326, 2016. ISSN 2045-2322. doi: 10.1038/srep24326. URL <http://www.nature.com/articles/srep24326>.
- [160] Jordi Seuba, Sylvain Deville, Christian Guizard, and Adam J. Stevenson. Gas permeability of ice-templated, unidirectional porous ceramics. *Science and Technology of Advanced Materials*, 17(1):313–323, 2016. ISSN 18785514. doi: 10.1080/14686996.2016.1197757. URL <http://dx.doi.org/10.1080/14686996.2016.1197757>.
- [161] D. Shangguan, S. Ahuja, and D. M. Stefanescu. An analytical model for the interaction between an insoluble particle and an advancing solid/liquid interface. *Metallurgical Transactions A*, 23(2):669–680, 1992. ISSN 03602133. doi: 10.1007/BF02801184.
- [162] Noah Omar Shanti. *Microstructurally tailored ceramics for advanced energy applications by thermoreversible gelcasting*. PhD thesis, Northwestern University, 2010.
- [163] R. W. Siegel, S. K. Chang, B. J. Ash, J. Stone, P. M. Ajayan, R. W. Doremus, and L. S. Schadler. Mechanical behavior of polymer and ceramic matrix nanocomposites. *Scripta Materialia*, 44(8-9):2061–2064, 2001. ISSN 13596462. doi: 10.1016/S1359-6462(01)00892-2. URL <https://linkinghub.elsevier.com/retrieve/pii/S1359646201008922>.
- [164] Jae-II Sim, Keun-Hyeok Yang, Heung-Yeoul Kim, and Byong-Jeong Choi. Size and shape effects on compressive strength of lightweight concrete.

- Construction and Building Materials*, 38:854–864, 2013. ISSN 09500618. doi: 10.1016/j.conbuildmat.2012.09.073. URL <http://linkinghub.elsevier.com/retrieve/pii/S0950061812007350>.
- [165] Gian Domenico Sorarù, Gennaro D'Andrea, Renzo Campostrini, Florence Babonneau, and Gino Mariotto. Structural characterization and high-temperature behavior of silicon oxycarbide glasses prepared from sol-gel precursors containing Si-H bonds. *Journal of the American Ceramic Society*, 78(2):379–387, 1995. ISSN 15512916. doi: 10.1111/j.1151-2916.1995.tb08811.x.
- [166] Gian Domenico Sorarù, Stefano Modena, Emanuel Guadagnino, Paolo Colombo, James Egan, and Carlo Pantano. Chemical durability of silicon oxycarbide glasses. *Journal of the American Ceramic Society*, 85(6):1529–1536, 2002. ISSN 00027820. doi: 10.1111/j.1151-2916.2002.tb00308.x. URL <http://doi.wiley.com/10.1111/j.1151-2916.2002.tb00308.x>.
- [167] Zdenko Spitalsky, Dimitrios Tasis, Konstantinos Papagelis, and Costas Galiotis. Carbon nanotube-polymer composites: Chemistry, processing, mechanical and electrical properties. *Progress in Polymer Science (Oxford)*, 35(3): 357–401, 2010. ISSN 00796700. doi: 10.1016/j.progpolymsci.2009.09.003. URL <http://dx.doi.org/10.1016/j.progpolymsci.2009.09.003>.
- [168] D. M. Stefanescu, F. R. Juretzko, B. K. Dhindaw, A. Catalina, S. Sen, and P. A. Curreri. Particle engulfment and pushing by solidifying interfaces: Part II. Microgravity experiments and theoretical analysis. *Metallurgical and Materials Transactions A: Physical Metallurgy and Materials Science*, 29(6): 1697–1706, 1998. ISSN 10735623. doi: 10.1007/s11661-998-0092-3.
- [169] Andre´ R. Studart, Urs T. Gonzenbach, Elena Tervoort, and Ludwig J. Gauckler. Processing routes to macroporous ceramics: A review. *Journal of the American Ceramic Society*, 89(6):1771–1789, 2006. ISSN 00027820. doi: 10.1111/j.1551-2916.2006.01044.x.
- [170] Arjun P. Sudarsan, Jian Wang, and Victor M. Ugaz. Thermoplastic elastomer gels: An advanced substrate for microfluidic chemical analysis systems. *Analytical Chemistry*, 77(16):5167–5173, 2005. ISSN 00032700. doi: 10.1021/ac050448o. URL <https://pubs.acs.org/sharingguidelines>.
- [171] Ravindran Sujith, Pawan Kumar Chauhan, Jella Gangadhar, and Ankur Maheshwari. Graphene nanoplatelets as nanofillers in mesoporous silicon oxycarbide polymer derived ceramics. *Scientific Reports*, 8(1):1–9, 2018. ISSN 20452322. doi: 10.1038/s41598-018-36080-1.
- [172] Tatsuhiro Takahashi and Paolo Colombo. SiOC Ceramic Foams through Melt Foaming of a Methylsilicone Pre-ceramic Polymer. *Journal of Porous Materials*, 10(2):113–121, 2003. ISSN 13802224. doi: 10.1023/A:1026031729278.

- [173] Yufei Tang, Sha Qiu, Qian Miao, and Cong Wu. Fabrication of lamellar porous alumina with axisymmetric structure by directional solidification with applied electric and magnetic fields. Journal of the European Ceramic Society, 36(5):1233–1240, 2016. ISSN 1873619X. doi: 10.1016/j.jeurceramsoc.2015.12.012. URL <http://dx.doi.org/10.1016/j.jeurceramsoc.2015.12.012>.
- [174] Jessica D. Torrey and Rajendra K. Bordia. Processing of polymer-derived ceramic composite coatings on steel. Journal of the American Ceramic Society, 91(1):41–45, 2008. ISSN 00027820. doi: 10.1111/j.1551-2916.2007.02019.x.
- [175] D. R. Uhlmann, B. Chalmers, and K. A. Jackson. Interaction between particles and a solid-liquid interface. Journal of Applied Physics, 35(10):2986–2993, 1964. ISSN 00218979. doi: 10.1063/1.1713142.
- [176] Cekdar Vakifahmetoglu and Paolo Colombo. A direct method for the fabrication of macro-porous SiOC ceramics from preceramic polymers. Advanced Engineering Materials, 10(3):256–259, 2008. ISSN 14381656. doi: 10.1002/adem.200700330.
- [177] Cekdar Vakifahmetoglu, Paolo Colombo, Sara Maria Carturan, Eckhard Pippel, and Jörg Woltersdorf. Growth of one-dimensional nanostructures in porous polymer-derived ceramics by catalyst-assisted pyrolysis. Part II: Cobalt catalyst. Journal of the American Ceramic Society, 93(11):3709–3719, 2010. ISSN 00027820. doi: 10.1111/j.1551-2916.2010.03974.x.
- [178] Cekdar Vakifahmetoglu, Eckhard Pippel, and Paolo Colombo. Growth of one-dimensional nanostructures in porous polymer-derived ceramics by catalyst-assisted pyrolysis. Part I: Iron catalyst. J. Am. Ceram. Soc., 98(4):959–968, 2010. ISSN 00027820. doi: 10.1111/j.1551-2916.2009.03448.x.
- [179] Cekdar Vakifahmetoglu, Damla Zeydanli, and Paolo Colombo. Porous polymer derived ceramics. Materials Science and Engineering R: Reports, 106: 1–30, 2016. ISSN 0927796X. doi: 10.1016/j.mser.2016.05.001. URL <http://dx.doi.org/10.1016/j.mser.2016.05.001>.
- [180] C. Wang, J. Wang, C. B. Park, and Y.-W. Kim. Cross-linking behavior of a polysiloxane in preceramic foam processing. Journal of Materials Science, 39(15):4913–4915, 2004. ISSN 0022-2461. doi: 10.1023/B:JMSC.0000035335.92101.7c. URL <http://link.springer.com/10.1023/B:JMSC.0000035335.92101.7c>.
- [181] Chunhui Wang, Xiong Chen, Bin Wang, Ming Huang, Bo Wang, Yi Jiang, and Rodney S. Ruoff. Freeze-casting produces a graphene oxide aerogel with a radial and centrosymmetric structure. ACS Nano, 12(6):5816–5825, 2018. ISSN 1936086X. doi: 10.1021/acsnano.8b01747.

- [182] Xifan Wang, Franziska Schmidt, Dorian Hanaor, Paul H. Kamm, Shuang Li, and Aleksander Gurlo. Additive manufacturing of ceramics from preceramic polymers: A versatile stereolithographic approach assisted by thiol-ene click chemistry. *Additive Manufacturing*, 27:80–90, 2019. ISSN 22148604. doi: 10.1016/j.addma.2019.02.012.
- [183] Qingbo Wen, Zhaoju Yu, and Ralf Riedel. The fate and role of in situ formed carbon in polymer-derived ceramics. *Progress in Materials Science*, 109 (August 2018):100623, 2020. ISSN 00796425. doi: 10.1016/j.pmatsci.2019.100623. URL <https://doi.org/10.1016/j.pmatsci.2019.100623>.
- [184] S. J. Widgeon, S. Sen, G. Mera, E. Ionescu, R. Riedel, and A. Navrotsky. ²⁹Si and ¹³C Solid-state NMR spectroscopic study of nanometer-scale structure and mass fractal characteristics of amorphous polymer derived silicon oxycarbide ceramics. *Chemistry of Materials*, 22(23):6221–6228, 2010. ISSN 08974756. doi: 10.1021/cm1021432. URL <https://pubs.acs.org/doi/abs/10.1021/cm1021432>.
- [185] M J Wild and P Buhler. On the phase composition of polymethylsiloxane. *J. Mater. Sci.*, 33(22):5441–5444, 1998. URL <https://link.springer.com/article/10.1023/A:1004414820662>.
- [186] Michaela Wilhelm, Christian Soltmann, Dietmar Koch, and Georg Grathwohl. Ceramers—functional materials for adsorption techniques. *Journal of the European Ceramic Society*, 25(2):271–276, 2005. ISSN 09552219. doi: 10.1016/j.jeurceramsoc.2004.08.008.
- [187] Marcin Wojdyr. Fityk: A general-purpose peak fitting program. *Journal of Applied Crystallography*, 43:1126–1128, 2010. ISSN 00218898. doi: 10.1107/S0021889810030499.
- [188] Friedrich Wolff, Christoph Kugler, and Helmut Münstedt. Viscoelastic properties of a silicone resin during crosslinking. *Rheologica Acta*, 50(11-12): 917–924, 2011. ISSN 00354511. doi: 10.1007/s00397-010-0513-2.
- [189] Friedrich Wolff, Christoph Kugler, and Helmut Münstedt. Time- and temperature-dependent crosslinking behaviour of a silicone resin. *Rheologica Acta*, 51(1):71–80, 2012. ISSN 00354511. doi: 10.1007/s00397-011-0585-7.
- [190] Mengying Xie, Yan Zhang, Marcin J. Kraśny, Chris Bowen, Hamideh Khanbareh, and Nicholas Gathercole. Flexible and active self-powered pressure, shear sensors based on freeze casting ceramic-polymer composites. *Energy and Environmental Science*, 11(10):2919–2927, 2018. ISSN 17545706. doi: 10.1039/c8ee01551a. URL <https://pubs.rsc.org/en/content/articlelanding/2018/ee/c8ee01551a#!divAbstract>.

- [191] Leiming Yan, Jisi Wu, Lei Zhang, Xinli Liu, Kechao Zhou, and Bo Su. Pore structures and mechanical properties of porous titanium scaffolds by bidirectional freeze casting. Materials Science and Engineering C, 75:335–340, 2017. ISSN 09284931. doi: 10.1016/j.msec.2016.12.044.
- [192] Xiaojie Yan, Muhammad Sahimi, and Theodore T. Tsotsis. Fabrication of high-surface area nanoporous SiOC ceramics using pre-ceramic polymer precursors and a sacrificial template: Precursor effects. Microporous and Mesoporous Materials, 241:338–345, 2017. ISSN 13871811. doi: 10.1016/j.micromeso.2016.12.027.
- [193] Byung-Ho Yoon, Eun-Jung Lee, Hyoun-Ee Kim, and Young-Hag Koh. Highly aligned porous silicon carbide ceramics by freezing polycarbosilane/camphene solution. Journal of the American Ceramic Society, 90(6): 1753–1759, 2007. ISSN 0002-7820. doi: 10.1111/j.1551-2916.2007.01703.x. URL <http://doi.wiley.com/10.1111/j.1551-2916.2007.01703.x>.
- [194] M. Yu, Li Tang, Sanjay Shah, Loleta Chung, John Carney, Leonard Katz, Chaitan Khosla, and B Julien. Strength and breaking mechanism of multi-walled carbon nanotubes under tensile load. Science, 287(5453):637–640, 2000. ISSN 00368075. doi: 10.1126/science.287.5453.637.
- [195] Zhong-Yong Yuan and Bao-Lian Su. Insights into hierarchically meso-macroporous structured materials. Journal of Materials Chemistry, 16(7):663–677, 2006. ISSN 0959-9428. doi: 10.1039/B512304F. URL <http://dx.doi.org/10.1039/B512304F>.
- [196] Xiaomei Zeng, Noriaki Arai, and Katherine T. Faber. Robust cellular shape-memory ceramics via gradient-controlled freeze casting. Advanced Engineering Materials, 21(12):1–5, 2019. ISSN 15272648. doi: 10.1002/adem.201900398.
- [197] Guo Dong Zhan, Joshua D. Kuntz, Julin Wan, and Amiya K. Mukherjee. Single-wall carbon nanotubes as attractive toughening agents in alumina-based nanocomposites. Nature Materials, 2(1):38–42, 2003. ISSN 14761122. doi: 10.1038/nmat793.
- [198] Huixing Zhang, Pedro D Angelo Nunes, Michaela Wilhelm, and Kurosch Rezwan. Hierarchically ordered micro / meso / macroporous polymer-derived ceramic monoliths fabricated by freeze-casting. Journal of the European Ceramic Society, 36(1):51–58, 2016. doi: 10.1016/j.jeurceramsoc.2015.09.018. URL <http://dx.doi.org/10.1016/j.jeurceramsoc.2015.09.018>.
- [199] Yajun Zhang, Xiaowei Yin, Fang Ye, and Luo Kong. Effects of multi-walled carbon nanotubes on the crystallization behavior of PDCs-SiBCN and their improved dielectric and EM absorbing properties. Journal of

the *European Ceramic Society*, 34(5):1053–1061, 2014. ISSN 09552219. doi: 10.1016/j.jeurceramsoc.2013.11.044. URL <http://dx.doi.org/10.1016/j.jeurceramsoc.2013.11.044>.

- [200] Yumin Zhang, Luyang Hu, Jiecai Han, and Zehui Jiang. Freeze casting of aqueous alumina slurries with glycerol for porous ceramics. *Ceramics International*, 36(2):617–621, 2010. ISSN 02728842. doi: 10.1016/j.ceramint.2009.09.036.
- [201] Nifang Zhao, Meng Li, Huaxin Gong, and Hao Bai. Controlling ice formation on gradient wettability surface for high-performance bioinspired materials. *Science Advances*, 6(31):1–10, 2020. ISSN 23752548. doi: 10.1126/sciadv.abb4712.
- [202] Xueying Zhao, Alan Lai, and Christopher A. Schuh. Shape memory zirconia foams through ice templating. *Scripta Materialia*, 135:50–53, 2017. ISSN 13596462. doi: 10.1016/j.scriptamat.2017.03.032. URL <http://dx.doi.org/10.1016/j.scriptamat.2017.03.032>.
- [203] Pengcheng Zhu, Zhining Wu, and Yuyuan Zhao. Hierarchical porous Cu with high surface area and fluid permeability. *Scripta Materialia*, 172:119–124, 2019. ISSN 13596462. doi: 10.1016/j.scriptamat.2019.07.019. URL <https://doi.org/10.1016/j.scriptamat.2019.07.019>.
- [204] Kai Hui Zuo, Yuan Zhang, Yu Ping Zeng, and Dongliang Jiang. Pore-forming agent induced microstructure evolution of freeze casted hydroxyapatite. *Ceramics International*, 37(1):407–410, 2011. ISSN 02728842. doi: 10.1016/j.ceramint.2010.08.015.

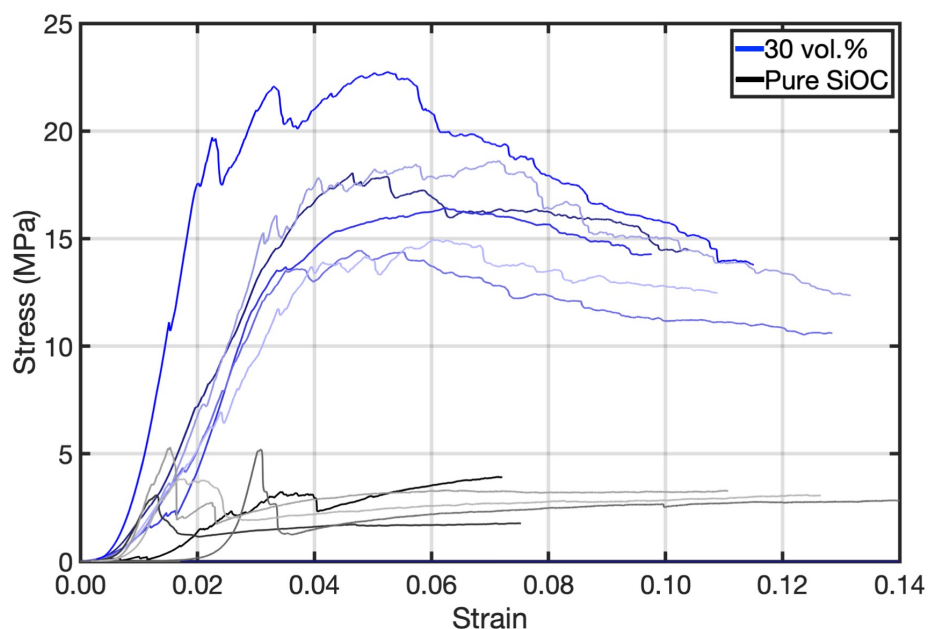
*Appendix A***STRESS-STRAIN CURVES OF SiC WHISKER COMPOSITES
AND PURE SiOC**

Figure A.1: Stress-strain curves of freeze-cast pure SiOC ceramics (black lines) and 30 vol.% SiC composites (blue lines)

As described in Section 3.6, lamellar structures of pure SiOC fail in shear fracture with a large drop in stress, followed by a gradual increase in stress. Most of the pure SiOC curve shows this behavior with only one exception. We hypothesize the natural variation in fracture strengths of ceramics and in pore alignment from freeze casting could cause this anomaly. All stress-strain curves of 30 vol.% SiC whisker composites have a series of micro-fracture events leading to a maximum in stress, followed by a softening. The differences in the uniaxial compression of the 30 vol.% SiC whisker composites and pure SiOC are shown to be repeatable and consistent.

Appendix B

**SURFACE ENERGY DIFFERENCE AS THE ORIGIN OF THE
REPULSIVE FORCE**

After engulfment, a new solid/whisker interface, designated WS, is created and the interface of whisker/liquid (WL) is eliminated (Fig. B.1(a)). These interfaces are described by γ_{WL} , the surface energy between liquid DMC and the whisker, and by γ_{WS} , the surface energy between solidified DMC and the whisker. The repulsive force arises from the difference in energy between these two interfaces. A schematic of a whisker engulfed by a dendrite is shown in Fig. B.1(b). The repulsive force F_r is calculated from the free energy difference before and after the engulfment, ΔG [168].

$$\Delta G = A\Delta\gamma = 2 \times d \times \frac{2d}{a} \Delta\gamma = F_r \times (d + 2a_0) \quad (\text{B.1})$$

Then it follows that

$$F_r \approx \frac{4d}{a} \left(\frac{a_0}{(a_0 + h)} \right)^2 (\gamma_{WS} - \gamma_{WL}) \quad (\text{B.2})$$

where A is the contact surface area between the whisker and the dendrite, a_0 is the atomic distance, and $\Delta\gamma$ is the surface energy difference between the WS and WL interfaces. The surface energy between solidified DMC and the whisker, γ_{WS} was calculated following [168]

$$\gamma_{WS} = \gamma_{SV} + \gamma_{WV} - W_{adhesion}$$

where γ_{SV} and γ_{WV} are the surface energies of solidified DMC and whiskers, respectively, and $W_{adhesion}$ is the work of adhesion between DMC and whiskers. The surface energy of solid DMC, γ_{SV} was calculated from the heat of sublimation, $\Delta H_{sublimation}$ [122, 130] from the following:

$$\gamma_{SV} \times A_{solvent} = \frac{1}{6} \Delta H_{sublimation}$$

where $A_{solvent}$ is the area occupied by one mole of surface atoms of the solvent, and $\Delta H_{sublimation}$ is the sum of the heat of fusion (ΔH_{fusion} , 11.58 kJ/mol [50]) and heat of evaporation, $\Delta H_{vaporization}$, 36.4 kJ/mol [145]) following [122, 130]. Based upon these values, γ_{SV} was found to be 3.9×10^{-2} J/m². From the droplet experiment, γ_{WL} and $W_{adhesion}$ were determined to be 23.1×10^{-2} and 5.7×10^{-2} J/m², respectively.

Finally, the surface energy difference, $\gamma_{WS} - \gamma_{WL}$, is 10.7 mJ/m^2 , within a reasonable range [138].

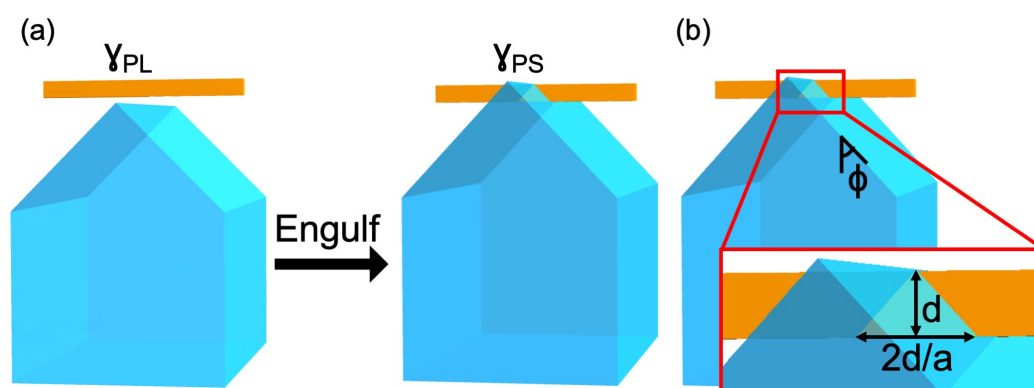


Figure B.1: A schematic of (a) the surface energy difference, and (b) the surface area of the dendrite in contact with the whisker during the engulfment process.

Appendix C

CALCULATION OF TORQUES

C.1 Torque from Fluid Motion

The pressure difference in the gap of the left side of the whisker, $\frac{\partial P}{\partial x}$, is calculated from the Navier-Stokes equations:

$$\frac{\partial P}{\partial x} = \frac{12\eta LV_{ff}}{h^3}$$

The pressure difference, $\frac{\partial P}{\partial x}$, is then integrated to produce the pressure between the left end of the whisker and any point to the left of the middle of the whisker, $\Delta P(x)$:

$$\Delta P(x) = \left(\frac{-L \sin \theta}{2} + bL \right) - P(x) = \int_x^{\frac{-L \sin \theta}{2} + bL} \frac{12\eta LV_{ff}}{h^3} ds$$

The torque from the left side of the whisker, τ_{Left} , is calculated by multiplying the force with the distance between a point to the middle of the whisker:

$$\tau_{Left} = d \int_{\frac{-L \sin \theta}{2} + bL}^0 x \int_x^{\frac{-L \sin \theta}{2} + bL} \frac{12\eta LV_{ff}}{h^3} ds dx$$

The same calculation is repeated for the right side of the whisker.

$$\frac{\partial P}{\partial x} = \frac{-12\eta LV_{ff}}{h^3}$$

$$\Delta P(x) = \left(\frac{L \sin \theta}{2} + bL \right) - P(x) = \int_x^{\frac{L \sin \theta}{2} + bL} \frac{-12\eta LV_{ff}}{h^3} ds$$

$$\tau_{Right} = d \int_0^{\frac{L \sin \theta}{2} + bL} x \int_x^{\frac{L \sin \theta}{2} + bL} \frac{-12\eta LV_{ff}}{h^3} ds dx$$

The total torque, τ_{Total} , is the summation of the left and the right torque:

$$\begin{aligned} \tau_{Total} = & \frac{6d\eta LV_{ff} \sin \theta}{(a - \cot \theta)^2} \\ & \times \left\{ \frac{\ln h - \ln h - abL + 0.5L(a \sin \theta - \cos \theta + 2b \cot \theta)}{\cos \theta - a \sin \theta} \right. \\ & + \left. \frac{L(\sin \theta - 2b)[-8h \sin \theta - 6L(\sin \theta - 2b)(a \sin \theta - \cos \theta)]}{4[2h \sin \theta + L(\sin \theta - 2b)(a \sin \theta - \cos \theta)]^2} \right\} \\ & + \frac{6d\eta LV_{ff} \sin \theta}{(a + \cot \theta)^2} \\ & \times \left\{ \frac{1.5 + \ln h - \ln h + abL + 0.5L(a \sin \theta + \cos \theta + 2b \cot \theta)}{\cos \theta + a \sin \theta} \right. \\ & - \frac{2h \sin \theta [h \sin \theta + L(\sin \theta + 2b)]}{[2h \sin \theta + L(\sin \theta + 2b)(a \sin \theta + \cos \theta)]^2} \\ & \left. - \frac{2h}{L \cos \theta + 2(h + abL + bL \cot \theta + aL \sin \theta)(a \sin \theta + \cos \theta)^2} \right\} \end{aligned}$$

C.2 Torque from Frictional Force

The Reynolds number, Re , of SiC whiskers in the freeze-cast and solidification is estimated to be $\ll 0.1$. For small Reynolds numbers (< 0.1), the drag coefficient of a cylinder, C_d , approaches 60 [41]. The drag force arising from the frictional force is calculated from the following:

$$F_d = \frac{1}{2} \rho v^2 C_d A_{whisker}$$

where v is the velocity at which whiskers rotate. $A_{whisker}$ is the cross-section area of the whisker facing the fluid. The torque from the frictional force, $\tau_{Friction}$, is calculated below and always works against the whisker motion.

$$\tau_{Friction} = F_d \times \frac{L}{2} \times 2$$

Appendix D

EXAMPLES OF ROTATION FROM THE FREEZING VIDEO

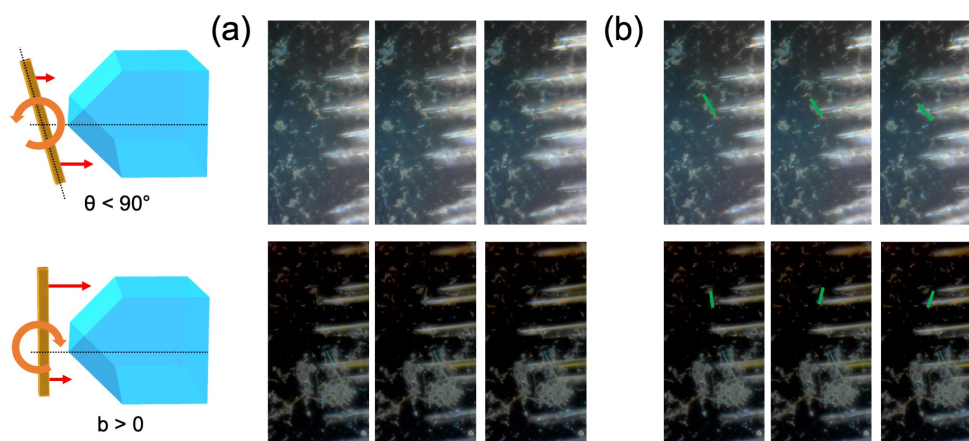


Figure D.1: Predicted rotations based on the model and examples of the rotation in the solidification video. Each image sequence is arranged chronologically with (a) original images and (b) images with green lines marking the whisker configuration.

Shown in Fig. D.1 are the predicted rotations based on the model and examples of the rotation in the solidification video. The white fingers on the right are freezing dendrites and they advanced to the left as time progressed. Each image sequence is arranged chronologically. Fig. D.1(a) shows the images directly taken from the video. In Fig. D.1(b), we marked the whiskers with green lines to highlight the rotation of the whisker. The whisker shown in the top sequence had $\theta > 90^\circ$ and it rotated counterclockwise as the model predicted. The one shown in the bottom sequence had $b < 0$ and rotated clockwise, also in agreement with the model.

*Appendix E***LAMELLAR SPACING AND FREEZING FRONT VELOCITY**

During the freezing step of freeze casting, images of the freezing process were captured every 20s by a camera with an intervalometer. Image analysis was performed using ImageJ [155] to determine the freezing front velocity. The samples were quenched at -35°C . Fig. E.1(a) shows high starting freezing front velocities which rapidly level off to a steady-state value from the bottom to the top of the sample. The freezing front velocities were similar, regardless of the SiC whisker solids loading. The freezing front velocities at 3 mm were used in the simulation to calculate the engulfed whisker fraction.

To measure the lamellar spacing, the pyrolyzed samples were sectioned through the radial center parallel to the freezing direction for longitudinal views of the pore structures. Three SEM images were taken across the height of each sample. Image analysis was performed using ImageJ to determine the lamellar spacing. The lamellar spacings increased with the sample height, as expected from a lower freezing front velocity (Fig. E.1(b)).

The relations between lamellar spacings and freezing front velocities were established through the sample height for 10, 20, 30 vol.% SiC whiskers in Fig. E.1(c). Since we could not directly measure lamellar spacing as a function of freezing front velocity, the relations were calculated from a best-fit power-law function of lamellar spacing and sample height, and a best-fit power-law function of freezing front velocity and sample height.

The measured lamellar spacing and freezing front velocity from the 2D solidification setup agrees well with those from the freeze-cast samples, indicating the 2D solidification setup is able to produce similar freezing conditions (freezing front velocity and dendritic/lamellar spacing) to those of the freeze-cast samples.

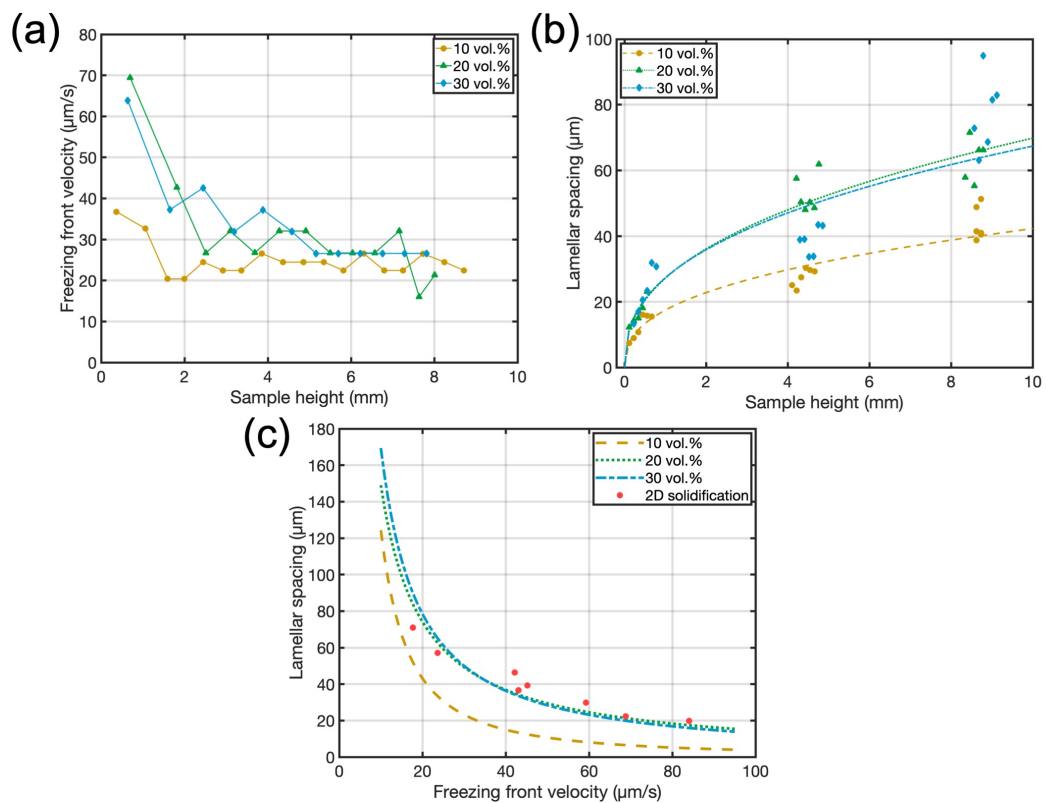


Figure E.1: (a) Freezing front velocity and (b) lamellar spacing as functions of sample height. (c) Lamellar spacing as a function of freezing front velocity